Millimeter-Scale Magnetically Actuated Robotic Tools for Surgery and Cell Manipulation

by

Onaizah Onaizah

A thesis submitted in conformity with the requirements
for the degree of Doctor of Philosophy

Department of Mechanical and Industrial Engineering
University of Toronto

Millimeter-Scale Magnetically Actuated Robotics Tools for Surgery and Cell Manipulation

Onaizah Onaizah

Doctor of Philosophy

Department of Mechanical and Industrial Engineering
University of Toronto

2020

Abstract

Small scale robots are precise end-effectors that can manipulate objects with a high degree of accuracy. Many surgical and on-chip tasks can be performed by manipulating these robots in their dedicated environments. Mobile untethered surgical robots are an attractive research area because of their ability to maneuver inside small and constrained environments and perform tasks that were previously considered infeasible. These robots enable us to make surgery minimally invasive. Surgeons can drill a hole in your skull and insert the tools inside the ventricles from where they can navigate their way to either cut or grasp tissue. Because these robots are too small for electronics and on-board power, they are often actuated remotely using magnetic fields as these field can penetrate most environments and are relatively safe for biological organisms. This makes them an ideal tool to use inside the human body and for on-chip applications. Magnetic tools can be developed and placed inside microfluidic platforms for cell manipulation such as sorting and stimulation. Both on-chip and mobile devices are explored in this thesis focusing on applications related to cell manipulation as well as surgical tools. Specifically, this thesis involves a discussion on the development of a pair of micro-surgical scissors for cutting of soft tissues as well as a magnetically oscillating beam that can be used to apply shear stress to cells and used for cell sorting purposes.

Dedication

For my dadi, and my nani, both of whom I lost during my PhD. I carry the grief of your loss in my heart. You are part of me.

Acknowledgments

There are many people without whom this work would not be possible. First, and foremost, I would like to thank my supervisor, Professor Eric Diller, for taking a chance on me, as well as for the consistent support and guidance he has provided me over the course of this work. I feel incredibly grateful to have had him as a supervisor and I cannot overstate how much I have enjoyed working with him and learned from him in the last four years. In addition, I would like to thank Professor Lidan You, for her continuous support of our collaborative project. Professor You's energy and leadership are inspirational. Thank you for your patience while we performed the multitude of cell experiments.

In addition, there were many people who provided advice and guidance on this work. I would like to acknowledge my committee members Professor Edmond Young and Axel Guenther, for their thoughtful and probing questions during our yearly meetings as well as their puns; Dr. Amir Sadri and Professor James Drake for supplying me with the motivation and enthusiasm to see my projects through. Thank you to all my lab members and collaborators for putting up with my bossy nature and my gossip. Thank you especially to Jiachen Zhang, Tianqi Xu, Omid Youssefi and Shashi Malladi for being my friends and always willing to take a coffee break.

I would also like to thank the staff members at the Department of Mechanical and Industrial Engineering, Sue Eccles, Shannon Osborne, and Liz Do, who work tirelessly to support all the students in this department and whom I consider my friends.

On a personal note, I need to thank my family, my parents and siblings, who have always provided me support as well as reality checks when I needed them and who ensure that I never forget who I am. In addition, to all the friends (especially Nasheeta Ghayas), thank you for always being willing to listen to me and providing me with countless hours of distractions from work.

Finally, I wish to acknowledge this land on which the University of Toronto operates. For thousands of years it has been the traditional land of the Huron-Wendat, the Seneca, and most recently, the Mississaugas of the Credit River. Today, this meeting place is still the home to many Indigenous people from across Turtle Island and we are grateful to have the opportunity to work on this land.

Contribution of Co-Authors

Chapter 3 On-chip Tools for Cell Manipulation

3.1 Cell Sorting Using a Magnetically Actuated Valve

J. Zhang, O. Onaizah, A. Sadri, and E. Diller, A generic label-free microuidic microobject sorter using a magnetic elastic diverter," Biomedical Microdevices, vol. 19, issue 2, pp. 43, 2017.

Prof. E. Diller and Dr. A. Sadri were involved in project design and manuscript preparation. J. Zhang was involved in mechanical design and fabrication and performed all sorting experiments. O. Onaizah developed the analytical physics-based model and performed the finite element simulations on the sorting behavior of the proposed cell sorter. O. Onaizah and J. Zhang were both responsible for collecting confocal microscope images of the proposed cell sorter. O. Onaizah also built the magnetic actuation platform (electromagnetic coils) used for all experiments. Discussions regarding research concepts, miniature robot design, experiment setup, collection and interpretation of data were continuously conducted among all contributing authors.

3.2 Local Stimulation of Osteocytes Using a Magnetically Actuated Oscillating Beam

In Preparation for Integrative Biology: Local Stimulation of Osteocytes using a Magnetically Actuated Oscillating Beam.

Prof. E. Diller and Prof. L. You were involved in project design and manuscript preparation. L. Xu performed all the work related to cells including experiments, data acquisition and analysis. O. Onaizah designed and fabricated the on-chip device and the magnetic actuation setup (electromagnets) for the Cellular Biomechanics lab. O. Onaizah developed the model and performed all the finite element simulations and analyzed this data. Discussions regarding research concepts, miniature robot design, experiment setup, collection and interpretation of data were continuously conducted among all contributing authors.

Chapter 4 Mobile Untethered Surgical Tools

O. Onaizah and E. Diller, "Tetherless Mobile Micro-Surgical Scissors Using Magnetic Actuation," in 2019 International Conference on Robotics and Automation (ICRA), 2019, pp. 894-899.

Prof. E. Diller was involved in project design and manuscript preparation. O. Onaizah was responsible for mechanical design, software development, control, image and data acquisition, and analysis. Discussions regarding research concepts, miniature robot design, experiment setup, collection and interpretation of data were continuously conducted among all contributing authors.

Table of Contents

List of Tables

List of Figures

Chapter 1
Overview of Small-Scale Robotics

This chapter summarizes the development of small-scale robotics. It discusses the changes in physical principles and fabrication methods between large robots and small-scale robots. The potential applications and capabilities of these devices are also discussed. It also covers some well-known devices in the field of small-scale robotics and discusses the advantages and challenges of using small-scale robots.

1 Overview of Small-Scale Robotics

1.1 Brief Development History

Untethered small-scale robots originated in the 1990s and have since become a widely studied research area. Their development has depended greatly on the advancement of MEMS technology as well as the parallel development of optical tweezers. The idea of scaling down devices to access small, constrained environments or perform previously infeasible operations has been in popular culture for quite a while with movies such as *Fantastic Voyage* and TV shows such as *the Magic School Bus* using this concept for biomedical and other pursuits. While the idea of scaling down already functional devices is tempting since small-scale robots offer unique solutions to problems encountered in small enclosed spaces; it is not realistic to simply scale down large robots. This is because the behaviour of small-scale robots is very different than their macro-scale counterparts.

While the physical principles governing motion on small scale devices are the same as those on large scale devices, the magnitude of the dominant forces changes drastically [1]. This is primarily a result of the surface area-to-volume ratio (S/V) changing with length. When devices are scaled down, the volume of the device is reduced by a factor of L^3 whereas the area of the device is reduced by a factor of L^2. Therefore, forces dependent on surface area suddenly start to dominate at small scales. Mass and inertia which are volume dependent play a smaller role in the mechanics of the device than forces such as friction, fluid drag, surface forces and electrostatic forces just to name a few. This has been well documented in nature as well where bacteria use their flagella to produce helical motions for swimming and water striders use surface tension instead of buoyancy to keep themselves afloat. These forces also impact the design and implementation of small-scale robots. For mechanical systems, it becomes necessary to avoid mechanisms such as gears that can present friction problems. Therefore, it becomes essential to revamp our understanding of mechanical design to take advantage of the dominant forces as well as using clever fabrication techniques.

Small-scale robot fabrication has evolved primarily from MEMS technology and microfluidic device production. Large robots are typically fabricated using bulk materials that are machined with mills and other equipment. These robots include on-board power systems and electronics

for actuation and control [1]. Small-scale fabrication techniques include photolithography, material deposition, electroplating and micromolding. Other techniques that have become common include laser printing, 3D printing, CNC milling and laser spot welding. Small-scale robots are typically assembled by a user under a microscope with a pair of tweezers which requires delicate handling and expertise although emerging techniques offer promising solutions to this [2, 3]. All the devices in this thesis were manually assembled. Microfabrication techniques often have advantages too and one big one is bulk fabrication at low cost which allows single-use devices to be more readily available.

1.2 Advantages and Challenges

Small-scale robots are an exciting solution to problems prevalent in many fields as they have the ability to access small and constrained environments. They can perform previously infeasible tasks that require a high level of delicacy and accuracy. These small-scale robots are capable of moving in 3D environments and can be precisely controlled. Traditional robotics techniques such as path planning and obstacle avoidance have been demonstrated in small spaces and microfluidic channels. Precise localization of small-scale robots has also been shown in 3D using multiple cameras for feedback.

Many challenges still remain around small-scale robotics related to motion, multi-agent control, localization, object manipulation, addition of tools and sensing. The level of precision required from small-scale robots for surgeries has only been demonstrated for very specific applications such as suturing. Putting sensors on these small-scale robots is also important for cases where vision feedback is either not possible or severely limited. Precise object manipulation also remains a challenge. The ability for multi-tool devices to work together to accomplish tasks also remains a relatively unexplored problem although it has been shown for larger scales. A prime example of this would be multiple untethered surgical tools accomplishing a task simultaneously.

Small-scale robots can offer many advantages in biomedical fields by offering promising alternatives to current techniques such as in-situ robots that can be assembled inside remote environments. One such proposed technique uses a PLA (polyactic acid) filament attached to a magnet that can be assembled inside the human body using heating elements to change the temperature to its glass transition temperature [4]. This allows the filament to be shaped into any 2D planar structure such as a gripper for microobject manipulation [4].

1.3 Applications and Capabilities

Advances in small-scale robotics have made it an ideal tool to be utilized for several different applications. Microobject manipulation is one of the most promising areas for use of this technology. This involves both contact and non-contact manipulation. Contact manipulation is able to supply large pushing and gripping forces when required. Non-contact manipulation is able to perform tasks where delicacy is required. Often the forces generated by non-contact manipulation are lower as direct handling of objects is not used. In addition, both contact and non-contact manipulation can be used to handle biological objects such as cells and tissue scaffolds and has many promising applications for lab-on-a-chip platforms. Two applications of non-contact cell manipulation are presented in this thesis.

Team manipulation involves the independent control of multiple small-scale robots to increase speed, efficiency and capability [5]. Team manipulation is highly desirable for tasks such as drug delivery where the dosage of drugs carried by each small-scale robot is low but multiple robots could access, carry and deliver the desired dosage to a target location. Team applications are also relevant for on-chip applications where multiple small robots can be used to guide cells or other microobjects down desired trajectories by opening or closing certain pathways. Small-scale robots can be used to assemble parts in 2D or 3D. They can essentially work as microfactories where teams of these robots are dispatched with tools for assembly purposes. One of the biggest advantages that these robots would offer would be parallel assembly of multiple devices together. Many of these devices are currently assembled manually by users which can take from several hours to several days to build one device; therefore, automation would be advantageous and save both time and money.

Small-scale robots offer many applications in the healthcare field ranging from drug delivery as mentioned to applications in sampling of the microbiome and biopsies. These small-scale robots have been shown to operate with a needle inside an artificial eye and ex-vivo eyes [6]. Eyes are a natural first application since a microscope can be easily used for vision feedback which makes controlling the small-scale robots straightforward. Many surgical applications have also been proposed for these small mobile untethered robots. These applications would make minimally invasive surgery more applicable for fields such as neurosurgery which are limited due to small

surgical corridors and high accuracy and precision requirements. One of these surgical applications (removal of a pineal tumour inside the brain) is discussed in depth in Chapter 4.

1.4 Thesis Objectives

The main objectives of this thesis are:

1. To understand the strengths and limits of untethered, soft, magnetic devices.
2. This will involve using physics-based models to introduce a rigorous design process to the problem.
3. New capabilities will be introduced to existing devices which will be used to solve specific biomedical problems.

These following projects will be used in order to advance the field of small-scale robotics and attempt to answer the above questions:

1. Cell Sorting Using a Magnetically Actuated Valve
    a) Design a magnetic actuation platform for operation of the magnetic valve at high speeds
    b) Develop an analytical model to optimize the geometric properties (length and width) of the valve in order to maximize deflection
    c) Develop a 3D finite element numerical simulation in order quantify the region where the cells will be successfully sorted into the desired outlets as well as optimize the width of the channel in the bifurcation region as a function of valve displacement.
2. Local Stimulation of Osteocytes using a Magnetically Actuated Oscillating Beam
    a) Design a device for non-contact fluid based local stimulation of cells and design a magnetic actuation platform in order to oscillate the beam
    b) Perform finite element numerical simulations in order to determine the shear stress threshold produced by the devices and optimize them for stimulation
    c) Stimulate cells by using the device for on-chip applications with cells.

3. Tetherless Mobile Micro-Surgical Scissors Using Magnetic Actuation

    a) Develop a proof-of-concept prototype of the first completely wireless surgical scissors capable of dexterous motion and cutting in a remote environment as a mobile microrobotic device

    b) Design an actuation model that can predict the deflection of the scissors

    c) Scale down the device to meet the size specification but ensure that enough cutting force can be generated to slice through brain tissue. Show the operation of a device inside a brain phantom while cutting brain tissue

These projects are a direct result of existing limitations of current devices that will be overcome.

1. Magnetic small-scale robotic devices have not been embedded in microfluidic chips and actuated using global magnetic fields that can be fully controlled using electromagnets

2. Using magnetic small-scale robots in a global field for new on-chip applications such as non-contact cell sorting and stimulation has not been demonstrated

3. Cutting of soft tissues in a dexterous manner using untethered mobile tools such as scissors remains an unexplored problem

1.5 Thesis Outline

This thesis outlines the work done during the course of the PhD:

- Chapter 2 covers basic magnetic actuation principles and background.

- Chapter 3 covers on-chip devices that were designed and used with new techniques and capabilities.

- Chapter 4 covers the development of a proof-of-concept pair of surgical scissors for cutting of soft tissues.

- Chapter 5 covers the contributions of this thesis to the field and future research directions are proposed.

Chapter 2
Remote Magnetic Actuation

This chapter covers the basics of magnetism and how magnetic actuation is used for small-scale robotics. It also discusses the advantages and disadvantages of using magnetic actuation.

2 Remote Magnetic Actuation

2.1 Overview

Magnetic fields are generated by moving electrical charges such as current in a loop of wire or moving electrons in block magnets [7]. All magnetic fields are vector fields projected into space. They can vary over time and space. Increasing the distance from the source of a magnetic field whether it is a loop of wire (electromagnet) or a block magnet (permanent magnet) means that it can be treated as a dipole. A magnetic dipole can be thought of as an analogue to an electric dipole; however, it is important to keep in mind that a magnetic monopole unlike an electric charge has never been observed. An electric dipole is basically composed of a positive and negative charge with vector field lines connecting the two. A magnetic dipole is similar with a magnetic north and south pole with vector field lines. The magnetization direction of a magnetic material is the vector pointing from the south pole to the north pole. The magnetic field ($\boldsymbol{B}$) of a dipole is characterized as shown in Eq. 2.1 where μ_0 is the magnetic permeability, $\boldsymbol{m}$ is the magnetic moment of the dipole, $\boldsymbol{r}$ is the distance from the center of mass of the dipole.

$$\boldsymbol{B}(\boldsymbol{r}) = \frac{\mu_0}{4\pi}\left[\frac{3\boldsymbol{r}(\boldsymbol{m}\cdot\boldsymbol{r})}{r^5} - \frac{\boldsymbol{m}}{r^3}\right] \tag{2.1}$$

Torque can be generated as a result of applied magnetic fields and can be an important control mechanism used to maneuver magnetic objects. The work done in this thesis relies heavily on the use of magnetic torque to actuate both on-chip and mobile untethered tools. When an external magnetic field is applied to a magnetized body, the body will rotate to align with this external magnetic field as shown in Figure 1. This is best demonstrated by compass needles that always align with the Earth's magnetic field. The cross product of the magnetization direction and the external magnetic field can be used to determine the direction and magnitude of the torque ($\boldsymbol{\tau_m}$) as can be seen by Eq. 2.2. This also means that the maximum magnetic torque results when the externally applied magnetic field is perpendicular to the magnetization direction of the body. This is an important design consideration for both on-chip and mobile untethered devices.

$$\boldsymbol{\tau_m} = \boldsymbol{m} \times \boldsymbol{B} \tag{2.2}$$

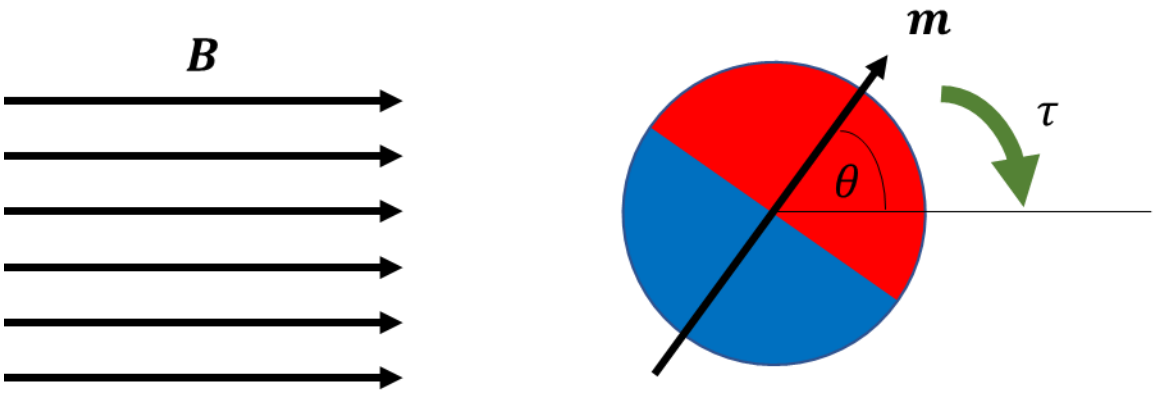

Figure 1: Magnetic torque is generated when an external magnetic field is applied.

A magnetic force ($\boldsymbol{F_m}$) is the result of a non-uniform magnetic field being applied to a magnetic body. A non-uniform field is essentially one that varies over space. This results in a spatial gradient of the magnetic field and can be used to pull magnetic material over space. Magnetic force decays quickly over distance and thus is typically weaker than magnetic torque which also decays over distance but more slowly. This is likely why magnetic force is used less frequently since it is often weaker than magnetic torque. Both magnetic torque and force can exist simultaneously. The magnetic torque will align the magnetic body in the direction of the externally applied field while the magnetic force will pull the object in the direction of the strongest field as demonstrated in Eq. 2.3 and Figure 2. This figure shows a magnetic body in which the magnetization direction is already aligned with the external magnetic field, hence no magnetic torque exists on this body. The external magnetic field is non-uniform over space and starts out strong, but it becomes weaker as it gets farther from the source and closer to the magnetic body. The resulting magnetic force will essentially pull the magnetic body in the direction of the strongest magnetic field. Therefore, the resulting magnetic force in this case is opposite of the direction of the applied magnetic field. While pushing of magnetic materials has been demonstrated, magnetic forces are more frequently just used to pull on magnetic material and thus this is often referred to as ‘gradient-pulling’ as magnetic gradients are being used to pull a magnetic body in space.

$$\boldsymbol{F_m} = (\boldsymbol{m} \cdot \nabla)\boldsymbol{B} = \begin{pmatrix} \frac{\partial \boldsymbol{B}}{\partial x} \\ \frac{\partial \boldsymbol{B}}{\partial y} \\ \frac{\partial \boldsymbol{B}}{\partial z} \end{pmatrix} \boldsymbol{m} \tag{2.2}$$

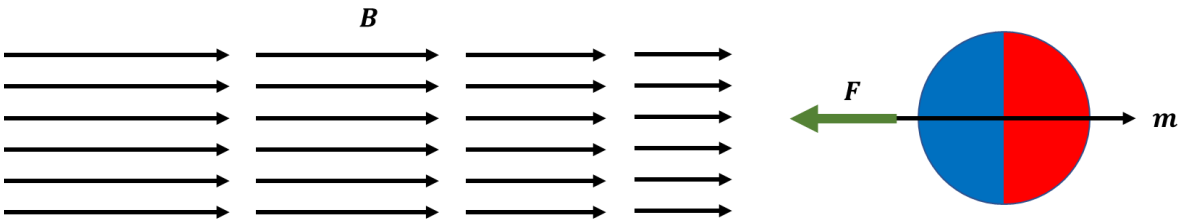

Figure 2: Magnetic force is generated when a non-uniform magnetic field is applied. This results in a gradient which is necessary to get a desired magnetic force.

Magnetic materials can be classified as: 1) hard/permanent magnets (ferromagnetic) or 2) soft magnets (paramagnetic). Ferromagnetic materials retain their magnetization direction even when there is no external magnetic field being applied. Paramagnetic materials are those that depend on an external magnetic field. When they are placed inside this external field, they will magnetize in the direction of the external field but when it is turned off, the magnetization is not retained. Due to isotropy reasons, magnetic materials often want to align on their long axis which can sometimes result in a small magnetic torque on paramagnetic materials.

A permanent magnet can be used apply both magnetic torque and force on an object as it generates a non-uniform field. Two or more permanent magnets can be arranged in a configuration where certain vector components cancel to produce a uniform magnetic field in a specific region. For example: two permanent magnets placed in the same direction on the same line of axis should be able to generate a uniform magnetic field over some workspace on an axis through the center of mass of both magnets. Of course, the magnets would have to be far enough away from each other to be treated as dipoles.

The same thing can also be achieved with electromagnets. The most well-known electromagnetic configuration is a Helmholtz coil setup. In this setup, two electromagnets are placed on the same axis with currents flowing in the same direction. The radius of both coils is same as the distance

between the coils. The supposition of the magnetic fields from each coil produces a region in the center of the workspace with uniform magnetic fields. The magnetic field produced by each coil in the Helmholtz coil setup can be descried using the Biot-Savart law as shown in Eq. 2.4 where R is the radius of each coil, x is the distance on the center line where the field is being measured, I is the current. For a Helmholtz coil setup, the two coils are placed at a distance R from each other. The center of the workspace occurs at $\frac{R}{2}$, where the magnetic field is uniform This law technically only applies to a single loop of wire and so would need to be multiplied by the number of loops inside each coil as denoted by N. By varying the parameters in this equation, the magnitude of the field can be changed as well as the design of the coils for small or large workspaces. A Maxwell coil system is similar to a Helmholtz coil system except that the current flowing inside each coil is in opposite directions. This produces a net zero field in the center of the workspace with a field gradient that is linear and generates magnetic forces.

$$B = \frac{\mu_0 I N R^2}{2(R^2 + x^2)^{\frac{3}{2}}} \tag{2.4}$$

2.2 Advantages and Disadvantages

Magnetic actuation has become a widely used technique because magnetic fields can penetrate most non-metallic environments and are essentially transparent to the human body and other biological organisms. This makes them an ideal tool for actuating small-scale robots. Magnetic fields can be used to apply both magnetic torque and force independently which are both relatively strong for manipulation purposes. Magnetic particles can often be embedded with current fabrication techniques and thus allow small-scale robots to be controlled more effectively. Magnetic fields are already used in areas of medical imaging which can make their implementation for medical technologies easier. Magnetic actuation often does not require anything onboard besides some ferromagnetic or paramagnetic material and is thus ideal for remote actuation. It allows devices to access small and constrained space as these devices can be significantly scaled down.

Magnetic fields are considered relatively safe for the human body. Static magnetic fields are safe up to 8 mT which is much larger than the desired magnetic fields for actuating most small-scale robots. Most of these robots use magnetic fields ranging from several mT to several 100 mT.

Most hard magnets used will demagnetize after 400 mT so fields larger than this are never required and in fact would be a hindrance for actuation purposes. Time-varying magnetic fields can pose more of a risk due to issues related to heating. Guidelines exist for these magnetic fields with rates of change limited to 0.1-1 T/s for frequencies up to 100 Hz [8]. The presence of pacemakers, surgical implant or other magnetic instruments can make even smaller fields dangerous

Using magnetic actuation to independently control multiple agents in a single global magnetic field remains a primary challenge and a large research area. Although significant strides have been made in independent control of two or three agents [5, 9, 10] as well as control of whole swarms [11], the ability to operate multiple identical or similar untethered devices remains a challenge. Applying local magnetic fields has been proposed but this often requires large infrastructure on which the device is operated [12]. It has potential for on-chip applications but is not feasible for mobile untethered devices that would be deployed inside the human body. Other challenges related to electromagnets often have to do with using active cooling mechanisms due to large amounts of heat that is generated [13] and of course permanent magnets require complex non-linear optimizations to generate specific magnetic fields and gradients with no ability to turn the magnetic field on or off [14].

2.3 Magneto-Elastic Devices

The small-scale robots used in this thesis are composed of both magnetic and elastic elements. The use of elastic elements is common in miniature devices because it often helps to eliminate certain control inputs by providing a restoring force. Elastic elements can take many forms from fully functional polymer devices as discussed in Chapter 3 to super elastic metallic wires as discussed in Chapter 4.

Magnetic elastic composites are used for on-chip devices in this thesis. These are composed of silicone elastomers or polymers such as PDMS (polydimethylsiloxane) which is mixed with a magnetic powder (MQFP-15-7, NdPrFeB, Magnequench) composed of magnetic particles around 10 μm in diameter. The mixture is cured and then placed in a large magnetic field in order to magnetize these permanent magnetic particles [15-17]. Magnetization direction is dependent on the desired task and also the direction of the external magnetic field relative to the tool. This allows the magnetic torque on the device to be maximized. These devices are fully

functional polymer-based devices and are used for cell sorting and cell stimulation. Simple beam bending models can be used to characterize the behaviour of these devices as shown in Eq. 2.5 where M is the applied moment on the end of the beam, L is the length of the beam, E is the elastic modulus, J is the second moment of inertia and v_{max} is the maximum deflection on the beam.

$$v_{max} = \frac{ML^2}{2EJ} \tag{2.5}$$

While these polymer-based devices work well for on-chip tasks, their usefulness as mobile untethered devices for surgical tasks is limited. This is largely due to the fact that these devices often need to apply large forces to their environments for tasks such as tissue resection or biopsy sample collection. The forces generated by these devices are lower because the concentration of magnetic material is a smaller. Magnetic torque and force are directly proportional to the magnetic moment of a body. Magnetic moment is directly proportional to the volume of magnetic material present. For these polymer mixtures, the volume is too small to produce sufficient torques and forces. This is where off-the-shelf permanent magnets are useful because of their much larger volumes. The are used along with a super elastic nitinol (nickel-titanium alloy) wire to achieve similar results but with larger torques and forces. Again, the same beam bending equations can be used as shown in Eq. 2.5.

Chapter 3
On-chip Tools for Cell Manipulation

Isolating cells is essential for research and clinical purposes. Cell sorting is the process in which individual cells or cell populations can be isolated based on specific characteristics. For example: normal cells can be isolated from tumour cells to study each individually and develop cancer therapies. Current cell sorting devices exist (e.g., flow cytometers) but have significant limitations related to safety and cost. This chapter proposes a microfluidic device as an alternative to the current devices. The device consists of a bifurcated flow channel with a mechanical valve that is magnetically actuated. The device is fabricated using conventional microfabrication techniques such as photolithography. The valve is actuated using a specifically designed electromagnetic coil system for fast speeds. Both an analytical model of the valve dynamics as well as a numerical fluid flow model for the fluid dynamics surrounding the valve have been developed. The goal of the modelling is to optimize the valve and channel geometry to achieve accurate sorting and thus increase the sorting efficiency.

These results have been published in (Reprinted with permission from Springer Nature):

J. Zhang, O. Onaizah, A. Sadri, and E. Diller, A generic label-free microuidic microobject sorter using a magnetic elastic diverter," Biomedical Microdevices, vol. 19, issue 2, pp. 43, 2017.

Mechanical loading on bone tissue is an important physiological stimulus that plays a key role in bone growth, fracture repair, and treatment of bone diseases. To measure the response of bone cells to selective mechanical stimulation in physiologically-relevant arrangements, there is a need for a platform which can locally stimulate a selected region of bone cell culture with a fluid shear stress gradient. This chapter proposes a device to achieve non-contact local stimulation of cells with a magnetically actuated beam that simulates the fluid shear stresses encountered in vivo. The stimulating beam is made from a composite of magnetic powder and polymer, where a magnetic field is used to precisely oscillate the beam in the horizontal plane. The beam is placed above a cell surface adherent to the cells with a small gap height. Finite element simulations are performed to quantify the shear stress values and to generate a shear stress map in the region of interest. Osteocytes arranged over the region are stimulated where their intracellular calcium response quantified based on their position and local shear stress value. Cells closer to the

oscillating beam respond earlier compared to cells further away from the shear stress field generated by the beam. Experiments have demonstrated the capability to mimic the propagation of calcium signalling to osteocytes outside of the stimulatory region.

These results are in preparation for submission to:

Integrative Biology: Local Stimulation of Osteocytes using a Magnetically Actuated Oscillating Beam.

3 On-chip Tethered Tools for Cell Manipulation

3.1 Cell Sorting Using a Magnetically-Actuated Valve

3.1.1 Introduction

Isolating and sorting cells is essential for research purposes in many areas of biology and biotechnology and has widespread clinical appeal [18-21]. The purpose of cell sorting is to isolate individual cells or cell populations by well-defined characteristics for individual study. For example: a population of tumour cells can be separated from normal cells based on their observable properties. This is essential when developing cancer therapies. Advances in many areas of research and the desire for personalized medicine have increased the need for high performance cell sorting devices.

Flow cytometers are considered the gold standard in cell sorting. They are used to sort cells based on a fluorescence activated tag attached to the cell [22]. Current cell sorting devices have significant limitations including safety concerns due to hazardous aerosols that could potentially contaminate the sample as well as users. High operating pressures used in the sample could also damage the structure or function of the cells. In addition, large bulky instrumentation is used which requires a large space and outside technical expertise. The limitations combined with the high costs associated with the system make it an infeasible option in the clinic. The commercialization of a low cost and clinically efficient system could vastly improve the state of cell sorting. These would be single use disposable devices that can be manufactured in bulk.

Microfluidic cell sorting devices can address many of the limitations of current cell sorting devices and offer a better tool to researchers at a lower cost. A safe and low-cost alternative cell sorting device would allow many researchers to use this technology. Electrostatic actuators [23], optical tweezers [24] and magnetically labelled cells [25] have all been proposed for cell sorting purposes. However, electrostatic actuators can often require high voltages which can damage cells [26]. Optical tweezers are non-contact so damage is limited but they do not produce forces large enough to manipulate large cells (on the order of 100 μm) [26]. Magnetic labelling of cells is a contact procedure and thus also risks damaging cells.

A novel microfluidic magnetic cell sorting device is proposed to overcome many of these limitations. This sorting tool consists of a flow channel with a valve that mechanically moves within the channel to control the path of cells. The channel is made using standard PDMS microfabrication techniques, while the valve is seeded with magnetic micro-particles and is manually assembled into the flow channel. The magnetically actuated valve is placed near the bifurcation point in a channel with an inlet and two outlets. Therefore, cells are not magnetically labelled but the valve controlling the direction of flow is. Reliable technologies in this area are lacking due to limitations in speed, control, and fabrication [22, 26, 27]. The valve is actuated using a uniform magnetic field strength of 10 mT supplied by a Helmholtz coil configuration. Fluid seeded with microbeads (to simulate cells) is used during experiments. The microbeads are centered using 3D flow focusing and the valve is used to control the path of the beads. An analytical model for the magnetically actuated valve has been designed and numerical simulations are performed to study fluid flow around the tip of the valve. The proposed device will be integrated with an automated detection system for cell sorting.

3.1.2 Methods

3.1.2.1 Device Design and Fabrication

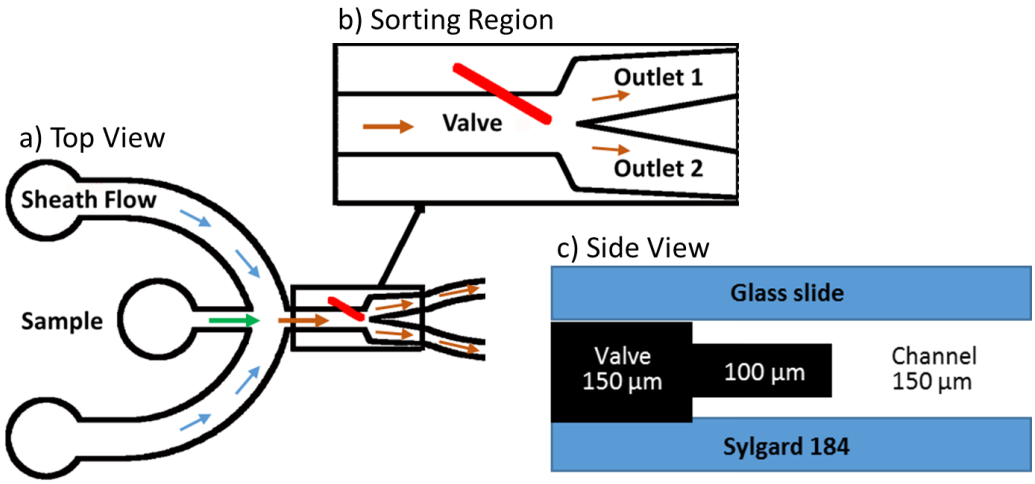

Figure 3: The proposed cell sorting chip is shown a) Top view, b) the main sorting region and c) side view of the channel.

A cell sorting design is studied using both an analytical model and numerical simulations. The top view of the proposed cell sorting chip is shown in Figure 3. It consists of three inlets and one

outlet. Two of the three inlets are used to focus the beads into the center of the channel using 3D flow focusing [28]. The sample, which consists of the cells in a medium (microbeads used for all experiments), is fed through the third inlet. Due to 3D flow focusing, all the beads are centered and have approximately the same velocity. The main operating region (as shown in Figure 3b) includes the combined flow from all three inlets that is bifurcated into two outlets. The valve is embedded into the side wall of the channel and is mechanically moved using magnetic fields. Due to the positioning of the valve, all the beads are automatically sorted into outlet 2. To sort beads into outlet 1, the valve is moved downwards to disturb the fluid flow around the tip. Accurate sorting requires the beads to be in a specific region that will be discussed later.

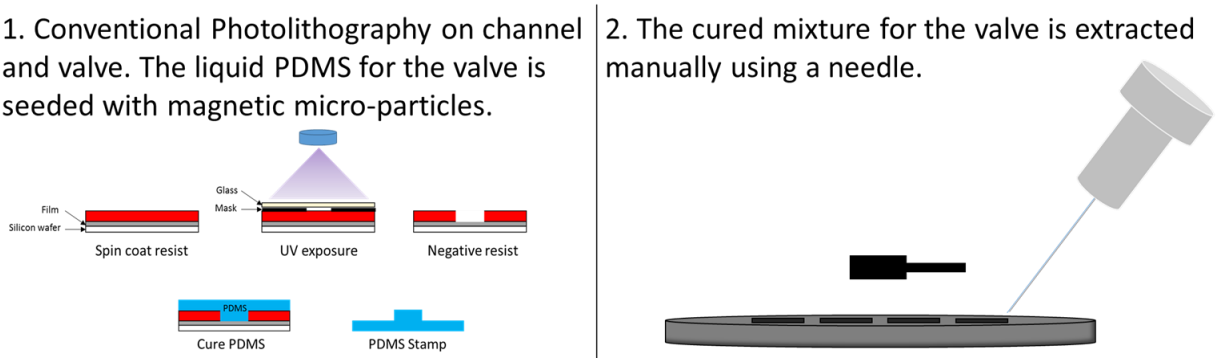

Figure 4: The microfluidic device is made using standard lithography techniques. The valve is seeded with magnetic microparticles in a 1:1 ratio by mass with PDMS and extracted using a needle.

Both the valve and the channel are made from standard photolithography techniques [29]. For the valve, a negative mold is created and the elastomer PDMS (Sylgad 184, Dow Corning) is mixed with magnetic micro-particles (MQFP-15-7, NdPrFeB, Magnequench) before it is cured to give the valve its magnetic characteristics. The valve is removed from its mold using a needle as shown in Figure 4 and then magnetized by being placed in a large (1.1 T) magnetic field. This also ensures that all the individual magnetic particles are oriented in the direction of magnetization. The valve is then manually inserted into the channel which is then sealed using a glass slide. The side view of the final channel is shown in Figure 3c. The portion of the valve that is embedded into the side wall of the channel and does not move as it is the same height as the channel (150 μm). The portion of the valve that moves is 100 μm leaving a gap of 25 μm both above and below. The gap size was experimentally optimized so that it was large enough to

significantly reduce both friction and drag on the valve but small enough to also ensure that the beads being sorted cannot sneak above and below the valve and reduce sorting efficiency. The height of the valve (100 µm) is optimized so that large cells can also be accurately sorted. The length and width of the valve are 1 mm and 40 µm respectively and will be further discussed in Section 3.1.2.4.

The principles of the device are shown in Figure 5. Due to the positioning of the valve and the sample flow (with microbeads) which is centered inside the channel, all cells automatically go into outlet 2 unless the valve is actuated. This reduces the control inputs required to magnetically actuate the valve. When the valve is actuated, it creates vortices that sort the cell into outlet 1. We will see in our results that the timing of the actuation is key with respect to the location of the cells when sorting.

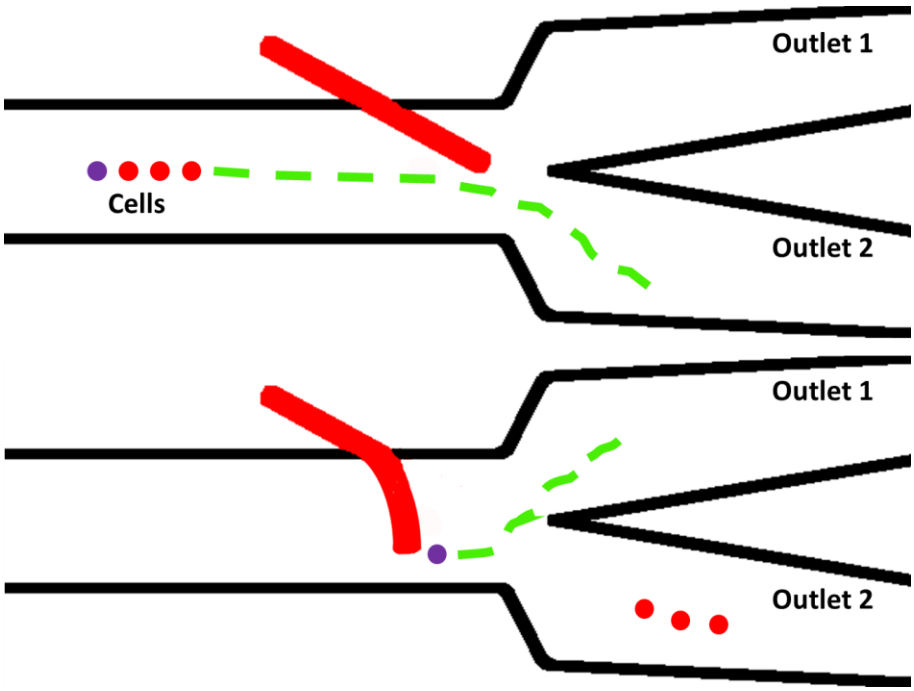

Figure 5: The basic principle of the device where cells are automatically sorted into outlet 2 until the valve is actuated to sort the cell into outlet 1.

3.1.2.2 Experimental Setup

The cell sorting chip is placed inside a specifically designed coil system based on the Helmholtz configuration to maximize magnetic fields in the center of the workspace. The coil system is

connected to amplifiers that can generate a maximum current of around 20 Amps. A step input signal is supplied to the coil system to move the valve when the beads are in the correct region. The sorting and valve movement are imaged using a camera connected to a microscope. The coil system has low inductance which allows it to generate high frequency fields. The valve can be moved with the same deflection (μm) for up to 1 kHz after which fluid drag effects significantly reduce the deflection. The coil system is shown in Figure 6.

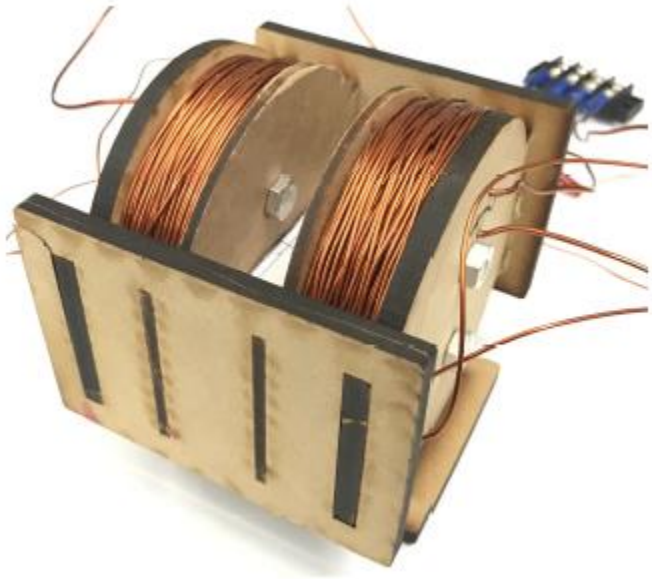

Figure 6: The coil system specifically designed to have low inductance and actuate the valve at fast sorting speeds.

The valve is actuated using magnetic torque ($\tau_{magnetic}$) which is a result of applying a magnetic field (B) perpendicular to the direction of the magnetic moment (m) as shown in Figure 7 and Eq. 3.1 where θ is the valve deflection. As mentioned previously, the valve is magnetized before being inserted into the channel. Since the valve is placed into the channel at a 30° angle, the magnetization direction is in the x-direction (30° from the long axis of the valve) as shown in Figure 7. A magnetic field applied in the y-direction will result in a torque on the valve as it will move to try to align the magnetization direction to the field direction. By applying an oscillating field in the +y and -y directions (i.e. a sinusoidal or square wave signal), the valve can be moved back and forth about its own axis. Other torques acting on the valve are the elastic torque

($\tau_{elastic}$) as shown in Eq. 3.2 where k is the elastic coefficient and the drag torque (τ_{drag}) as shown in Eq. 3.3 where b is the drag coefficient.

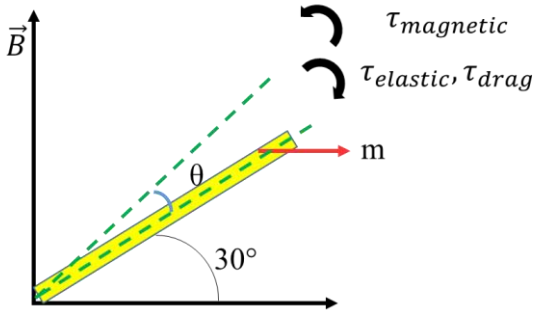

Figure 7: The actuation of the valve is displayed. It is a result of magnetic torque which tries to align the magnetic moment (m) and magnetic field (B) directions. The other torques acting on the valve are drag torque and elastic torque.

$$\tau_{magnetic} = mB\cos\theta \tag{3.1}$$

$$\tau_{elastic} = k\theta \tag{3.2}$$

$$\tau_{drag} = b\dot{\theta} \tag{3.3}$$

3.1.2.3 Image Processing Framework

To obtain the valve deflection as a function of time, an image processing tool is developed to analyze the images collected using a high speed camera as shown in Figure 8a. The grayscale images are first turned into binary images from which the valve tip extrema (corner values) are obtained. These locations (y_i and y_j) can be plotted for each image to get valve deflection in terms of position as shown in Figure 8b. The location of the valve at each point can also be used to calculate the angle of the valve from its initial axis using a rigid body approximation ($\theta = arctan(\frac{y}{x})$) as shown in Figure 8c.

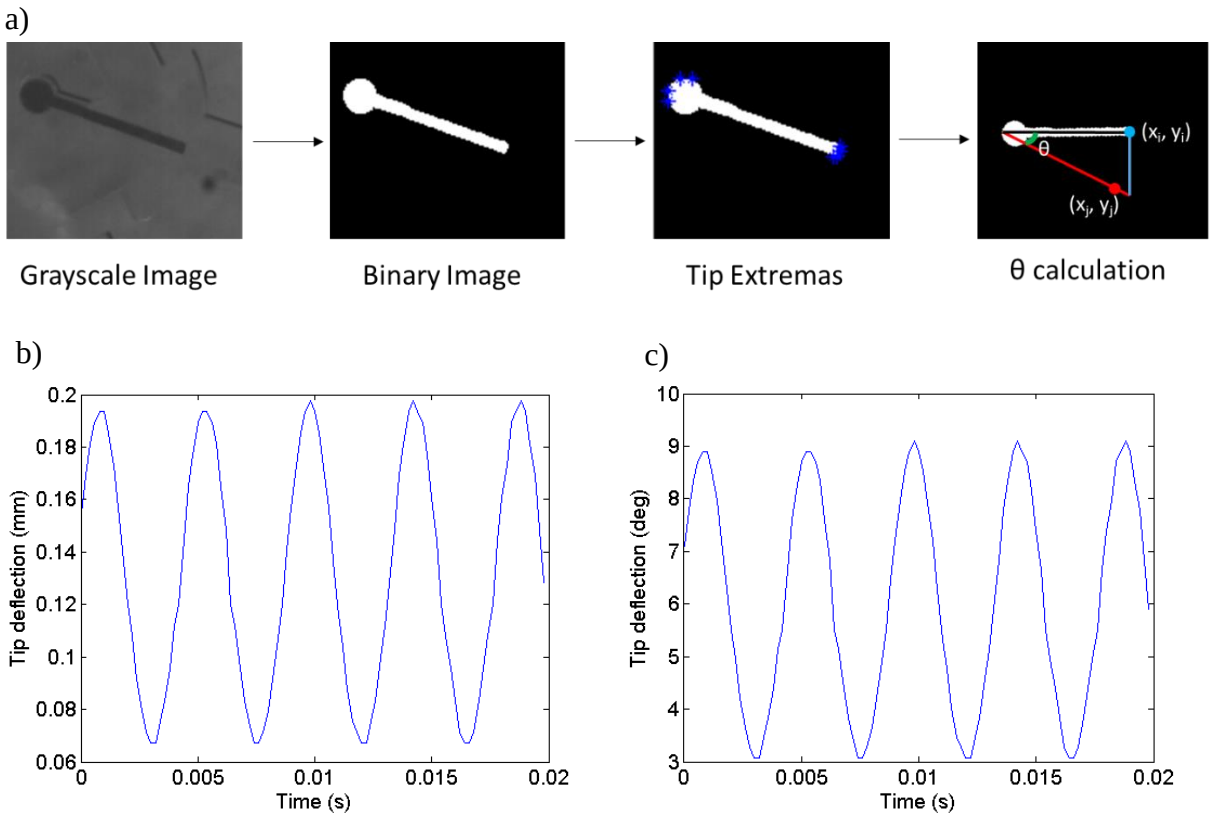

Figure 8: Image Processing Tool: a) steps taken to obtain valve deflection, b) valve deflection in terms of position where y_i and y_j are recorded and c) valve deflection in terms of the angle.

3.1.2.4 Analytical Model

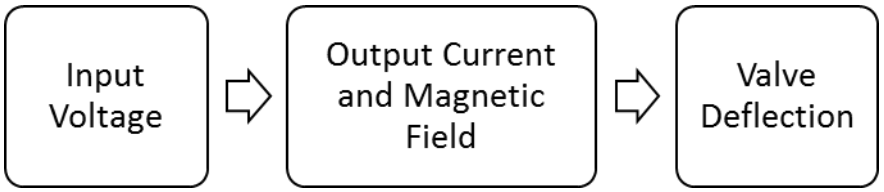

Figure 9: Building a relationship between the input voltage and valve deflection using the output current and magnetic field generated.

A relationship between input voltage and valve deflection can be established using output current as shown in Figure 9. A transfer function is fitted to the changes in amplitude and phase with increasing frequency and plotted in Figure 10a. The transfer function for a system with only resistance (R) and inductance (L) is also plotted in Figure 10a and shown in Eq. 3.4. Ideally, this transfer function would fit the data perfectly. However, the amplifier is essentially a black box

that can consist of capacitance (C) and other LR combinations and results in a unique transfer function (Eq. 3.5). This fitted transfer function (TF) is then used to generate an output current from the input voltage. As it can be seen in Figure 10b, the resulting current matches well with the measured current.

$$LR = \frac{2.598\text{x}10^4}{s + 5281} \tag{3.4}$$

The model is designed to understand how the magnetic valve is actuated in response to the input voltage. The current in the coils is proportional to the generated magnetic field that actuates the valve. The sinusoidal input voltage supplied from the signal generator and the output current from the amplifier are both measured. This is done for a frequency range from 1 mHz to 3.3 kHz. The change in amplitude and the phase lag between input voltage and output current are calculated and a transfer function (TF) is fitted to the data as shown in Figure 10 and Eq. 3.5.

$$TF = \frac{1.07\text{x}10^4 s + 1.054\text{x}10^8}{s^2 + 4225s + 2.74\text{x}10^7} \tag{3.5}$$

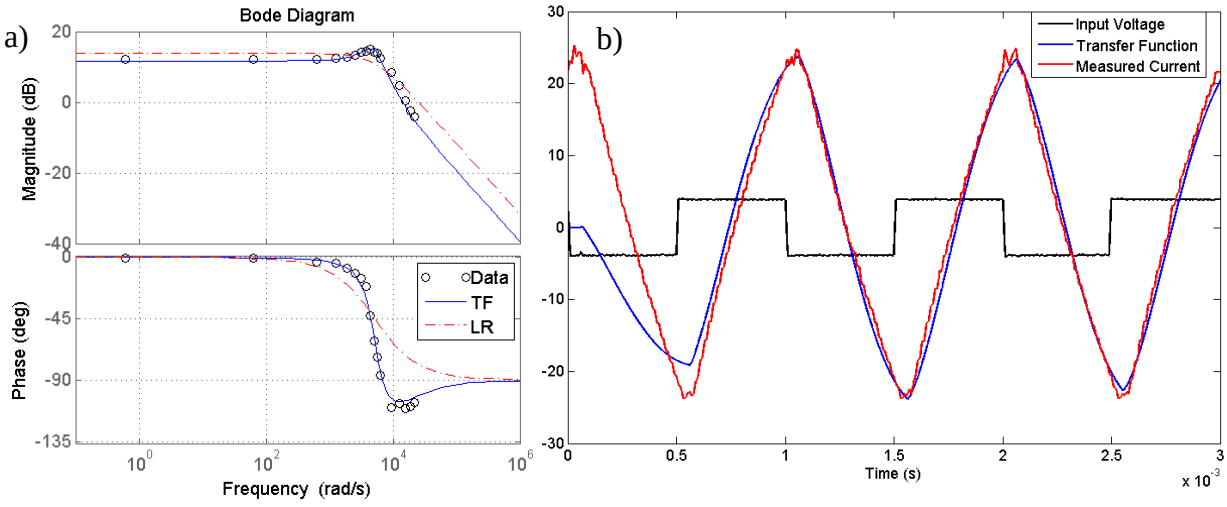

Figure 10: The relationship between input voltage and output current is shown. a) A bode diagram of the amplitude change and phase lag at the different frequencies is shown as well as a fitted transfer function (TF) and an LR transfer function. b) The transfer function is used obtain a simulated current from an input voltage that matches well with the measured current.

The resulting current is then used to obtain the simulated valve deflection using a simple model involving a balance of torques (drag, elastic and magnetic) as shown in Eq. 3.6.

$$\tau_{drag} + \tau_{elastic} = \tau_{magnetic} \tag{3.6}$$

The inertial torque is neglected because its inclusion was found to have negligible effects on the results. The 1D differential equation is shown in Eq. 3.7

$$b\dot{\theta} + k\theta = C_1 I(t)\cos\theta \tag{3.7}$$

where C_1 is an arbitrary magnetic coefficient relating the magnetic field ($B(t)$) to the current ($I(t)$). The parameters b, k and C_1 are determined below. This simple 1D ordinary differential equation can be used to solve for the valve deflection θ.

The drag coefficient b is:

$$b = \frac{WL^3\mu}{2h} \tag{3.8}$$

where W is the width of the valve, L is the length of the valve, $2h$ is the gap height between the valve and PDMS floor and μ is the viscosity. The drag coefficient is modelled using a Couette flow approximation. Couette flow is the resulting flow field when one of the walls is moving and the other is stationary.

The stiffness (k) of the valve is:

$$k = \frac{3EI_{cross}}{L} \tag{3.9}$$

where E is the Young's modulus of the valve, and I_{cross} is the area moment of inertia ($I_{cross} = \frac{1}{12}W^3H$ - where H is the height of the valve).

The magnetic coefficient (C_1) is defined as:

$$C_1 = \frac{mB(t)}{I(t)} \tag{3.10}$$

By studying the steady state step input response, the drag torque can be neglected. Therefore, by equating the elastic and magnetic torques a ratio of $\frac{C_1}{k}$ can be obtained as shown in Figure 11b. Similarly, a ratio of $\frac{C_1}{m}$ can also be obtained as shown in Figure 11a by measuring the current $I(t)$ and the generated field $B(t)$ using a gauss meter. Using a theoretical value of m, both C_1 and k can be independently obtained.

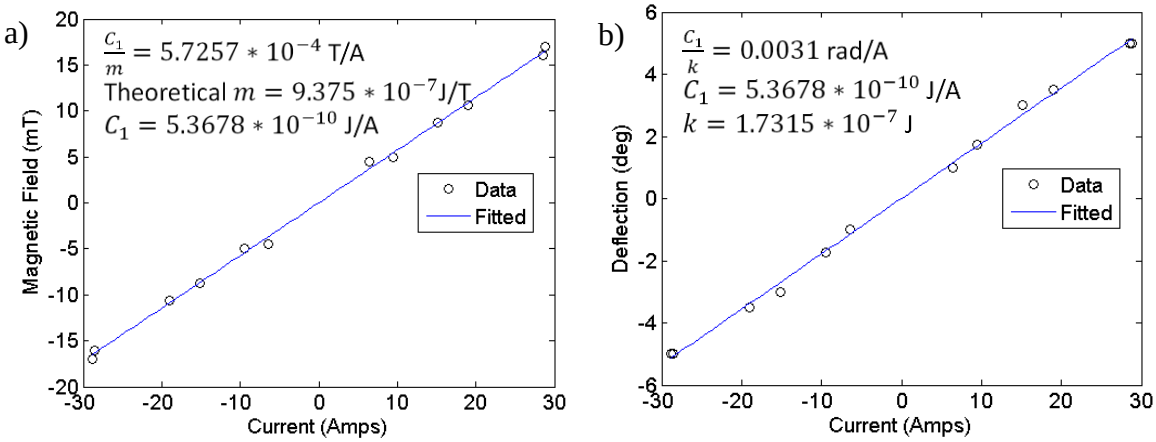

Figure 11: The coefficients C_1 and k are calculated respectively. a) A plot of magnetic field (B) vs. current (I) outputs a slope of C_1/m and using a theoretical value for the magnetic moment (m), C_1 can be obtained. b) A plot of valve deflection (θ) vs. current (I) using a steady state step input is used to find the slope of C_1/k. Using the value of C_1 from a), a value of k can be obtained.

There is now only one unknown parameter which is the drag coefficient b. As seen from Eq. 3.8, a theoretical value can be calculated. The theoretical values of the drag torque for a Couette flow approximation are plotted in Figure 12 as a function of the length of the valve and gap height from the bottom surface. For comparison purposes, the drag coefficient resulting from drag torque on a rotating ellipsoid [1] and the experimental drag coefficient (discussed further in Figure 14) values are also shown in Figure 12 and Table 1.

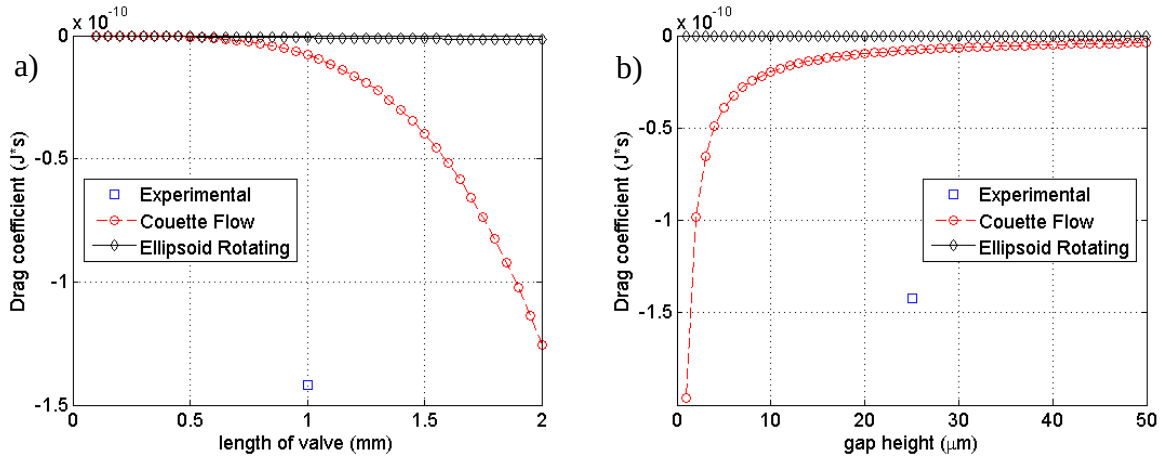

Figure 12: **Drag coefficient values using the Couette flow approximation, the rotating ellipsoid approximation and the experimentally determined value are plotted against a) the length of the valve and b) the gap height from the bottom surface.**

Table 1: **The drag coefficient values using the two approximations (Couette Flow and Rotating Ellipsoid) as well the experimental value are listed.**

	Drag torque at 1 mm valve length	Drag torque at 25 um gap height
Ellipsoid Rotating	$8.40 \times 10^{-13}\ Js$	$5.02 \times 10^{-13}\ Js$
Couette Flow	$7.85 \times 10^{-12}\ Js$	$7.85 \times 10^{-12}\ Js$
Experimental	$1.42 \times 10^{-10}\ Js$	

Using the theoretically determined values for the drag coefficient b, a simulated valve deflection can be plotted from any input voltage as shown in Figure 13.

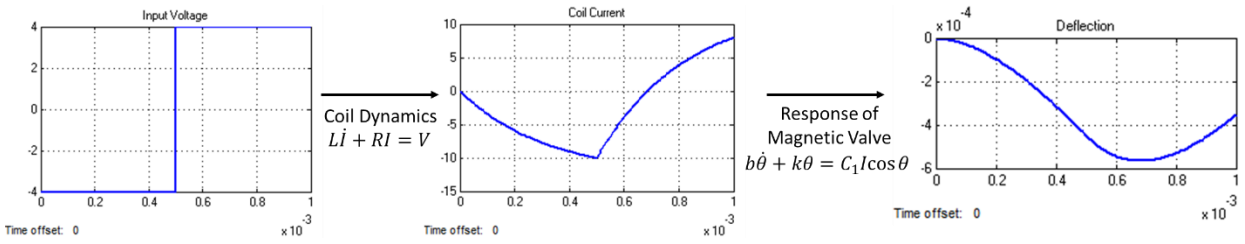

Figure 13: The relationship between input voltage and valve deflection has been established and can be used to obtain a simulated valve deflection.

The last unknown parameter b can be solved for by fitting the experimental data obtained by using the image processing tool to the simulated deflection as shown in Figure 14. The value of b is determined to be $1.42 * 10^{-10} J * s$. As can be seen from Table 1, the theoretical value of b as determined using the Couette flow approximation is about 20 times smaller than the experimental value and the rotating ellipsoid approximation is several orders of magnitude smaller.

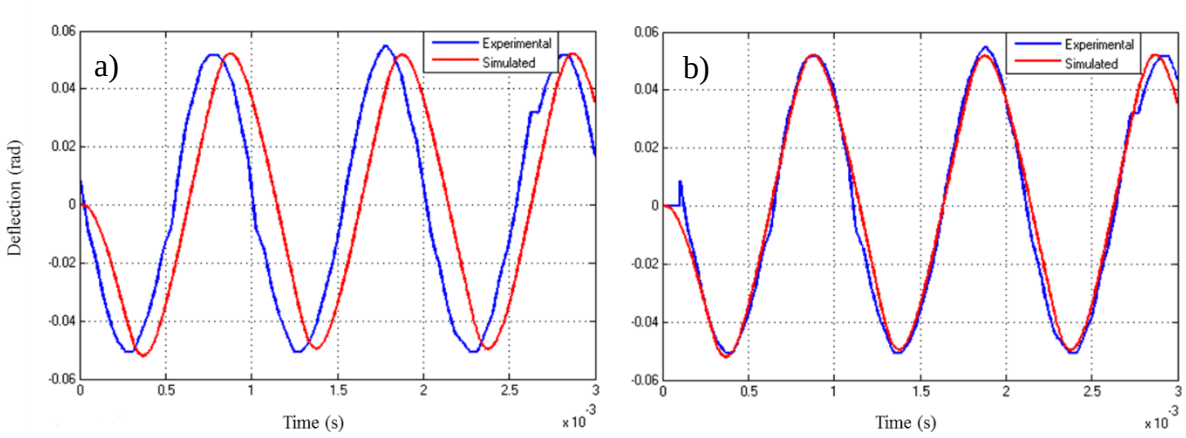

Figure 14: **The experimental and simulated results for valve deflection are plotted. The simulated results have been matched to the experimental one by iteratively changing the value of b. a) The results have been matched but there is delay between the experimental and theoretical results. This delay of 0.1 ms could be a result of amount of time it takes for the valve to respond after the input voltage signal is given. In b), the experimental results have been adjusted to account for the delay in order to show that the two have been successfully matched.**

The analytical model is used to understand the dynamics of the valve movement and specifically how changing the geometrical properties of the valve can maximize the amount of deflection.

$$\theta(t) = \theta_{homogenous} + \theta_{particular} \tag{3.11}$$

$$\theta(t) = A_1 e^{-\frac{k}{b}t} + \frac{C_1 I_{max}(k \cos \omega_d t + b\omega_d \sin \omega_d t)}{{\omega_d}^2 b^2 + k^2} \tag{3.12}$$

Here A_1 is the initial starting position of the valve, I_{max} is the maximum current that can be generated by the amplifiers and ω_d is the driving frequency of the valve which is set to $2\pi f$

where f is set to 1 kHz in Figure 15 and t is the time. The valve deflection can now be plotted as a function of time using Eq. 3.12 since all parameters are known.

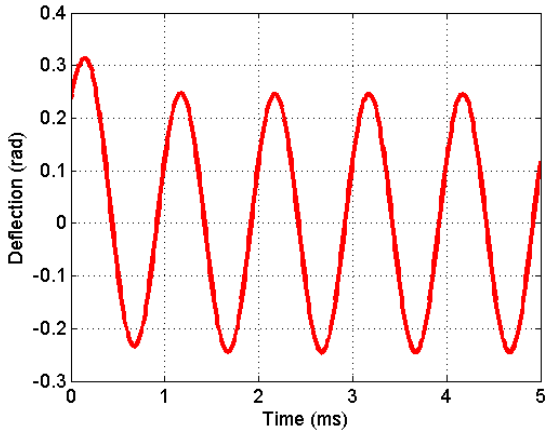

Figure 15: Valve deflection plotted as a function of time using Eq. 7.

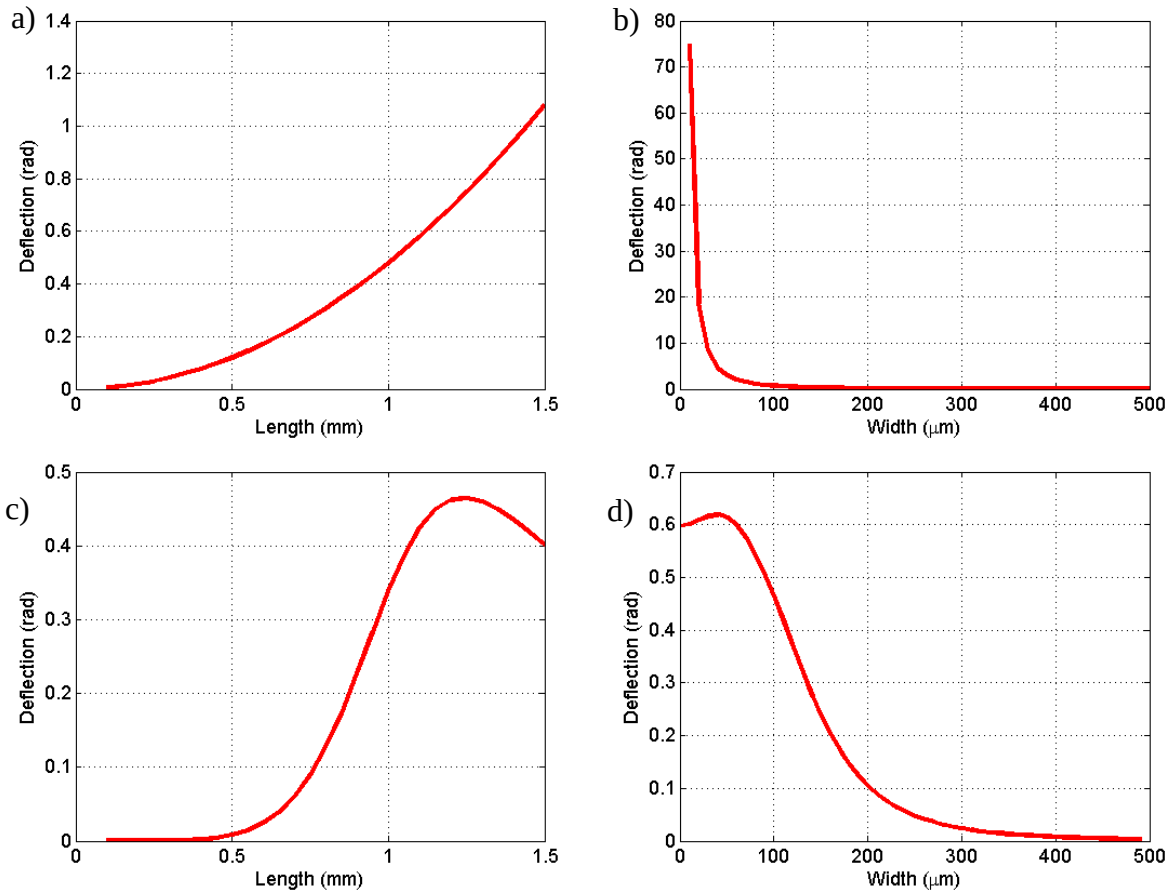

Figure 16: The valve deflection is plotted as function of length (a,c) and width (b,d) of the valve. In a-b, fluid drag effects are neglected. In c-d, the fluid drag effects are included.

The valve deflection can also be plotted against geometrical parameters of the valve such as length, width and height as well as the gap height between the valve and the bottom of the channel. The associated time t selected for these comparisons corresponds to the maximum deflection but could be arbitrarily chosen to be any point as all deflections are calculated for the same time point. Since the length and width are the two parameters that can be most easily altered, the valve deflection is plotted as a function of the length and width of the valve for two cases: 1) neglecting fluid drag which is a reasonable assumption at low frequencies and 2) including fluid drag which is essential for high frequency results.

The results are shown in Figure 16. In Figure 16a-b, fluid drag effects are neglected and in both cases there is no actual maximum value of valve deflection. The valve deflection is proportional to the length of the valve and inversely proportional to the width of the valve. In b) the valve deflections predicted for small widths are huge. It is important to note, that realistically the valve deflection cannot go above $\frac{\pi}{2}$ as the magnetization and magnetic field directions will be perfectly aligned and no further torque on the valve will be applied. When drag torque is included, a maximum deflection is found at a length of 1.3 mm and width of 40 μm. The width for the experimental valve is then fixed at this value while the length of the valve is chosen to be 1 mm instead of 1.3 mm due to practical considerations such as the width of the channel. A 1 mm valve still maintains 80% of the maximum deflection and can be actuated more smoothly. The same data is shown in Figure 17 as a surface plot to show that both parameters can be optimized simultaneously to achieve the maximum deflection.

3.1.2.5 Finite Element Simulations

While the analytical model attempts to understand the mechanics of the valve, the numerical model attempts to understand the fluid mechanics that result from the valve movement. All simulations are done using COMSOL Multiphysics and ANSYS Workbench 16. Before the numerical simulation can be used to alter the geometry or to understand the fluid flow surrounding the valve, it must be matched to experimental results. A Fluid Structure Interaction (FSI) simulation is done using a 2D channel geometry with no pressure driven flow. The valve (defined as a linear elastic material) is moved due to a body load step input force defined as $F_y = -2.5 \text{ x} 10^7 * step1(t)$ where $step1(t)$ is shown in Figure 18. The body load is applied at 0.01 s and is applied in the y-direction to mimic the experimental scenario. Only the bifurcation region is simulated to simplify

the geometry and thus make the simulations faster. The channel is filled with water and responds accordingly to the valve movement.

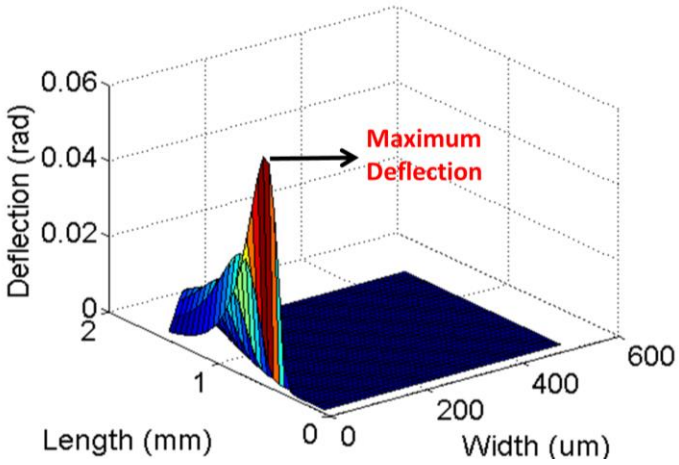

Figure 17: The deflection is plotted as a function of the length and width of the valve in order to optimize these parameters for the maximum deflection.

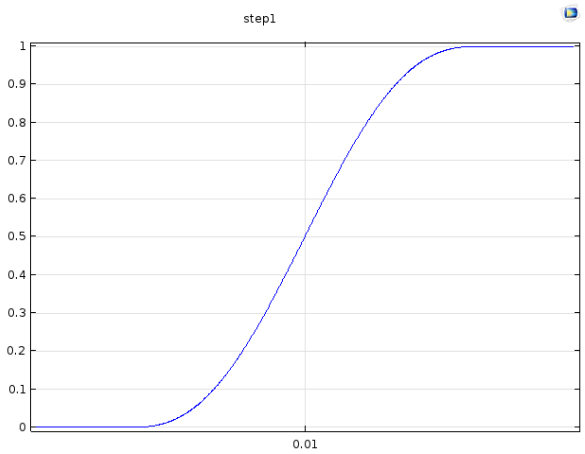

Figure 18: Step function used in the body load – takes 6 ms for the valve to move

The geometry of the channel used in the 2D simulation is shown in Figure 19b. Tip displacement (Figure 19a) and fluid velocity (Figure 19c) were determined using the results from the simulation at the tip point shown in red in Figure 19b.

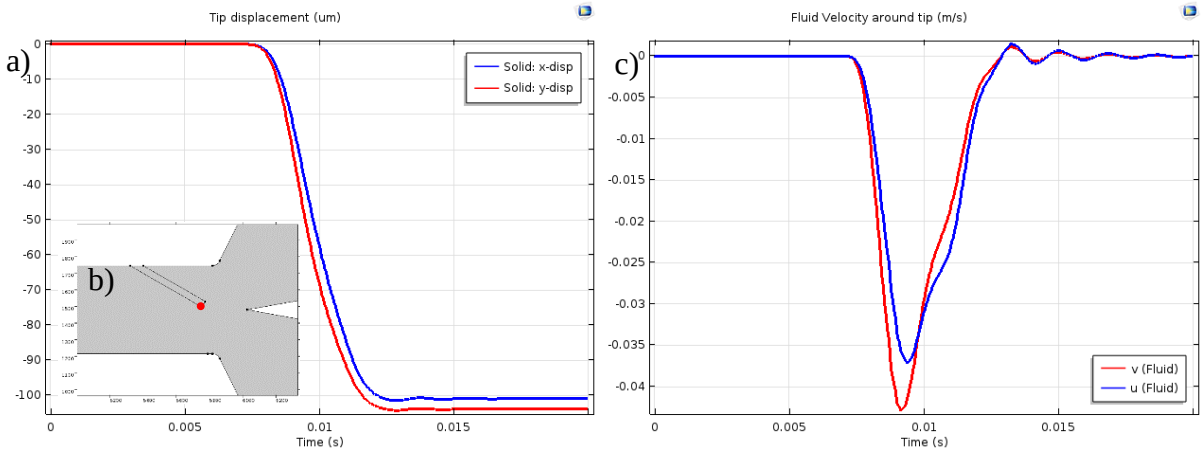

Figure 19: Results for the tip displacement (a) and fluid velocity (c) for the point shown in red in (b) are plotted.

The results from the simulation are presented in Figure 20. The default fluid velocity plot at the time point where the valve has reached its maximum deformation is shown in Figure 20a. Particle tracing is done on the results obtained from the FSI simulation using the Particle Tracing Module. A grid of particles (25 µm diameter) is released at t = 0 within an initial velocity of 0 and predicts how the experimental beads would respond to the valve movement and specifically helps to quantify the region where the beads would have to be located in order to be correctly sorted to the top outlet (outlet 1). The results of the Particle Tracing Module are shown in Figure 20b.

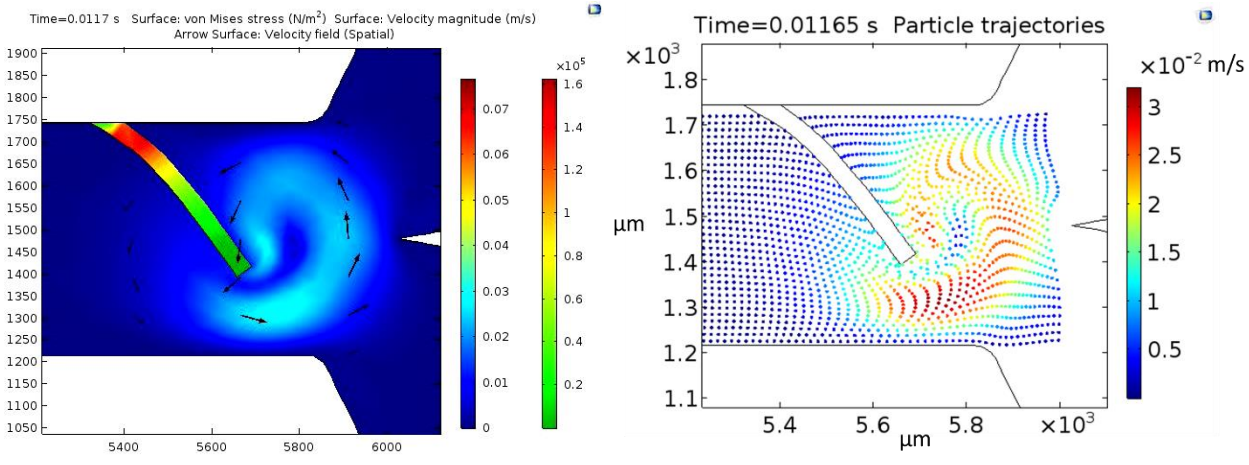

Figure 20: The results from the simulation are shown: a) snapshot of the velocity magnitude and von Mises stress at the maximum valve displacement b) snapshot of particle

locations and velocity at the maximum valve displacement, particle tracing is done on the fluid velocity field obtained in part a).

To compare the simulation to experimental results. The situation is replicated experimentally where the channel is filled with fluid but there is no pressure driven flow (static fluid). An input voltage is supplied to the system to produce the same valve deflection as the simulated case. The channel is seeded with particles around the valve that act as tracers. The initial particle locations from the experimental data are extracted and entered into the particle tracing module on COMSOL to obtain simulated particle trajectories. The simulated and experimental particle trajectories are then plotted in Figure 21. The trajectories show that the same rotational flow patterns exist in both cases. Better image processing tools to extract the particle trajectories for the experimental case can be developed. Furthermore, because of limitations stemming from a 2D simulation, the experimental and simulated trajectories will never match perfectly.

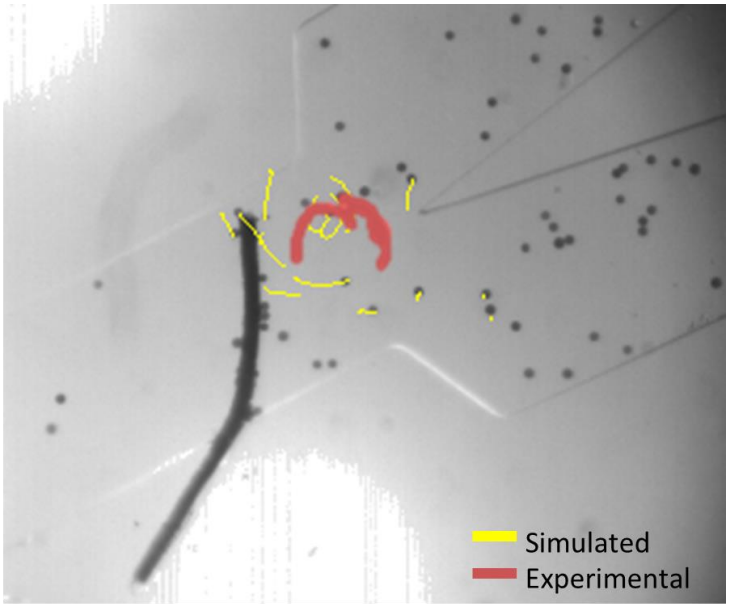

Figure 21: Experimental and simulated particle trajectories are shown.

The simulations are repeated with pressure driven flow and the fluid velocity and particle locations are plotted in Figure 22. Since only 2D simulations have been performed, one of the major limitations encountered is the lack of fluid flow in outlet 1. This increases the residence time for any particles sorted into outlet 1 significantly. In the experimental case, there is a 25 μm gap above and below the valve (a third of the channel height) which allows a significant amount

of the flow to go to this outlet (although no beads as those are centered using 3D flow focusing). To overcome these challenges, a 3D simulation is performed as a replica of the experimental geometry and the results are shown in Figure 25. Preliminary simulations were also done to optimize the channel geometry in order to take advantage of small valve deflections to sort beads (as shown in Figure 23).

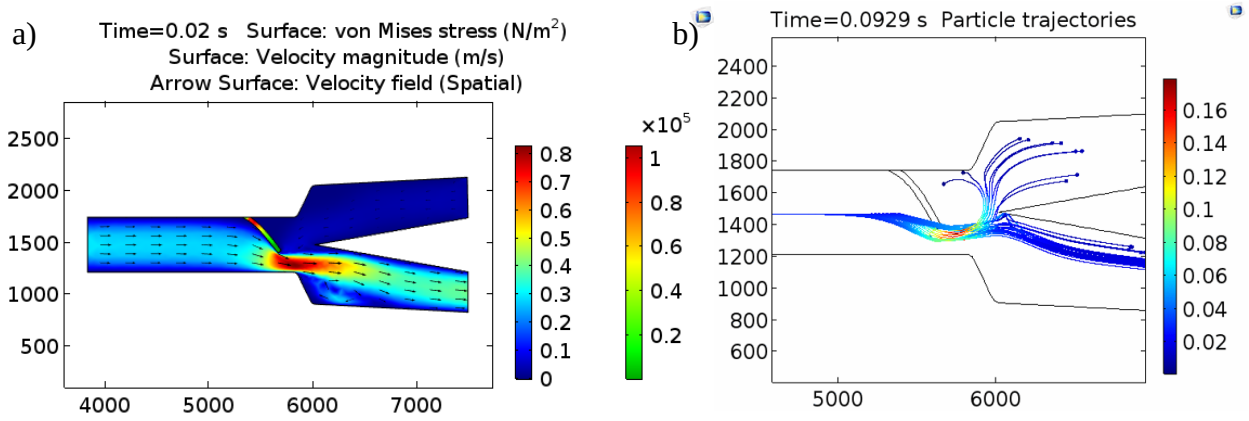

Figure 22: Simulation results including pressure driven flow, a) snapshot of the default fluid velocity plot after the maximum valve deformation and b) snapshot of particle tracing results after they have been correctly sorted. There are some particles still trapped in the bifurcation region (limitation of 2D simulation).

These preliminary numerical simulations are used to study how changes in channel geometry can allow even small valve deflections to successfully sort cells. It is hypothesized that increasing the channel width at the bifurcation region (see Figure 23a-b) would increase the distance a bead would travel transversely (even from a small valve deflection) allowing it to be accurately sorted. This is of importance in high frequency cases (above 1 kHz), when the valve deflection is significantly reduced due to fluid drag effects. Therefore, a parametric study is performed to study how amplification of the channel width at the bifurcation region can be correlated to small valve deflections (Figure 23). Preliminary results showed no differences resulted when the width of the bifurcation region was changed from 900 μm (Figure 23c) to 1300 μm (Figure 23d). Further investigation of these results showed that this is due to the fact that beads are currently sorted in the bifurcation region so changing its width accomplishes nothing. However, if the beads were sorted beforehand and then their distance amplified in the bifurcation region, the

hypothesis should hold. Therefore, further simulations can be done by moving the valve further upstream so that sorting is done within the inlet channel (before the bifurcation).

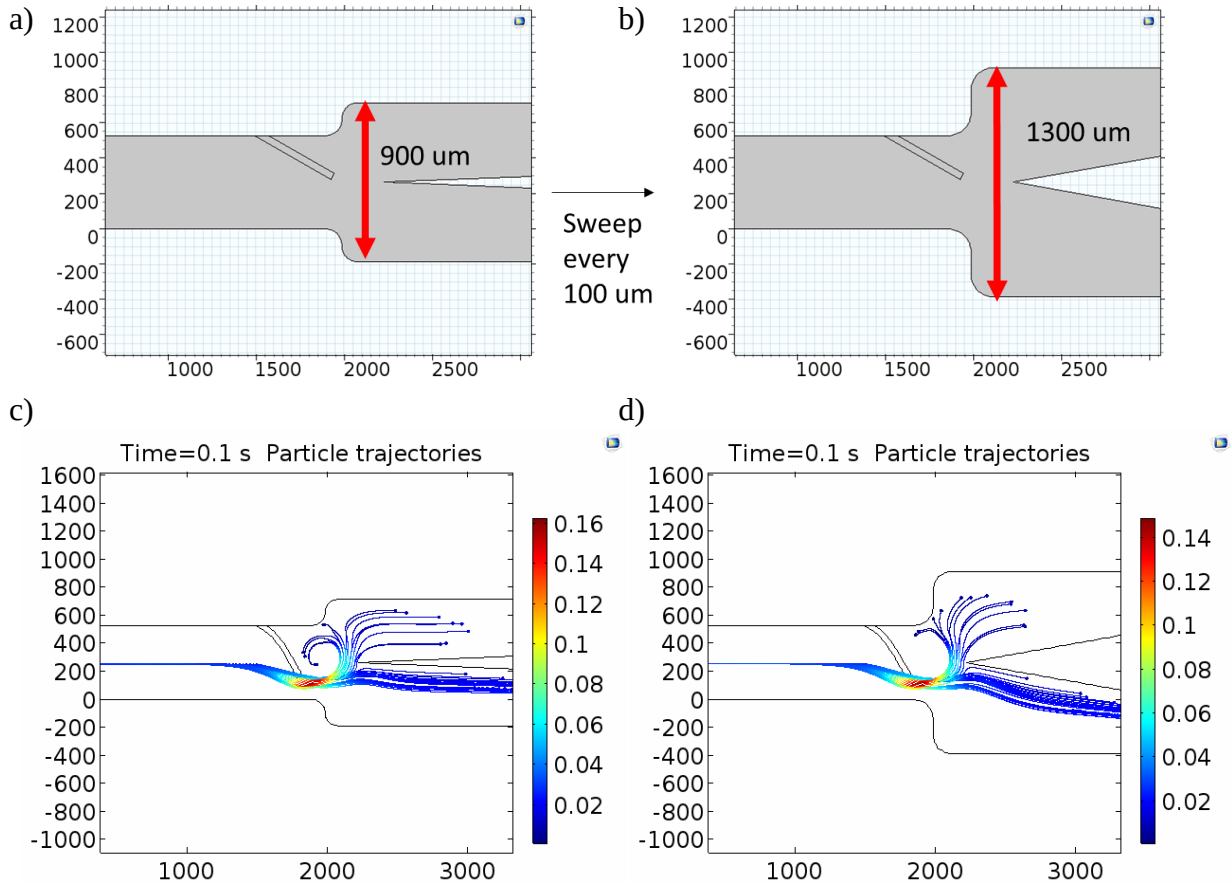

Figure 23: Parametric study performed for changing the width of the channel at the bifurcation region: a) geometry of 900 µm channel, b) geometry of 1300 µm channel, c) results for the 900 µm channel and d) results for the 1300 µm channel.

The parametric study results were also examined in terms of valve deflection where the overarching goal is to accurately sort even with small displacements as is the case for high frequencies. The valve displacement is not directly controlled but can be altered by changing the input force magnitude in the simulation or the magnetic field experimentally. Figure 24 shows the resulting valve displacements for a force magnitude of 0.5×10^7 and $4.5 \times 10^7 \frac{N}{m^3}$. As predicted, the number of beads that were accurately sorted were proportional to the force magnitude. At $0.5 \times 10^7 \frac{N}{m^3}$, no beads were sorted. If the smallest force magnitude (valve displacement) can be combined with the largest possible width at the bifurcation (1300 µm), then

accurate bead sorting should be possible at faster speeds. These combined parametric studies can be performed in the future.

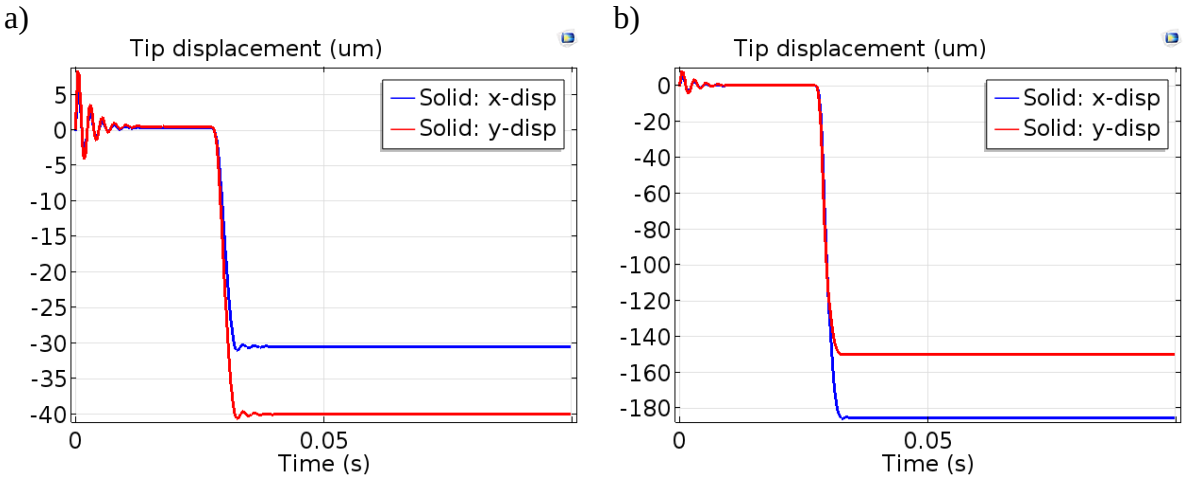

Figure 24: Valve tip displacements shown for two different input forces magnitudes: a) 0.5 x 10^7 N/m^3 and b) 4.5 x 10^7 N/m^3.

3.1.3 Results and Discussion

A microbead (BLPMS 20–27 μm, Cospheric) was sorted into the collection outlet to demonstrate the efficacy of the proposed valve. The top-view frames of the sorter during this process are shown in Figure 25a–c. The sample flow was slightly shifted so that incoming microbeads would go into the waste outlet if the valve remained stationary. However, the bead shown here was displaced by the fluid vortex induced by the valve deformation, which was caused by the applied magnetic field, and subsequently went into the collection outlet. The 3D ANSYS Workbench 16 simulation results of this sorting process are shown beneath experimental frames, with the microbead being enlarged for better visualization. The color of the path represents the microbead speed at that position.

As shown in this demonstration, a microbead needs to be caught by the fluid vortex created by the valve deformation in order to be successfully sorted into the collection outlet. In other words, the microbead must be within a specific region when the diverter deforms. This region is defined as the effective sorting region (ESR) and illustrated in Figure 25d. The position and size of ESR depend on the y position and x velocity of incoming microbeads, and the speed and magnitude of the valve deformation. The ESR is approximated as an ellipse between the valve tip and the

bifurcation point. It should be noted that the sorting is accomplished by the dynamic vortex, which disappears shortly after the diverter deformation. Without this dynamic vortex, all incoming objects will go into the waste outlet no matter whether the valve is deformed or not, as shown in Figure 25e and f.

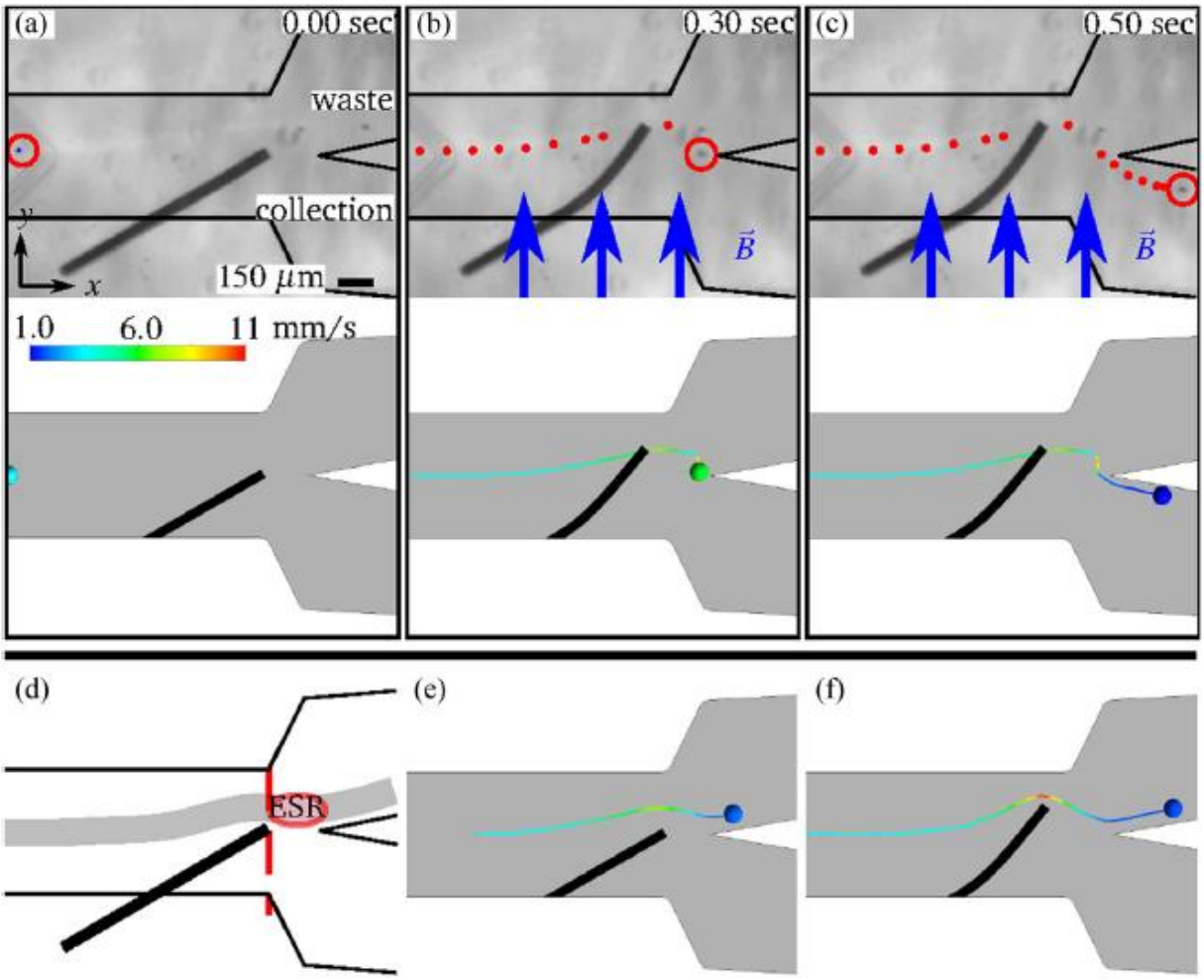

Figure 25: a-c) Experimental sorting results with ANSYS simulation results, d) effective sorting region, e-f) scenarios where the valve deforms while microbead is not the effective sorting region. © 2017, Springer Nature

3.1.4 Conclusions

Analysis on an existing cell sorting chip was performed using an analytical model and numerical simulations. The analytical model is used to understand the valve mechanics and to characterize a relationship between the input current and valve deflection. The goal of this modelling was to

optimize the valve geometry to obtain the maximum possible deflection. It was found that the valve deflection is maximized when the length of the valve is 1.3 mm and the width of the valve is 40 μm. The final geometry of the valve was set to 40 μm width and 1 mm length. The length was slightly smaller for practical reasons such as the width of the channel and to maintain smooth valve motion.

Numerical simulations were then performed to understand how the valve deflection affects the fluid flow in the surrounding region. The goal was to characterize the region where beads would have to be located in order to be accurately sorted and effective sorting region was characterized. First, experimental and simulated results were matched for a simple 2D simulation with no pressure driven flow. Then pressure driven flow was introduced into the channel and the region where the particles are accurately sorted was quantified. Here, one of the limitations of the 2D simulation was observed. It was noted that the positioning of the valve severely limits the amount of fluid flow to outlet 1. This increases the residence time of particles in the bifurcation region significantly. To match this to the experimental scenario, a 3D simulation was performed in ANSYS Workbench 16. The trajectory of a microbead was matched to the experimental scenario. The numerical simulation can be used to optimize the channel geometry to take advantage of small valve deflections. At high frequencies, the valve displacement is significantly reduced due to fluid drag effects. If these small displacements are still able to accurately sort the beads, then successful sorting at high frequencies can be achieved. Parametric studies can be done in the future to see how the channel width at the bifurcation region can be optimized as a function of the valve deflection.

The use of this optimized cell sorting chip will have some major advantages. The first (as seen through numerical simulations and experiments) is non-contact manipulation. The valve is used to control the path of the beads by altering the fluid flow around its tip rather than interact with the beads in anyway. There is also the potential of introducing multiple valves into the channel which will allow for an increase in productivity and specificity. Some limitations of this chip include low sorting speeds although this can theoretically be improved with more sophisticated equipment (such as high current amplifiers). Sorting at low frequencies (500 Hz) has been successfully achieved with promise for sorting at higher speeds. At high frequencies, fluid drag is a big limitation as it reduces the amount of deflection of the valve. Other limiting factors at

high frequencies include coil inductance and flow focusing. The manual fabrication of the device also has an impact on reproducibility and poses a challenge for any commercial use.

3.2 Local Stimulation of Osteocytes Using a Magnetically Actuated Oscillating Beam

3.2.1 Introduction

Mechanotransduction is an important process for basic cell functions, affecting cellular mechanisms from protein signalling to DNA transcription. Physical cues act as essential inputs to these mechanisms, ranging from mechanical loading of the cell to unique physical properties surrounding the cell [30, 31]. Although observed in a variety of organ systems, these physical cues are most prominent in load-bearing tissues such as the musculoskeletal system. In bone tissue, major mechano-sensory cells, osteocytes, are embedded in a network of lacuna-canaliculi exposing them to high levels of fluid shear stress upon bone tissue compression [32]. This mechanical stimulus is important for bone tissue function, as it activates key signalling pathways that regulate the bone remodelling process as well as tissue repair [33, 34]. Osteocytes seeded within flow-based *in vitro* systems have demonstrated their sensitivity to different levels of fluid shear stress [35-37]. However, current *in vitro* systems rely on macro-scale devices that stimulate a monolayer cell culture with standard uniform shear stress, in contrast with the pockets of shear stress experienced by osteocytes in the lacuna-canaliculi network [38, 39]. The rise of microfluidic systems has filled this gap by introducing cell culturing platforms at dimensions closer to that of the lacuna-canaliculi network, demanding development of newer fluid stimulation mechanisms suitable for this scale. Major cell response to flow in the form of intracellular calcium fluctuations have been successfully detected from osteocytes cultured using *in vitro* fluid flow systems [40-42], as well as *in vivo* models [43-45]. These calcium flux measurements demonstrate either the average response from a population of osteocytes or the single-cell calcium fluctuation pattern. However, is still very difficult to observe cellular response due to intercellular signalling transport from mechanically stimulated cells. Both *in vitro* experiments using patterned cell networks [46] and *ex vivo* studies using bone tissue [47] have shown the key role of calcium fluctuations play in propagation of signals between mechanically stimulated and non-stimulated osteocytes; however these studies rely on membrane disturbance and tissue strain as the mechanical stimulus, lacking the capability to study how fluid shear stress influence this signal propagation. Existing tools such as atomic force microscopy (AFM) can only provide point-force disturbances to the cell membrane and lack the capability to generate localized fluid shear stress that mimics the phenomenon within the lacuna-canaliculi

network where osteocytes are subjected to different level of shear stress. Hence there is a need for the development of a platform to locally stimulate a selected region of osteocyte culture with a shear stress to measure the varying response of osteocytes to mechanical stimulation, as well as response from intracellular signalling to non-stimulated cells. While local stimulation of cells has been attempted in the past [48], no study has attempted to quantify the shear stress gradient that can be generated through local non-contact cell manipulation.

This study aims to design a platform which can enable local cell mechanical stimulation by fluid shear stress in a targeted region. A magnetically actuated beam is placed above adherent cells and oscillated at a frequency of 1 Hz in order to generate shear stress on cells. The shear stress is localized to the region surrounding the beam, while cells further away from the stimulated region experience minimal shear stress. Finite element simulations are performed in order to quantify the shear stress values that can be generated by the oscillating magnetic beam. An experimental protocol is established with a specifically designed coil system and driving electronics integrated into an optical inverted microscope. Live imaging of intra-cellular calcium fluctuations is used to quantify cell response during magnetic actuation. A shear stress map is plotted along with the locations of all stimulated cells in order to illustrate the working principles of the device and to understand how future studies with local cell stimulation can be performed more reliably.

3.2.2 Methods

3.2.2.1 Design and Fabrication

Local stimulation of cells is achieved through the placement of a magnetically-actuated flexible beam above the adherent cell surface, which can generate localized shear stress regions [17]. The beam is manufactured as a flexible polymer with magnetic material embedded inside. It consists of a mixture of polydimethylsiloxane (PDMS, Sylgard 184, Dow Corning) which comes in two parts with a polymer base and curing agent that are combined in a 10:1 ratio by mass. This mixture is then mixed with permanent magnetic particles (MQFP-15-7, NdFeB, Magnequench) in a 1:1 mass ratio. This mixture is poured into a negative mold of the beam that was created using photolithography. The excess is scraped off with a razor blade. This mixture is fully cured on an 85°C hot plate for 4 hours and the beam is subsequently removed from the mold using a needle. After the beam has been removed, the magnetic particles inside the beam are magnetized

before assembly. The beam is placed in a uniform magnetic field of 1.1 T created by two permanent magnets (1-inch cube, NdFeB, N40, Magnet4US) placed 3 mm apart (see Figure 26).

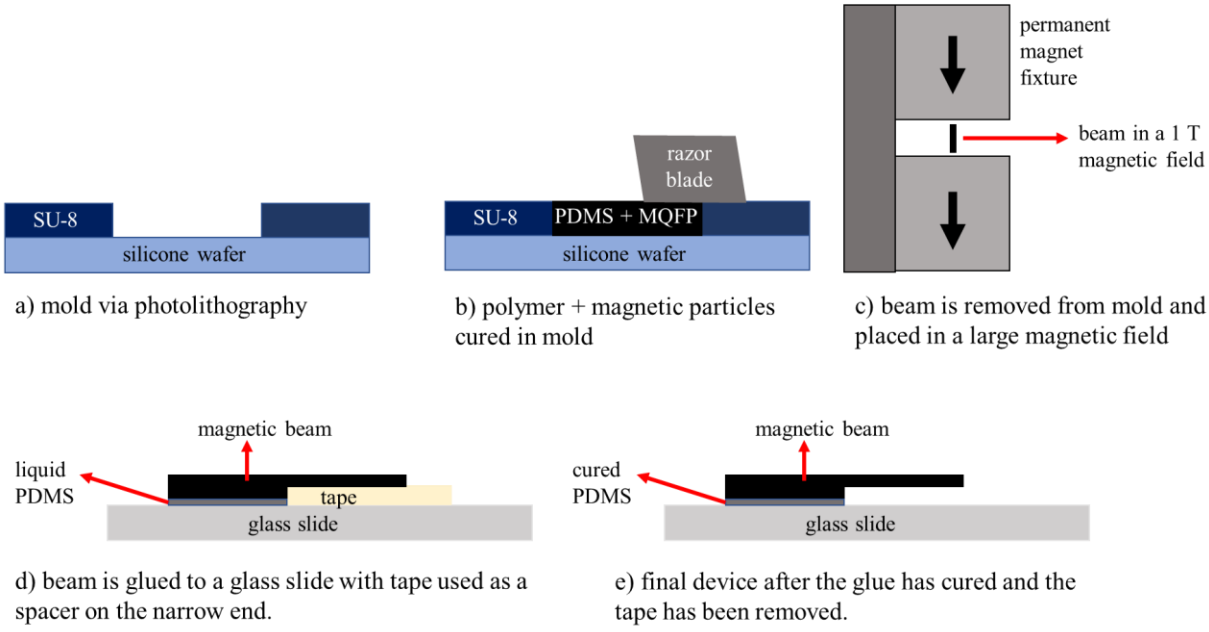

Figure 26: The fabrication process for the magnetically-actuated beam: i) a negative mold for the beam is created via photolithography, ii) A mixture of PDMS with magnetic particles is cured in the mold with any excess removed via a razor blade, iii) the beam is removed after curing and magnetized in a large magnetic field generated by two permanent magnets, iv) the magnetic beam is then glued to a glass slide using liquid PDMS and tape as a spacer and again cured, v) the final device when the spacer is removed after the device has been fully cured.

The beam is then glued using liquid PDMS to a glass slide with a spacer added to prevent the sinking of the beam. This is again cured on an 85°C hot plate for 4 hours. After curing, the spacer is removed. Separately, an adhesive film is added as a border to another glass slide on which cells are cultured. The slide with the beam is then flipped and placed on top of the cell surface. A small gap between the beam and the cell surface is necessary to ensure non-contact manipulation. Two different types of adhesives films are used to leave a gap height of 10 and 25 µm respectively. However, we will show in our results that cell stimulation was likely not achieved until the gap height was 5 µm as shear stress levels at higher gap heights are not sufficient. The small gap heights are achieved coincidentally in these set of experiments, but

future experiments can be designed to repeatedly achieve this gap height. The most common reasons for the experimental gap height to be smaller than the theoretical gap height is because of gravity which pulls the tip of the beam down when device is assembled or a thick layer of glue that pushes the whole structure downward (see Figure 27). The former would also result in an uneven shear stress gradient resulting in cells closer to the tip of the beam to be more easily stimulated due to higher shear stress levels while the latter would increase the shear stress uniformly across the localized region.

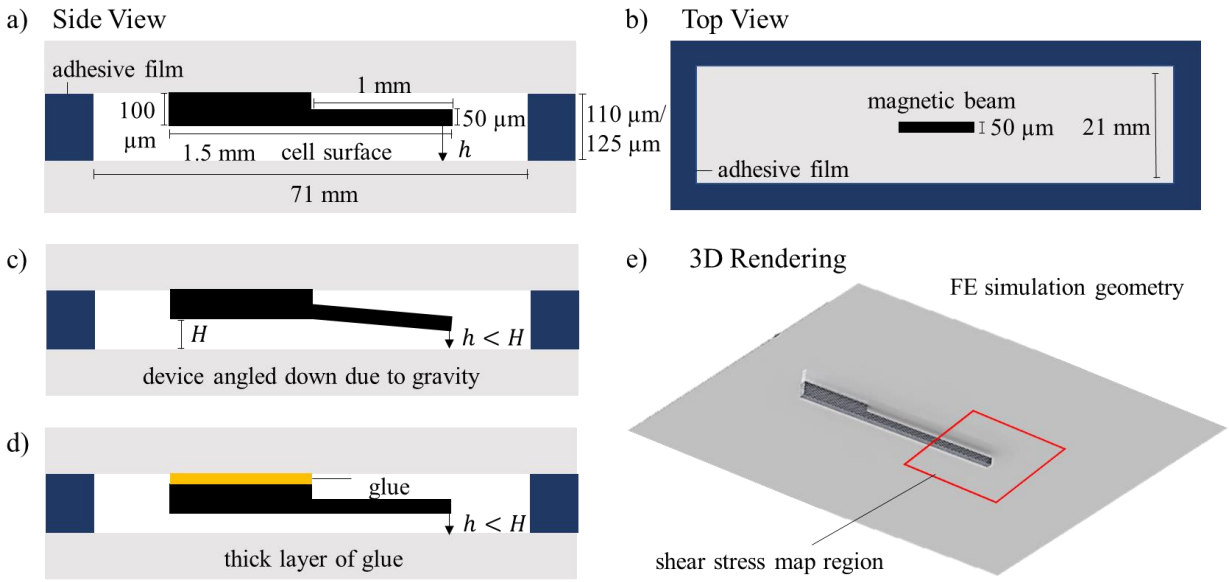

Figure 27: a) Side view of the fully assembled device where the magnetic beam sits a distance h above the cell surface, b) top view of the device is shown with the adhesive film border on the bottom slide and the magnetic device glued to the top glass slide. c) and d) show scenarios where the gap height h can be coincidentally reduced either due to the device being angled downwards due to gravity (c) or as a result of thick spacer or a thick layer of glue pushing the whole structure downwards (d). e) A 3D rendering of the geometry is shown. This is the geometry used in the finite element analysis. The red square shows the region where shear stress calculations were performed.

3.2.2.2 Experimental Setup

A pair of electromagnetic coils (Figure 28) were designed to fit around a fluorescent microscope. A large set of coils were designed with an 18 cm radius, 300 turns of an effective 7 AWG copper

wire mounted on a wooden structure that generates 10 mT in the center of the workspace. The device is placed in the center of the workspace such that the magnetization direction of the beam is perpendicular to the external magnetic flux density. An oscillating magnetic flux density of 10 mT at 1 Hz (Figure 29b) causes the beam to oscillate in the x-y plane [17] that results in shear stress on the cell surface. However, the magnitude of the shear stress must be greater than 0.8 Pa to result in cell stimulation, which occurs for very small beam-surface gap heights. The coil system is connected to an analog servo driver (30A8, Advanced Motion Controls) and power supply for tunable field generation. A signal generator is used to generate a 1 Hz sinusoidal waveform. The external magnetic flux density (B) results in a torque on the magnetic beam since the direction of magnetization (m) is placed perpendicular to the field direction. The resulting magnetic torque (T) is described by Eq. 3.13.

$$T = m \times B = mB \sin\theta \tag{3.13}$$

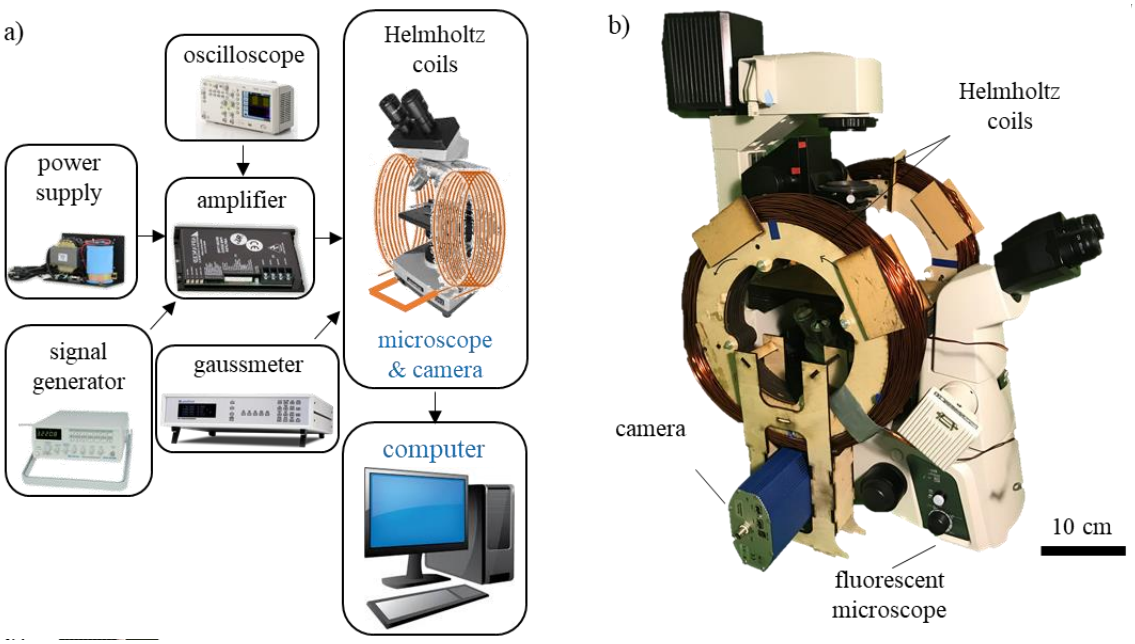

Figure 28: a) A schematic of the experimental setup is shown, b) the actual coils when placed around the microscope are shown. The 1D Helmholtz coils are specifically designed to fit around a fluorescent microscope connected. The coils are connected to an amplifier and power supply for current generation.

3.2.2.3 Finite Element Simulations and Analysis

To determine the shear stress that is applied to the cells and to understand how the results can be made reproducible, a set of fluid-structure interaction simulations were performed in ANSYS Workbench 17.1. These were repeated for different deflections with a gap height of 50 µm. The results of these simulations can be seen in Figure 29-Figure 30. A 3D geometry was constructed as shown in Figure 27e in ANSYS Workbench 17.1 with Transient Structural and Fluent components coupled together. A tip force was applied to the magnetic beam to match the average deflection seen in experiments. Note that the devices are all manually fabricated where small variations can result in large changes to the deflection profile of the beam. This simulation uses an average observed deflection, but this can be higher or lower for individual experiments resulting in higher or lower shear stress values. The magnetic physics was not modelled here since magnetic actuation is used to deflect the beam, which is easily observed experimentally, and therefore a model is not necessary to determine the shear stress. A sinusoidally oscillating force is applied to the beam which induces motion in the fluid. The resulting velocity data from the fluid domain was extracted from CFD Post for the 1 mm square shown in red in Figure 27e. For a 2D geometry, a spatial gradient of the velocity (u) data can be used to generate the shear stress (τ) results as shown in Eq. 3.14 where μ is the fluid viscosity.

$$\tau(z) = \mu \frac{\partial u}{\partial z} \tag{3.14}$$

$$\tau(\vec{u}) = \mu \nabla \vec{u} \tag{3.15}$$

$$\nabla \vec{u} = \begin{bmatrix} \frac{\partial u_x}{\partial x} & \frac{\partial u_x}{\partial y} & \frac{\partial u_x}{\partial z} \\ \frac{\partial u_y}{\partial x} & \frac{\partial u_y}{\partial y} & \frac{\partial u_y}{\partial z} \\ \frac{\partial u_z}{\partial x} & \frac{\partial u_z}{\partial y} & \frac{\partial u_z}{\partial z} \end{bmatrix} \tag{3.16}$$

When all components of the shear stress tensor were plotted, we observed that the results of the tensor are asymmetric, and this is likely a result of the vortices created by the beam oscillation and that the τ_{xz} is the largest component of the shear stress. This is in line with the design of our device where the magnetic beam is placed a certain gap height above the cell the surface and

oscillates in the *x* direction resulting in a large spatial gradient. To find the principal stresses of an asymmetric tensor is computationally intensive [49]. For our purposes, it is sufficient to conclude that all other elements are negligible and concentrate on the τ_{xz} component as the primary shear stress component leading to cell stimulation.

$$\tau_{xz} = \mu \frac{\partial u_x}{\partial z} \tag{3.17}$$

3.2.2.4 Analytical Model

A Couette flow model is used as a simplified model of the system. The Couette model consists of flow between two infinite plates separated by a distance h with one plate moving at a velocity U and the other plate held stationary as shown in Figure 29b. The shear stress for this simplified model is determined by Eq. 3.14 (the spatial gradient of the velocity). The geometry of motion in the setup of this paper differs from the Couette assumption in two main ways: 1) oscillating flow generated due to the back and forth motions and 2) edge effects of the beam. A correction factor for the oscillatory Couette flow is found in [50]. Since the Reynolds number for our flow is very small (with a peak of around 1.0), the oscillating flow correction is found to have negligible impact on the shear stress and does not need to be accounted for. In a simple Couette flow model, the entire top boundary is moving and is considered an infinite plate. Realistically, our beam has defined edges and we see from the finite element model of Figure 29 that some of the largest shear stress values occur near the edges of the beam. It has been shown in the past that edge effects increase the shear stress by a factor of 3 [50], however for our purposes we used the simple Couette flow model (Eq. 3.18) to obtain the shear stress values plotted in Figure 29f and h. Here, U is the plate velocity (or the tip velocity of the beam in our specific case), h is the gap height and z is the vertical distance from the stationary wall. The velocities used in the calculation of the shear stress using this model are determined using 1) finite element simulations and 2) theoretical velocities determined based on the tangential derivative of a sinusoidal wave of the beams' deflection profile as shown in Figure 29c. The theoretical velocity profile of the beam is also illustrated in Figure 29d. The fluid velocity at different vertical distances from the beam as shown by Eq. 3.19 are plotted in Figure 29e to show that the analytical Couette flow model and numerical simulations are in agreement. The in-plane component of the fluid velocity is also plotted versus varying beam tip deflections in Figure 29g.

$$\tau = \frac{\mu U}{h} \tag{3.18}$$

$$u(z) = \frac{\mu U z}{h} \tag{3.19}$$

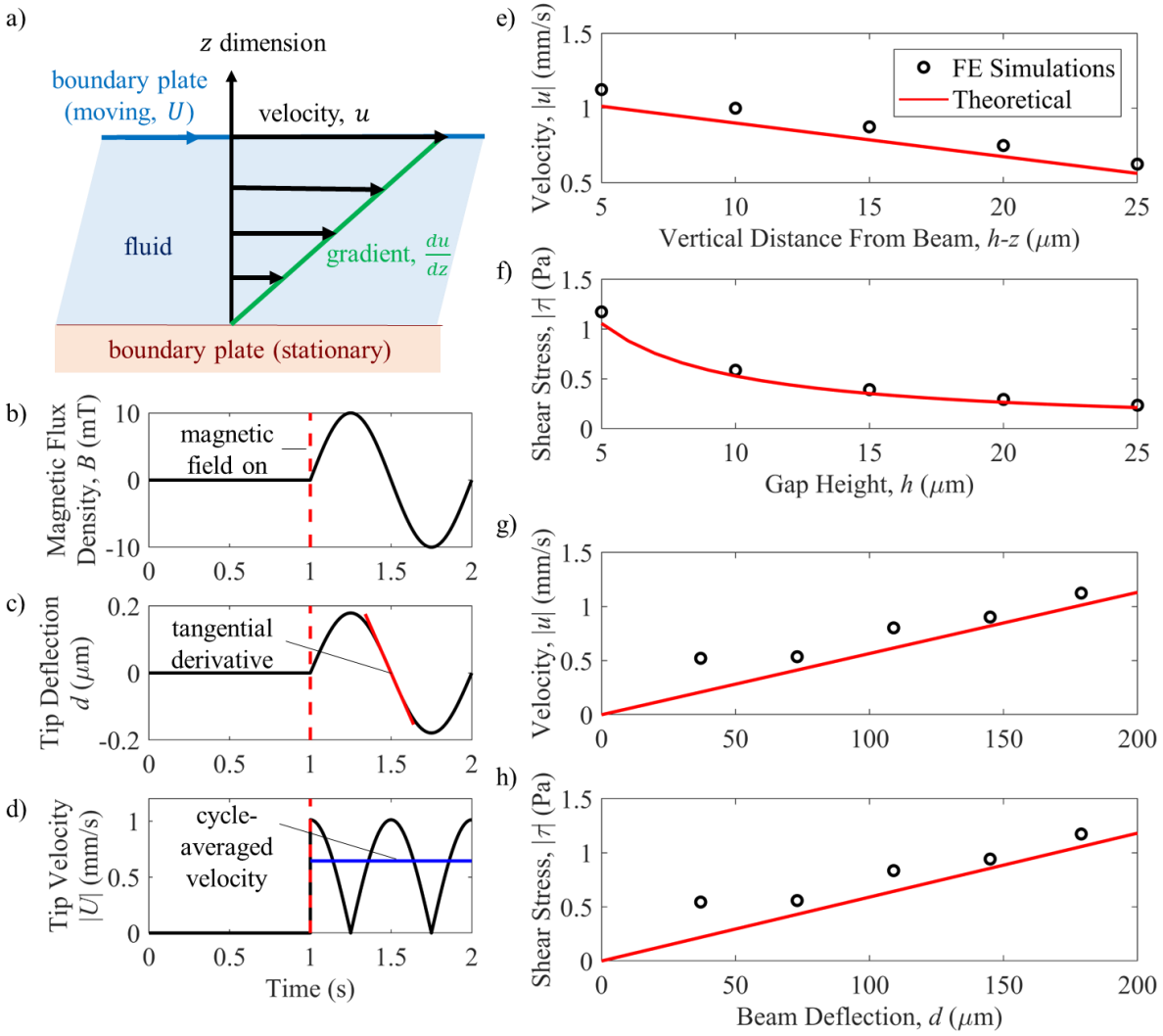

Figure 29: a) 2D Couette flow principle; b) magnetic flux density generated by the coils (shown for 2 s for posterity but this takes place over several minutes); c) the resulting theoretical deflection profile of the beam if the magnetic flux density in (b) is applied. This is also the profile used in the finite element analysis and the tangential derivative is used to determine the theoretical velocities shown in parts (e) and (g). d) The theoretical beam tip velocity magnitude as well as the cycle averaged velocity are shown for the deflection profile seen in (c). e) and g) are plotted using Eq. 7 with theoretical velocities determined

using the tangential derivative of the deflection profile and the numerical velocities determined from the finite element simulations. f) and h) show the shear stress with varying gap heights and beam tip deflection based on Eq. 6 using theoretical and numerical velocities.

3.2.2.5 Cell Culture

MLO-Y4 osteocytes (courtesy of Dr. Bonewald) are cultured in growth media composed of 2.5% calf serum (CS, Gibco, USA), 2.5% fetal bovine serum (FBS, Gibco, USA), 1% penicillin-streptomycin (PS, Gibco, USA), and 94% Alpha Minimum Essential Medium (MEM) (WISENT, Canada). Cells are seeded at 10^5 cells per 100 mm diameter collagen-coated (0.15 mg/ml Type I collagen (Corning, USA)) culture dishes until 80% confluency before transfer onto collagen-coated experimental slides for overnight incubation before imaging. MLO-Y4 cells are passaged and maintained at standard 37 ˚C and 5% carbon-dioxide environment.

3.2.2.6 Intracellular Calcium Imaging

MLO-Y4 cells are stained with Fura-2 AM intracellular calcium dye (ThermoFisher Scientific, USA) for 45 min at room temperature. After rinsing with phosphate-buffered saline (PBS, Sigma-Aldrich, USA), experimental slides seeded with stained cells are imaged by a Nikon Eclipse fluorescent microscope for 1-2 minutes before the magnetic field is turned on to oscillate the beam for up to 10 minutes. During experiments, cells are seeded in regular growth media supplemented with 4.6 mg/mL Dextran (500k MW) (Sigma–Aldrich) to achieve the needed shear stress value without significantly increasing the size of the beam. It has been previously shown that addition of Dextran to flow experiments using MLO-Y4 osteocytes does not affect their calcium response [51]. Fluorescent signals are read, and a ratio of 340 nm/380 nm signals is used to generate the calcium response curves. A calcium response is quantified as having 2-times fold-change or greater compared to baseline fluctuations measured in the initial 2 minutes of non-stimulated cells.

3.2.3 Results and Discussion

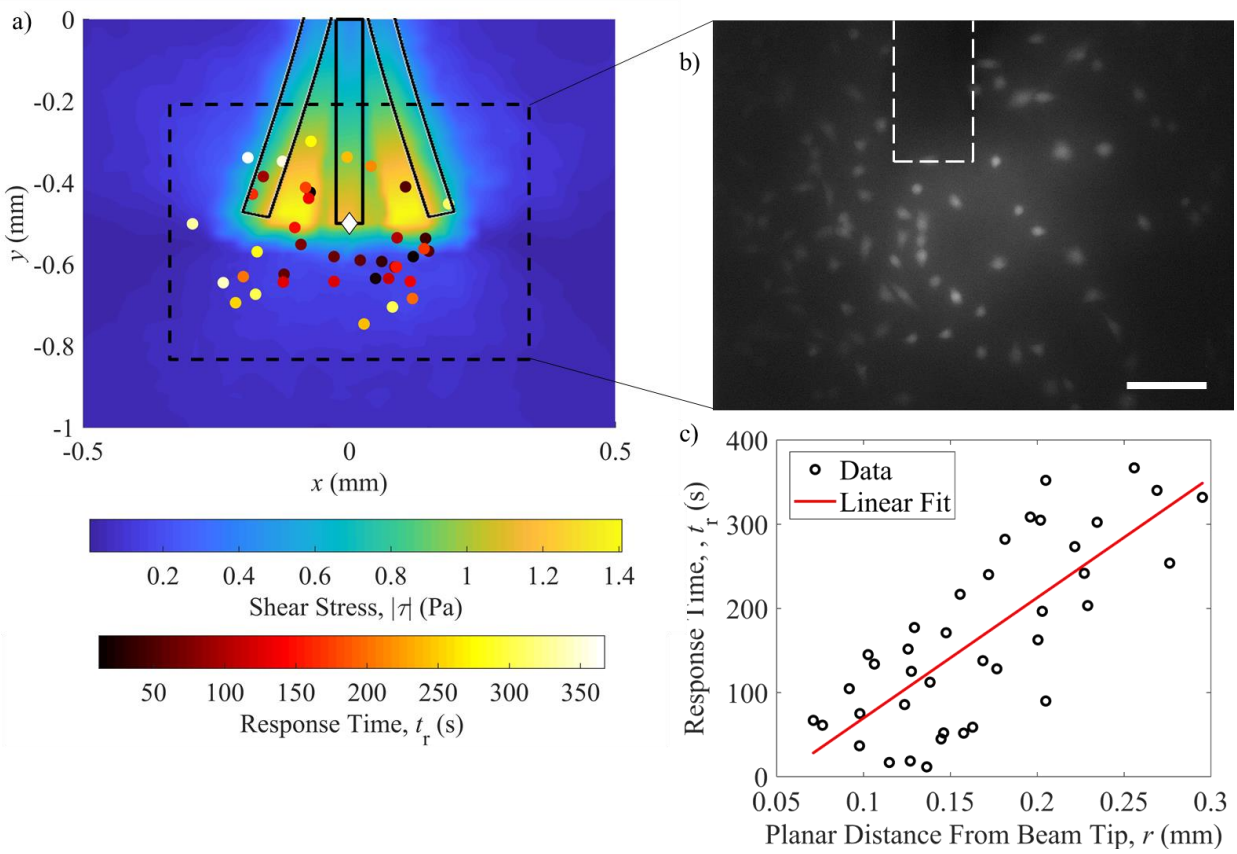

Figure 30: a) The shear stress map obtained using Eq. 6 with velocities obtained from finite element simulations is overlaid with the locations of responding cells that are coded with the time it takes to respond. The dotted line shows the typical viewing window in experiments and the range of the beam oscillation is also overlaid on the map. b) An image obtained of the cells along with the beam is shown which corresponds to the dotted lines on the shear stress map. Scale bar = 50 µm. c) A plot of the cell response time vs distance from the tip of the beam with a linear regression performed is shown.

We see from the analytical and numerical results of the shear stress values with different gap heights that large shear stress values are only obtained for very small gap heights below 10 µm and large beam tip deflection greater than 150 µm. In Figure 30a, we have plotted the maximum shear stress map resulting from the oscillation of the beam over 10 cycles in the 1 mm square region of interest around the beam tip. A microscope view of the beam and osteocytes is shown in Figure 30b. The maximum shear stress occurs in small areas around the beam oscillation which we refer to as the 'local stimulation region' (LSR). We see that cells in and around the

LSR are stimulated. We also observed cells being stimulated outside of the LSR where the shear stress magnitude was below the threshold required for cell stimulation. We have two hypotheses as to why this is the case; first, this could be the result of some form of cell response due to prolonged low magnitude shear stress, or secondly, a release of nutrients and chemicals from the stimulated cells in the LSR cross talk with cells outside the LSR to lead their response through intercellular communication. Also plotted here are the results of stimulated cells colour coded with a time stamp. It is observed in Figure 30c that the response time of the cells is correlated with the distance of that cell from the tip of the beam (Figure 30c and Figure 31a). This corroborates our earlier prediction that gravity is pulling down the tip of the beam resulting in higher shear stress levels near the tip and lower shear stress levels in the remaining LSR. The effect of gravity on the beam was also visually observed on multiple devices. The detailed calcium response of three cells is shown in Figure 31b.

As established in the literature, signals propagate within an osteocyte network through key molecules such as ATP and calcium. Despite the relatively far distance between the LSR and responding cells further away from the magnetic actuator, extracellular vesicles could play a key role in delivering signals at that range [47]; *in vitro* studies using cell indentation tools have shown it is difficult for calcium signals alone to propagate intracellular signalling beyond its neighbouring cells [46]. Furthermore, first peak response time of up to 300 s has been observed from distant cells. As this time is much longer than standard calcium fluctuation response time due to mechanical stimulation [40, 43], it can be implied that cellular response seen at this time scale is due to signal propagation from previously stimulated cells. However, future experiments involving fluorescent tracing of signal molecules will be required to confirm this hypothesis. Interestingly, there was no distinct difference in response characteristic between mechanically stimulated osteocytes and osteocytes outside of the stimulation region with a registered calcium response (data not shown). Similar peak magnitudes and frequency of multi-peak responses were observed in these near and far populations, with a slight, statistically non-significant trend towards higher response rate closer to the magnetic actuator (as can be seen by density of dots in Figure 30c). This is different from previous studies using cell membrane indentation, where a decrease in response magnitude was observed between stimulated and neighbouring non-stimulated cells [46]. With a prolonged stimulation time, it is possible that the concentration of signalling molecules increased to a threshold level capable of generating a comparable cellular

response as fluid shear stress. As there is an inherent difference between types of forces applied to the cell during fluid shear stress vs. cell membrane indentation, it is difficult to draw appropriate conclusions.

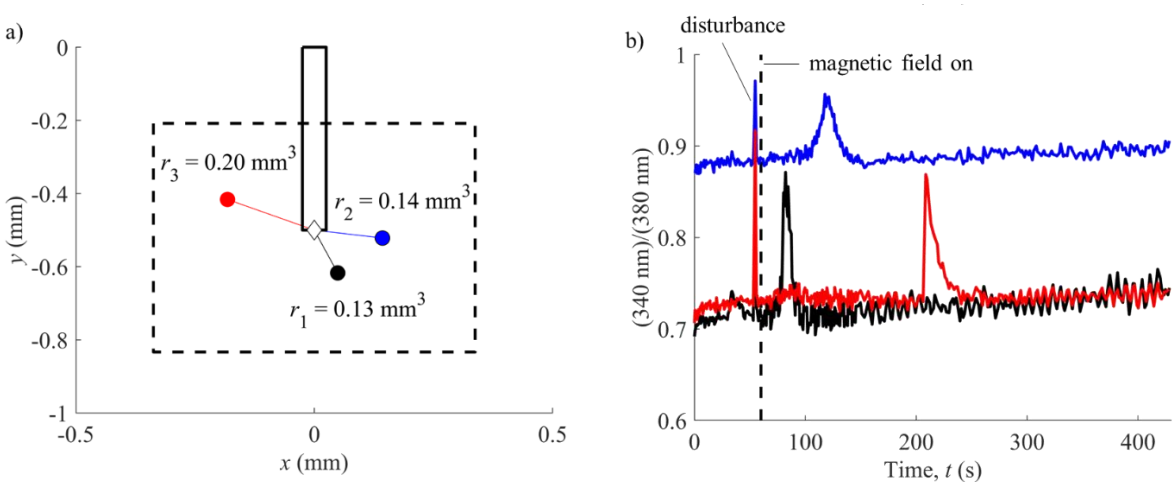

Figure 31: a) Three cells are plotted with respect to their positions from the tip of the beam, b) the calcium response of the corresponding cells from part (a) are shown.

3.2.4 Conclusions

A device design is proposed and fabricated in order to locally stimulate cells. The device was employed experimentally, and cells under direct beam oscillation induced shear stress were found to respond with intracellular calcium concentration increase. A set of finite element simulations were performed in order to obtain a shear stress map and a small LSR region was found at a gap height of 5 µm. Over time, cells outside the LSR also respond. We postulate that this could be the result of communication between cells from the LSR or due to prolonged application of low magnitude shear stress. Future experiments can be made more reproducible by controlling the gap height more precisely in device fabrication. Another easy way of increasing the shear stress is to increase the viscosity of the fluid which has been shown to increase the shear stress on the cells [51]. Future studies will aim to place the beam inside microfluidic channels in order to do more in depth molecular analysis. A microfluidic device will allow for future studies of osteocyte network signalling with physiologically accurate localized shear stress gradient.

Chapter 4
Mobile Untethered Surgical Tools

Current minimally invasive surgical tools suffer from lack of scalability and restricted access to some surgical sites using a laparoscopic probe. This chapter introduces a proof-of-concept prototype of the first completely wireless surgical scissors capable of dexterous motion and cutting in a remote environment as a mobile microrobotic device. The 15 mm untethered surgical scissors are custom made from sharpened titanium sheets with a magnet on each blade for actuating force and control. A super-elastic nitinol wire acts as a restoring spring and results in a simple design with no pin joint which is difficult to fabricate at small sizes. To actuate and control the scissors, a 3D magnetic coil system is used here for testing and demonstration. An external magnetic flux density of 20 mT can be generated using the coils and is used for cutting as well as orienting, moving and closing the scissors. In this first prototype setup, the scissors can generate up to 75 mN of cutting force, and we demonstrate the cutting of agar. As a proof of concept demonstration of the potential use of the scissors as a completely untethered surgical tool, we robotically maneuver the scissors to a target location in a confined environment where they cut through agar and return to their initial position. The scissors are then deployed inside a mock surgical setting where they are used to cut through the brain tissue of a goat.

Some of these results have been published in (Reprinted with permission IEEE 2019):

O. Onaizah and E. Diller, "Tetherless Mobile Micro-Surgical Scissors Using Magnetic Actuation," in *2019 International Conference on Robotics and Automation (ICRA)*, 2019, pp. 894-899 [52]

4 Mobile Untethered Surgical Tools

4.1 Motivation

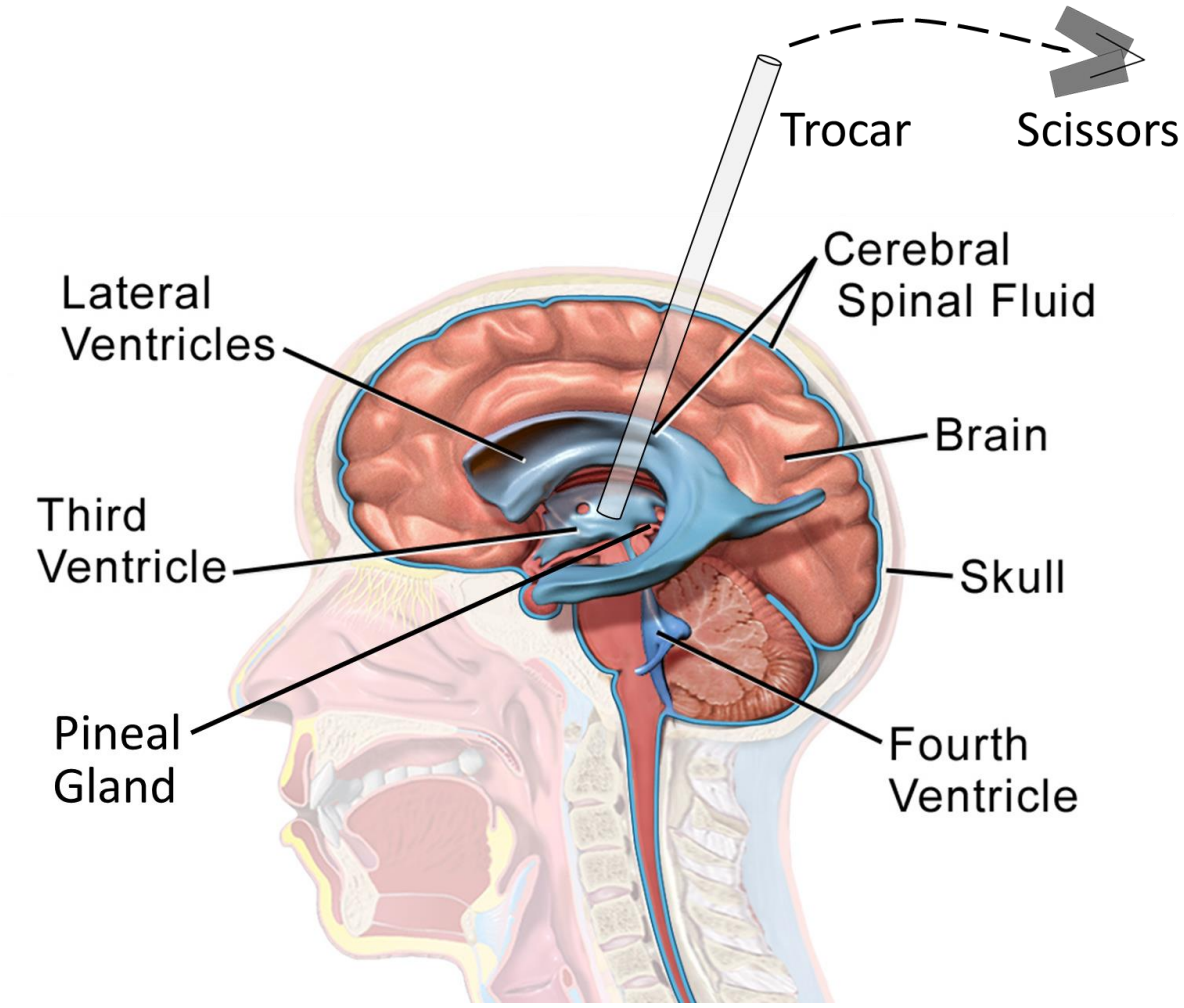

Figure 32: Rendering of a human brain showing the location of all four ventricles as well as the pineal gland which is the location of all pineal tumours and easily accessible via the ventricles. A trocar in inserted into the ventricles and the scissors are deployed through the trocar into the ventricles.

Pineal tumours are tumours that develop in the pineal gland which is located deep inside the brain close to the connection between the third and fourth ventricles. Pineal tumours account for up to 2.7% of the tumours that can develop in children [53]. The ventricles are fluid filled cavities in the brain. Operation of small-scale robotic tools inside the ventricles is often easier since these tools do not have to navigate and push through tissue and can often move around

more easily inside a fluid filled region. Since the pineal gland is easily accessible through the ventricles, pineal tumours can be removed using minimally invasive procedures. In this case, a small hole would be drilled in the skull (about 9 mm wide) through which a trocar is pushed into the ventricles. Surgical tools can then be deployed through this trocar into the ventricles. All four ventricles are connected; however, the connections are often narrow and would require tools that can easily bend around corners and access the small, constrained spaces.

Minimally invasive surgery using laparoscopic and robotic tools has become an increasingly common surgical practice as it minimizes damage to the site, speeds up recovery time and results in fewer complications compared to open surgery [54]. However, challenges to this type of surgery include the use of rigid tools with limited maneuverability, dexterity and minimal degrees of freedom. Robotic tools such as the da Vinci system by Intuitive Surgical [55] allow surgeons to operate away from the tableside using a dexterous controller. Distal tools such as the EndoWrist® instruments by Intuitive Surgical allows for complex tissue manipulation and even suturing by allowing a full rotation of the wrist with tool width as small as 5 mm [54]. These tools are still rigid, unable to maneuver around corners with limited dexterity and therefore have only been adopted in the fields of urology, gynecology, gastroenterology and orthopedics where surgical workspaces are larger and fewer anatomical challenges exist [56].

To access further into the body and overcome some of these limitations, researchers have been developing robotic distal tools which can bend and flex in a tight workspace with a relatively high level of dexterity [57-59]. While these snake-like robots only require one port of entry, one of the biggest limitations of these robots is that due to compliance and motion losses and friction, the position of the end effector cannot always be precisely controlled [60, 61]. The requirement for the use of a single access-point may still necessitate complex surgical planning to reach some sites [62] and severely limits the maneuverability once the tool has navigated to the surgical site.

Completely untethered microrobotic tools have potential to overcome many of these limitations by accessing very small spaces, offering more dexterity [63] and potentially enabling access to areas in the body which are currently inaccessible for minimally invasive procedures. Untethered microrobotic tools have been studied for biopsy and drug delivery applications [64-66] as well as removal of plaque in arteries and blood clots [67], while tissue penetration has been shown with certain tools such as needles [68], and magnetic hammers [69]. However, cutting of soft tissues

in a dexterous manner using untethered microrobotic tools such as scissors remains an unexplored problem. The purpose of this work is to test whether a wireless surgical scissors can be developed which can move and cut tissue robotically at a millimeter to centimeter size scale. Leveraging recent advances in microrobotic actuation using magnetic fields [6], we seek to show that adequate cutting force can be achieved and delivered to a simple surgical scissor mechanism which can also be moved in a dexterous manner.

Magnetic actuation is a commonly used remote actuation technique in the field of small-scale robotics because of its ability to penetrate most environments, generate both force and torque at relatively high speed and because it is safe for use in the human body [63]. Since no on-board power sources are required for magnetic actuation of small tools, scaling down devices even to the single-cell size is possible [70]. Magnetic fields can be generated for dexterous multi-degree-of-freedom manipulation using electromagnets [13] or permanent magnets [14]. Cutting with some untethered magnetically-actuated tools in other applications such as a capsule robot for sampling inside the GI tract [71] and single-cell cutting in an on-chip micro-scale device [72] has been previously demonstrated. However, these designs are not suitable for surgical cutting because they rely on single-use mechanisms or large on-chip actuating magnets and do not generate a scissor motion in a wireless and maneuverable device.

Thus, this study presents the first prototype of an untethered pair of scissors that are magnetically actuated for cutting of soft tissues. The key challenges which must be addressed for the design of viable surgical scissors in a wireless device are a) enforcing a good scissor blade contact and b) achieving a force output large enough to cut tissue. A primary challenge in cutting tissue using a wireless device is in achieving adequate force. The force required for cutting soft tissues varies in the literature and most of these results have been obtained by measuring forces required to penetrate tissue using needles. Tissue penetration forces using needles have been measured to be 2.5 mN for mouse brain [73] up to 1 N for porcine tissue [74]. Cutting forces using scissors have also been studied for rat and sheep tissues including the liver and were found to be 1.6 N and 7.1 N respectively [75]. It is important to note that these forces varied with the type of scissors and cutting speed used and closing the scissors without cutting required 3.6 N, signifying that these scissors have a very high amount of friction present in the mechanism.

This study outlines the design and fabrication of the prototype scissors and actuating magnetic coil system. As a design tool, a model of scissor cutting is developed and used to optimize the magnetic placement on the scissors. The cutting force is measured, and a demonstration is conducted whereby the scissors are maneuvered from their initial position to a target location where they slice through agarose gel and then return to their initial position. The scissors are then actuated in a mock surgical setting using the same actuation mechanism in order to cut through the brain tissue of a piglet.

4.2 Physics of Cutting

Tissue cutting is the process of machining tissues both inside the human body and *ex vivo* [76]. This includes both the cutting of bone tissues as well as soft tissues. Bone is a hard material and therefore exhibits more predictable behaviour which allows already established fracture mechanics and metal machining techniques to be used. Soft tissue cutting mechanics are more complicated and literature around this is not as comprehensive. In general, cutting does not involve separating atoms or breaking atomic bonds which would require a lot more energy. Cutting is just an expansion of space that already exists between molecules. Therefore, some materials are a lot easier to cut than others because of the arrangement of molecules within. For example: diamond is nearly impossible to cut because it is essentially just one large molecule. This also explains why cutting is often easier in certain directions or orientations; for example: think of your steak or even a piece of cloth.

Almost all surgeons require some sort of cutting tool when dealing with soft tissues [77]. Often, the cutting force is modelled as a constant value set to a specific threshold in most models. This I value depends on the specific tool and tissue being cut and is often experimentally determined. Recent modelling approaches have tried to move towards predictive approaches accounting for different scenarios [77, 78]. Fracture mechanics has been adopted as the primary approach to predict cutting force [79-82].

Cutting of soft tissues is reliant on three main forces: cutting force, frictional force, and the elastic force of tissue deformation [77, 83]. A large body of work around cutting has focused on needle insertions and have considered the frictional and elastic forces to be the dominant factors. This is especially true and a long and thin needle. As previously stated, the cutting force was often modeled as a constant acting on the tip of the needle [68]. There is a large amount of literature on

the elastic or viscoelastic modeling of tissue mechanics and deformation and on cutting mechanics in general. It is a well-established research area relying on fracture mechanics. However, there is a lack of literature bridging this gap. Cutting of soft tissues remains a largely unexplored area although needle insertion maybe an exception though it tends to focus on elastic deformation [84, 85]. The cutting force plays an important role as it is directly related to tissue damage. The goal of this study though is to focus not on the cutting mechanics but rather device design that achieves the desired cutting forces. Cutting is one of the most fundamental surgical tasks [86]. Minimally invasive procedures typically use laparoscopic scissors for cutting and the same two principles apply here: 1) deformation and 2) fracture. When the deformation reaches a certain threshold; fracture occurs. This process is outlined below in Figure 33.

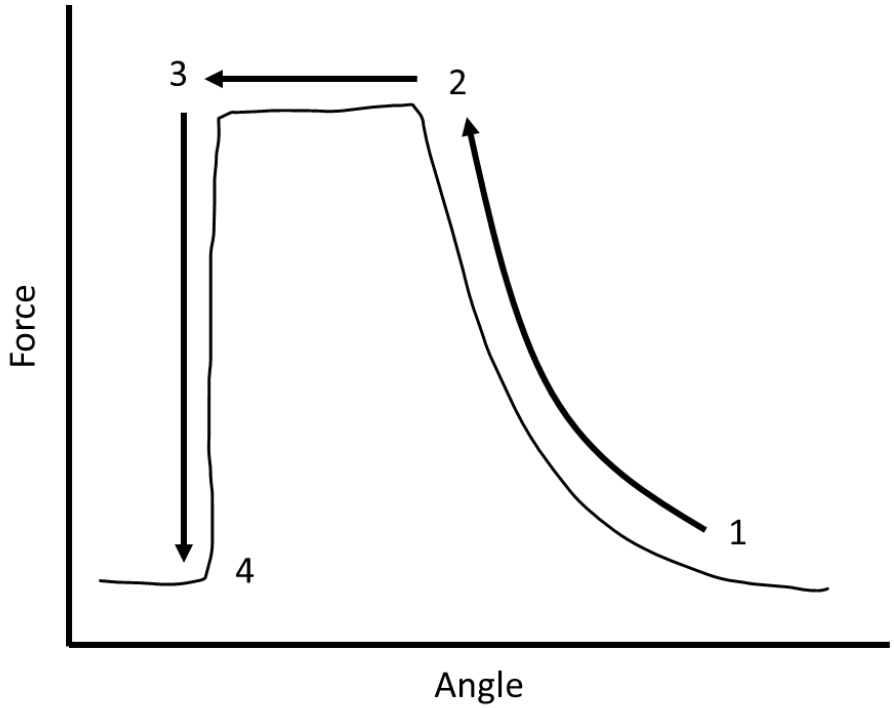

Figure 33: Depiction of cutting with laparoscopic scissors. 1)-2) Force increases as the handle closes (contact region), 2) fracture starts to occurs, 2)-3) fracture propagates as the handle closes (cutting region), 3)-4) scissors blades completes cutting and fully closes (completion region).

In addition to fracture mechanics which will be discussed in detail in the next section, tissue-tool interaction also relies heavily on the type of tool being used. [83, 87, 88]. Changing the geometry of the tool by adding a serrated edge to the blade or increasing the sharpness can play a big role

in decreasing the amount of force needed to cut through tissue. In fact, research has shown that even changing the velocity of a needle during insertion or the diameter of the tip can change the amount of force needed to cut through the tissue. The benefits of vibrational cutting are well known in the literature and again adding a vibrating element has been shown to decrease the forces required for cutting [83].

4.3 Cutting Force and Fracture Mechanics

Fracture Toughness is a material property that is used to indicate the ability of a material to resist the propagation of cracks [89]. Typically, the higher the fracture toughness the harder the material is to cut. A typical test for measuring fracture toughness involves measuring the energy required to propagate a crack in a material. This material property is used to describe the 'defect tolerance' or in other words the ability to handle the presence of cracks or other defects without significant loss of strength [89]. The fracture toughness of specific materials is listed in Table 2 below [90]. It is clear from this data that the fracture toughness of soft tissues (in this case chicken skin) is typically smaller meaning they are easier to cut than hard materials. The fracture toughness of some soft mammalian tissues and bio-gels has been explored [91-97] but the numbers vary depending on the tool and technique used and no current standard exists for how this should be measured for soft tissues.

Table 2: Fracture Toughness of selected materials [90].

Material	**Fracture Toughness ($\mathbf{kJ/m^2}$)**
Paper	4.9
Plastic	3.17
Cloth	2.43
Chicken Skin	2.8

Cutting force is typically referred to as the force required to achieve fracture in the first place. The cutting force is often used because fracture toughness or strain energy are not easy parameters to determine. The problem is that the cutting force is highly dependent on the tool being used and therefore even slight variations in blade sharpness, geometry or orientation can have large affects on the cutting force required.

New research has also cast doubt on the use for fracture mechanics to model cutting of soft tissues. This is because fracture mechanics relies heavily on the normal forces exerted on the material during the cutting process. Often, shear forces are much more successful in cutting soft tissues than normal forces. For example: when cutting a tomato using a knife, it is usually sliced with a back and forth shearing motion. Just applying a normal force would result in squashing the tomato rather than slicing it. This is also true for paper cuts. The paper shears across the skin and using the paper to apply a normal force would achieve nothing. Researchers sliced agar with both normal and shear forces and discovered that shear forces led to lower deformations and thus cutting forces [78].

4.4 Methods and Materials

4.4.1 Design and Fabrication

The proposed prototype design of the scissors features a sandwiched blade structure which minimizes the offset between the blades and keeps them together using a simple design without a pin joint. Cutting with scissors relies on shear forces that arise due to the blades moving on each other. A typical pair of scissors will have a pin joint to keep the blades in close contact. However, on the millimeter scale, this introduces a large amount of friction that tends to jam the actuation. The sandwich blade design naturally keeps the blades together. The blade motion is constrained by a restoring spring which allows the scissors to be closed and opened with a single control input. The scissor design is shown in Figure 34a. On-board actuation is accomplished by two magnets (with magnetic moment $\boldsymbol{m_1}$ and $\boldsymbol{m_2}$) which are placed at angles (β_1, β_2) as shown in the figure to have a net magnetization direction along the y-axis to orient and move the scissors. Assuming β_1 and β_2 are identical, the net magnetic moment of the entire scissors is

$$m_{net} = m(\sin\beta_1 + \sin\beta_2), \tag{4.1}$$

where m is the magnitude of the magnetic moment of one magnet. The resulting torque is used align the entire scissors to an externally applied magnetic flux density ($\boldsymbol{B}$) and is given by

$$\boldsymbol{\tau_{net}} = \boldsymbol{m_{net}} \times \boldsymbol{B}, \tag{4.2}$$

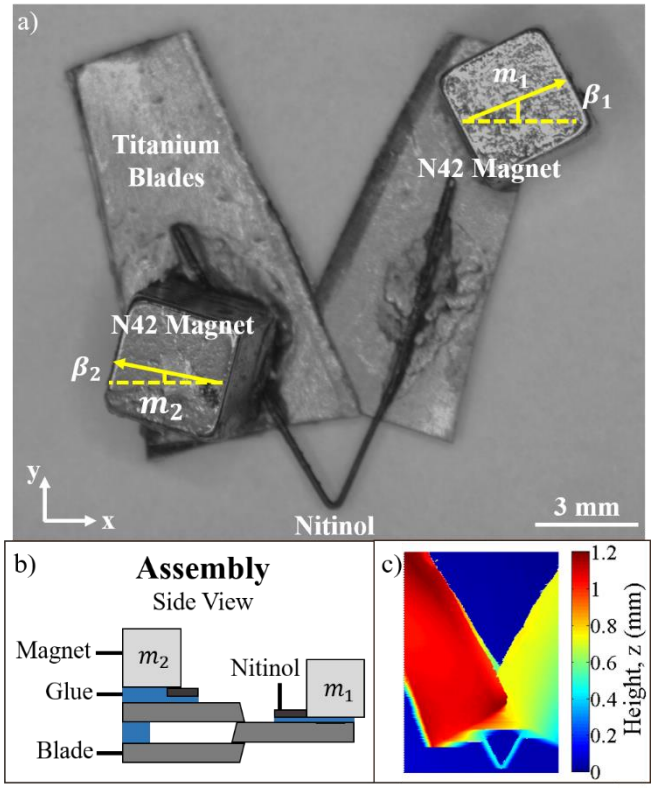

Figure 34: Scissor design. a) The top view of the scissors showing the layout of blades, magnets and restoring nitinol spring. b) Schematic of scissor design. c) The height of the scissors without the magnets mounted. © 2019 IEEE

The scissor prototype is custom-made in three manual fabrication steps: 1) grinding, 2) sharpening and 3) assembly. First a thin sheet of titanium (0.1 mm) is cut into a small rectangular strip and then one edge is coarsely ground on a 60-grit wheel. This edge is then sharpened and smoothed on a whetstone with 1000-grit and then 4000-grit. The rectangular strip is then cut into the desired shape as shown in Figure 34a and the scissors are then assembled as shown in Figure 34b. In this case, a nitinol wire with 193 µm diameter is glued manually using Super Glue. A 3.18 mm cube neodymium iron boron (NdFeB) permanent magnet (grade N42, K&J Magnetics) is mounted on each blade. An angle of 15° for β_1 and β_2 is chosen to provide a net magnetization in the vertical direction to the scissors to allow for movement of the entire device as a mobile microrobotic agent as seen in Eq. 4.1. When an external magnetic field (***B***) is applied, each magnet experiences a magnetic torque which pulls it into alignment with the applied field. These torques close the scissors until the torque is balanced by the nitinol restoring spring. When the magnetic field is removed, the scissors spring back open to their original

configuration. All components here were glued together but can also be laser spot welded together.

The height of the top surface of a flipped pair of scissors was measured to ensure that the blades were in sufficiently close contact to allow for cutting. Figure 34c shows the height (z) of the scissors as measured using a laser scanner (scanCONTROL 2900-10/BL, Micro-Epsilon). The offset between the top blade and the sandwiched blade is approximately $250\ \mu m$, which is also the gap between the bottom blade and the sandwiched blade. Since the thickness of the blades is $100\ \mu m$, this shows that blades are in close contact.

4.4.2 Experimental Setup and Control

A 3-axis electromagnetic coil system is used for all experimental results as shown in Figure 35. The coils can supply a maximum uniform field of $20\ mT$ in all three directions. The coils are loops of wires arranged in an approximate Helmholtz configuration and each coil is powered by currents supplied by an amplifier (30A8, Advanced Motion Controls), with details given in [66]. If the currents are applied in the same direction, a uniform field can be generated in the center of the workspace. The coils enclose a region of uniform field of approximately 2 cm cube. The scissors are actuated to the target location using open loop control with a game controller. Stick slip motion is used to move the scissors forward on a planar surface, as has been demonstrated in previous works [98]. A $5\ mT$ sawtooth wave with a frequency of $2\ Hz$ is applied in the z-direction with a constant field of $2\ mT$ in the planar direction of motion (x or y). In this way, the scissors rock back and forth, taking a small step (approximately $500\ \mu m$ each time). The scissors are steered by changing the direction of the horizontal field. Motion of the scissors for cutting, moving and standby modes can be teleoperated or controlled using a high-level feedback controller in future works. Two firewire cameras (FOculus FO124TC) are used for visualization purposes (top view and side view, Figure 35). The material selected for the cutting demonstration was agarose gel with a concentration of $0.4 - 0.6\%$ powder because it has been found to have similar mechanical properties to brain tissue [99].

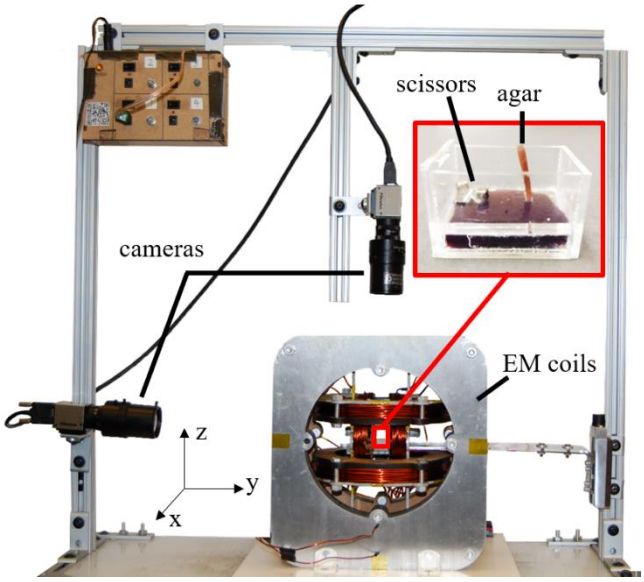

Figure 35: The actuation setup used for all experiments. A box with the pair of scissors and agar is placed inside the 3 axis Helmholtz coil system and viewed using two cameras (top view and side view).

4.4.3 Modelling and Design Optimization

To enable optimization of the scissors design, a model of cutting action was developed. One critical design parameter is the placement of the actuating magnets to minimize the effect of inter-magnet forces and torques which can result in poor actuation performance if not controlled. We thus aim to obtain the optimal location for the placement of the magnet ($\boldsymbol{m_2}$) in the region of interest as shown in Figure 36a. Two repelling dipoles can push the blades far away from each other and require a large magnetic flux density ($\boldsymbol{B}$) to close them fully. Two attracting dipoles can pull the blades closed by overcoming the restoring force of the spring without an external magnetic field being applied leaving no means to open them. Thus, we will seek the placement of magnets which results in zero net interaction (counting the magnetic attraction force and interaction torque) between the two magnets. We will assume $\boldsymbol{m_1}$ is fixed as shown in Figure 36a and vary the position of $\boldsymbol{m_2}$ in this design optimization.

The magnetic dipole interaction force between $\boldsymbol{m_1}$ and $\boldsymbol{m_2}$ is given by

$$\boldsymbol{F_{1,2}} = \frac{3\mu_0}{4\pi r^5}[(\boldsymbol{m_1}\cdot\boldsymbol{r})\boldsymbol{m_2} + (\boldsymbol{m_2}\cdot\boldsymbol{r})\boldsymbol{m_1} + (\boldsymbol{m_1}\cdot\boldsymbol{m_2})\boldsymbol{r} - \frac{5(\boldsymbol{m_1}\cdot\boldsymbol{r})(\boldsymbol{m_2}\cdot\boldsymbol{r})}{r^2}\boldsymbol{r}], \qquad (4.3)$$

where $\boldsymbol{r}$ is the vector from $\boldsymbol{m_1}$ to $\boldsymbol{m_2}$. The resulting torque from this interaction force on the pivot point is shown in Eq. 4.4 and Eq. 4.5 for $\boldsymbol{m_1}$ and $\boldsymbol{m_2}$ respectively where $\boldsymbol{R_1}$ to $\boldsymbol{R_2}$ are the vectors connecting the pivot point to $\boldsymbol{m_1}$ and $\boldsymbol{m_2}$ as

$$\boldsymbol{\tau_{f1}} = \boldsymbol{R_1} \times \boldsymbol{F_{1,2}} \text{ and} \tag{4.4}$$

$$\boldsymbol{\tau_{f2}} = \boldsymbol{R_2} \times \boldsymbol{F_{1,2}}. \tag{4.5}$$

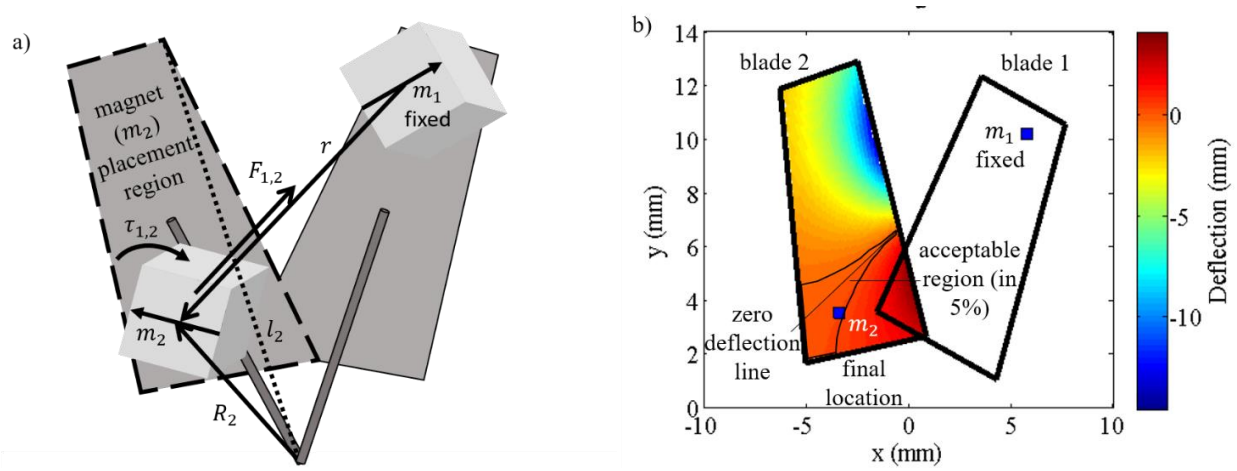

Figure 36: Scissor magnetic design optimization schematic. a) The top view of the scissors shows the magnetic interaction forces and torques. The placement of the magnet ($\boldsymbol{m_1}$) is fixed while a region of interest (dashed black line) is shown for the placement of the magnet ($\boldsymbol{m_2}$). b) The optimal region (< 5% error) for the placement of the magnet ($\boldsymbol{m_2}$) on the blade is outlined in black. Also, shown in blue is the actual location where it is mounted which falls inside the region and line of zero deflection. © 2019 IEEE

The resulting magnetic interaction torque generated by dipole 1 on dipole 2 is given by

$$\boldsymbol{\tau_{1,2}} = \frac{\mu_0}{4\pi r^5}[3\boldsymbol{m_2} \times (\boldsymbol{m_1} \cdot \boldsymbol{r})\boldsymbol{r} - r^2(\boldsymbol{m_2} \times \boldsymbol{m_1})]. \tag{4.6}$$

There is also a magnetic interaction torque generated by dipole 2 on dipole 1 ($\boldsymbol{\tau_{2,1}}$) which is not shown here for brevity but has an analogous formulation. The magnetic interaction torque ($\boldsymbol{\tau_{1,2}}$), the resultant torque from the magnetic interaction force ($\boldsymbol{\tau_{f2}}$) and the elastic torque of spring element ($k\boldsymbol{p_{i,2}}$) are in equilibrium as

$$\boldsymbol{\tau_{f2}} + \boldsymbol{\tau_{1,2}} - k\boldsymbol{p_{i,2}} = 0. \tag{4.7}$$

Here, k is a spring constant that captures the elastic modulus (E), second moment of inertia (I) and length of the spring (L). This calculated deflection is only for the nitinol wire which has a length of 2.6 mm as seen in

$$\boldsymbol{p_{i,2}} = (\boldsymbol{\tau_{f2}} + \boldsymbol{\tau_{1,2}})\frac{L^2}{2EI}. \tag{4.8}$$

Therefore, this deflection can be extended to the full blade using a similar triangles approach as seen in Eq. 4.9 where l_2 is the length from the pivot to the tip of blade 2. To seek the optimal placement of $\boldsymbol{m_2}$, we consider any point that results in a nominal blade tip deflection below 5% error (or 5% deflection of the total tip to tip separation) as acceptable for the placement of the magnet ($\boldsymbol{m_2}$) as shown in Eq. 4.10. A 5% error translates to a deflection of approximately $\pm$380 μm.

$$\frac{\boldsymbol{p_{f,2}}}{L} = \frac{\boldsymbol{D_2}}{l_2} \tag{4.9}$$

$$\boldsymbol{D_{i2}} < |0.38| \text{ mm} \tag{4.10}$$

Figure 36b shows the region where the magnet $\boldsymbol{m_2}$ can be placed to minimize the magnetic interaction force and torque. While the whole region shown in Figure 36a or blade was explored, only the small band outlined in Figure 36b produces a deflection of less than 5% (380 μm) of the tip to tip separation of the blades in the resting position. The line of zero nominal blade tip deflection of the blade is also shown. This is the ideal location for the magnet, but because the magnet is glued manually using tweezers, it cannot always be placed accurately on the line. The figure also shows the actual location where the magnet $\boldsymbol{m_2}$ is placed which results in a blade nominal tip deflection of only 290 μm and β_2 of 10°. This is deemed close enough to the optimal location.

Once the location of the second magnet ($\boldsymbol{m_2}$) is finalized, the entire scissors is assembled. We now extend the model to include the actuating torque ($\boldsymbol{\tau_{m2}}$) due to an externally applied magnetic flux density ($\boldsymbol{B}$) during actuation as given by

$$\boldsymbol{\tau_{m2}} = \boldsymbol{m_2} \times \boldsymbol{B}. \tag{4.11}$$

Again, the equation is only shown for $\boldsymbol{m_2}$, but an analogous formulation exists for the magnet $\boldsymbol{m_1}$ which is used to calculate the deflection of blade 1. The deflection of each blade $\boldsymbol{p_{f,1}}$ and $\boldsymbol{p_{f,2}}$ is calculated as

$$\boldsymbol{p_{f,1}} = (\boldsymbol{\tau_{f1}} + \boldsymbol{\tau_{2,1}} + \boldsymbol{\tau_{m1}}) \frac{L^2}{2EI} \text{ and} \tag{4.12}$$

$$\boldsymbol{p_{f,2}} = (\boldsymbol{\tau_{f2}} + \boldsymbol{\tau_{1,2}} + \boldsymbol{\tau_{m2}}) \frac{L^2}{2EI}. \tag{4.13}$$

Similar to the previous section, this calculated deflection is only for the nitinol wire which has a length of 2.6 mm. Therefore, this deflection is similarly extended to the full blade using a similar triangles approach as seen in Eq. 4.9 where l_1 and l_2 are the distances from the pivot point to the tip of blade 1 and blade 2 respectively. The model iteratively updates the position of the magnets $\boldsymbol{m_1}$ and $\boldsymbol{m_2}$ based on the previous deflection of the blades. This updated position is used to calculate updated torques until a converged solution is reached. The resulting deflections $\boldsymbol{D_{f1}}$ (for blade 1) and $\boldsymbol{D_{f2}}$ are subtracted from the initial position of the blade separation to obtain the tip to tip separation ($\boldsymbol{d}$) of the blades from 0 – 14 mT as shown in Figure 37a and Eq. 4.14.

$$\boldsymbol{d}(\boldsymbol{B}) = d(0) \; - \boldsymbol{D_1} - \boldsymbol{D_2} \tag{4.14}$$

4.5 Results

4.5.1 Model Validation

The tip to tip separation of the blades ($\boldsymbol{d}$) under varying applied field is plotted in Figure 37b. The experimental data is based on 4 experimental measurements taken at different field strengths, while the model is from Eq. 4.14. A large deviation is seen for the last few data points ranging from 9 mT to 14 mT, which we attribute to two primary reasons. The first and most apparent one is that there is friction present in the scissors that is not captured by the model. The second reason is that it is possible that the nitinol enters a nonlinear deformation regime at high strains.

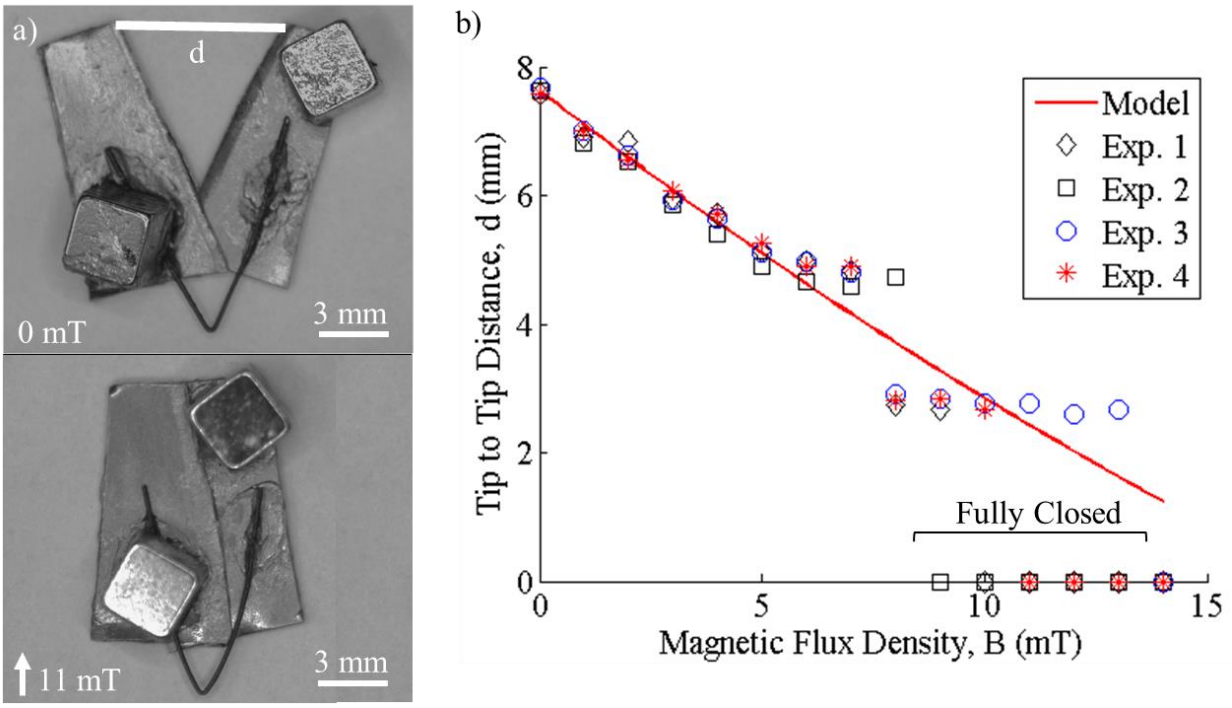

Figure 37: a) The tip to tip distance (d) between the blades is shown at 0 mT and 11 mT. b) The measured and modelled tip to tip distance as a function of magnetic flux density (B) for a set of unloaded scissors is plotted. © 2019 IEEE

4.5.2 Force Measurements

The blocking force of the scissors was measured using a single-axis 100 g load cell (GSO100, Transducer Technologies), which has a rated accuracy of $\pm$0.8 mN. The measurement is shown in Figure 38. In this measurement, one blade of the scissors is pushed into contact with the load cell measuring rod but does not move during the measurement. The other blade of the scissors is glued to the platform and not able to move. One important thing to note here is that the magnet $\boldsymbol{m_1}$ has been removed from the scissors for the purposes of this experiment. This is to remove any magnetic interaction with the load cell, but it is possible that this removal may have a small impact on the force output. However, the scissors were optimized to minimize the magnetic interaction forces and torques while in resting position, so we expect this error to be small.

The resultant forces vs. magnetic flux density are plotted in Figure 38. A maximum force of 75 mN is achieved at an applied flux density of 20 mT, which is the largest magnetic flux density output by the coils. If the scissors fully close at 9 mT, 35 mN can be used for cutting.

However, if the scissors close at 14 mT, only 16 mN of the force is used for cutting. Since it is not possible to separate the closing and cutting motions of the scissors, we can conclude that the cutting force falls between the 16 mN to 35 mN range.

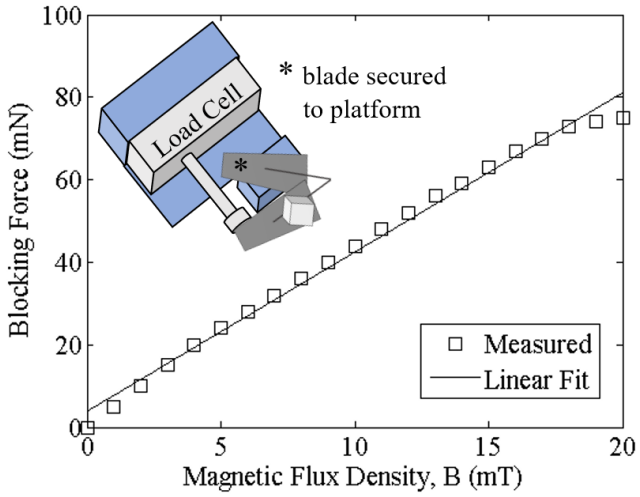

Figure 38: The blocking force of the scissors is measured to get an estimate of the force required for cutting agar using the image shown in the inset. This setup is placed inside the 3-axis coils. © 2019 IEEE

4.5.3 Robotic Motion and Cutting Demonstration of Agar

A demonstration of cutting agarose gel is shown in Figure 39. The scissors are placed inside a 32 x 29 x 21 mm box along with a small strip of agar dyed red. The bottom of the box is also lined with agar dyed red. An acrylic plate with a hole is placed on top of this lining. The agar strip is fed up from the hole to ensure that it stays vertical. The box is filled with 1 cSt silicone oil and all experiments are performed in this liquid.

The scissors are maneuvered from their initial position using stick slip motion to the target location where an agar tower is sliced using a field strength of 20 mT. The scissors are then maneuvered back to their initial position. Five screenshots from the video are shown in Figure 39 where the scissors are shown: a) at their initial position, b) before cutting, c) during cutting, d) immediately after cutting, e) home position.

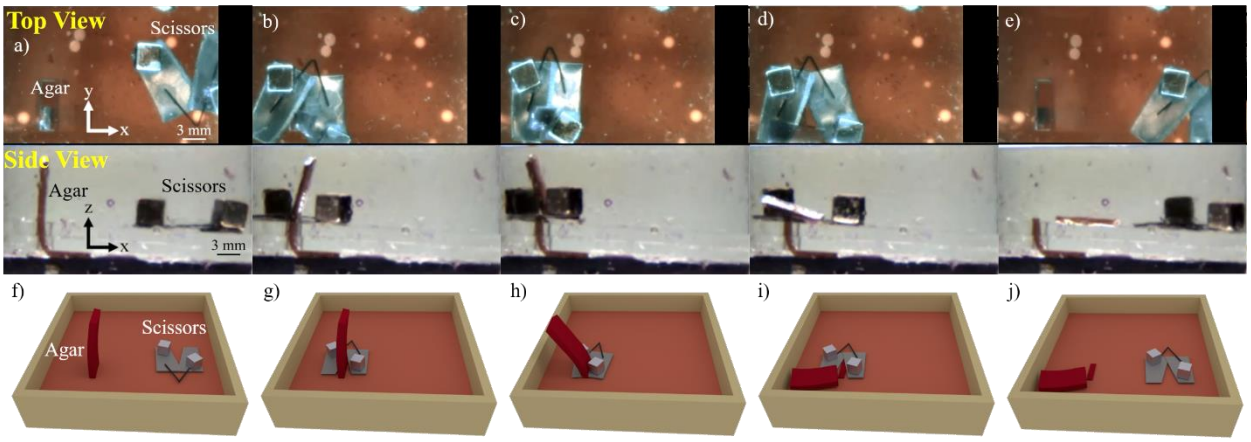

Figure 39: a)-e) The scissors are shown moving from their initial position to the agar and cutting it and then moving back. Both the top and side camera views are shown. f)-j) A simulation of the scissors moving from their initial location to the agar and cutting it and then moving back is shown. The simulation matches the snapshots of the video. © 2019 IEEE

4.5.4 Cutting Demonstration of Tissue inside Mock Surgical Setting

4.5.4.1 Design Updates

The design of the scissors was updated to scale them down while maintaining the same magnetic volume so that the cutting force does not decrease. The scissors were scale down to be 6 mm wide when they are fully closed. The titanium sheets were cut into smaller blades and assembled in the same method as shown in Figure 34. A 3D printed mold was used to ensure that the blades and nitinol wire stay in the desired orientation. A row of 5 NdFeB magnets that were 2 mm cubes were added onto each blade resulting in a total magnetic volume of 40 mm^3 which is higher than the original 27 mm^3 cubed magnetic volume. However, the placement of the magnets resulted in a larger angle from the perpendicular axis (>15°) and thus the same magnetic volume is pointing perpendicular to the net magnetization direction for each blade. The new design is shown in Figure 40.

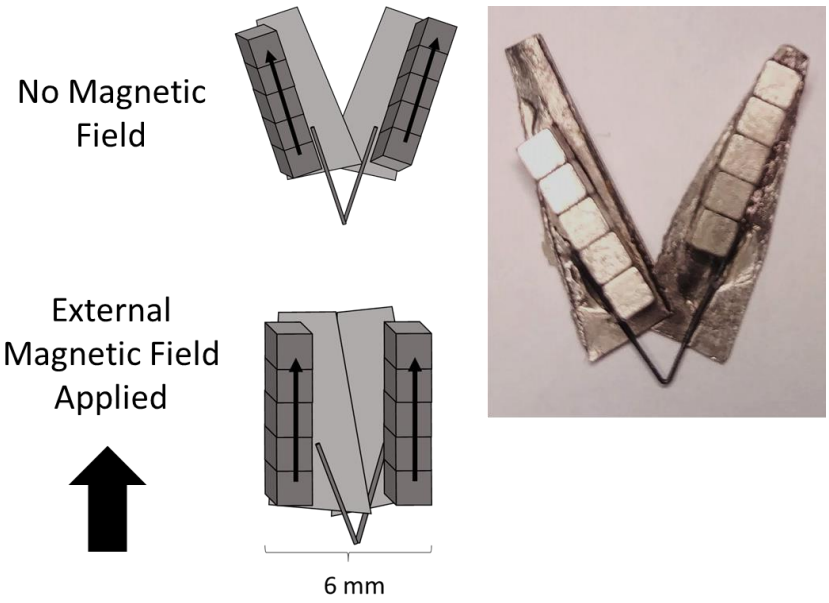

Figure 40: The updated design of the scissors is shown. This pair of scissors has been scaled down, but a row of magnets was added to maintain net magnetic volume that generates torque.

4.5.4.2 Updated Experimental Setup

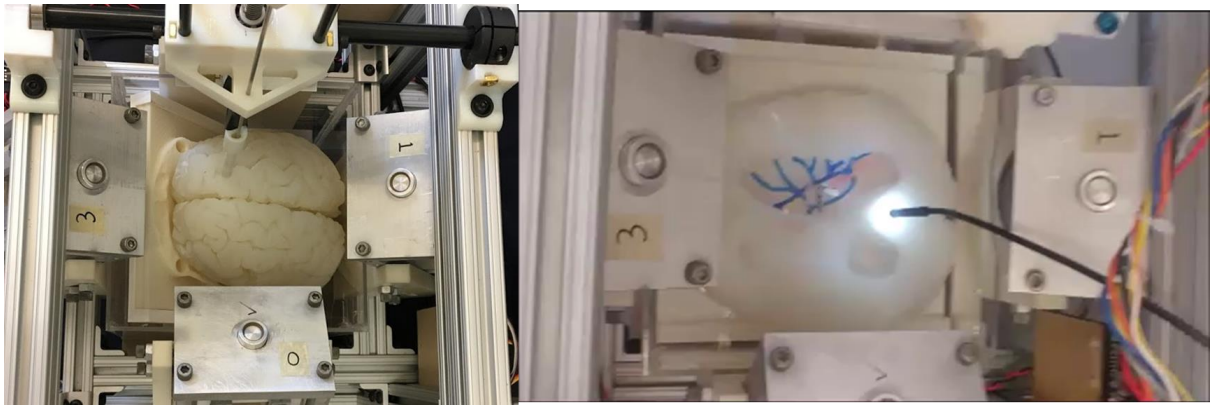

Figure 41: Experimental setup with 4 rotating permanent magnets with a brain phantom and endoscope in the center lighting the workspace.

A new magnetic actuation platform was proposed for experiments inside a brain phantom. The magnetic actuation platform consists of four permanent magnets arranged around a large 6 cm cubed workspace so that a full brain can fit inside to create a mock surgical setting. The permanent magnets rotate about their axis using DC motors. This can create the desired magnetic

field and gradients in order to get the desired force and torque outputs on the mobile devices placed inside the workspace. Again, the scissors are actuated using only magnetic torques. A small piglet brain was placed in the center of the workspace and was floated inside a contained filled with water. Open loop control was used again with a joystick in order to navigate the scissors by controlling the magnetic fields. This causes the magnets to rotate on their axes. Figure 42 shows a depiction of the magnetic actuation platform used for this set of experiments. A phantom brain made from silicone is shown in this figure but brain tissue from a piglet is used during the experiments. However, this setup was unsuccessful in controlling the scissors due to the large gradients that exist inside the workspace. These gradients meant that the scissors could not be moved along a desired trajectory.

A different approach was taken in order to obtain the results below where a single 1 inch cube magnet is used to pull the scissors inside a brain phantom and to cut through the brain tissue of a goat. A model of the brain ventricles was obtained online form an open source software. This was 3D printed using a Form Labs printer and then used to make a negative mold of the brain ventricles with agar. The scissors were placed inside the agar mold along with a piece of brain tissue from a goat that was clamped and an endoscope.

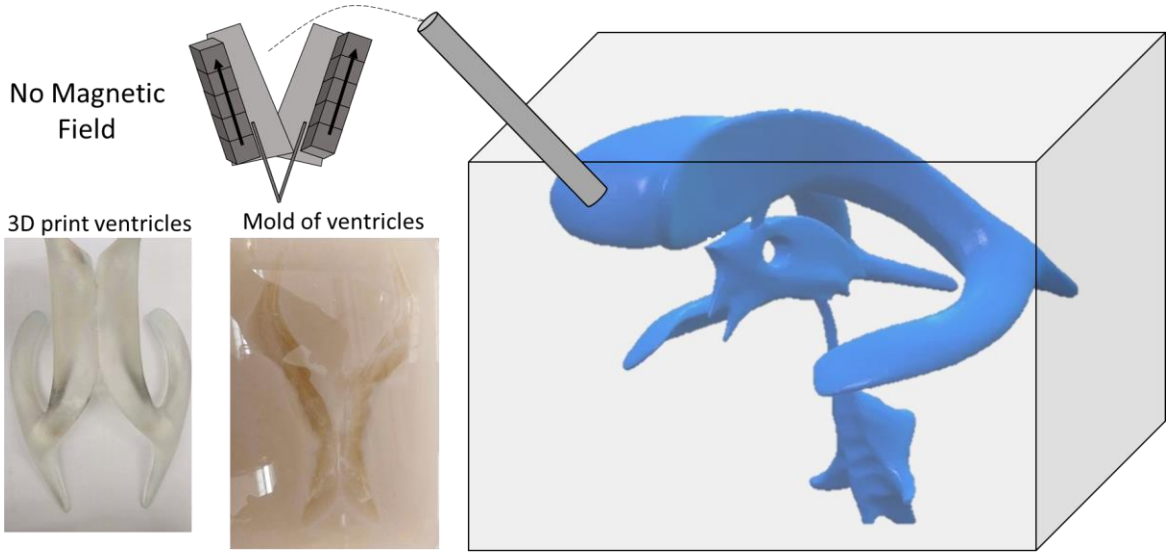

Figure 42: Brain ventricles were 3D printed and used to make an agar mold. The scissors along with a piece of goat brain tissue and an endoscope were placed inside the agar mold.

4.5.4.3 Results

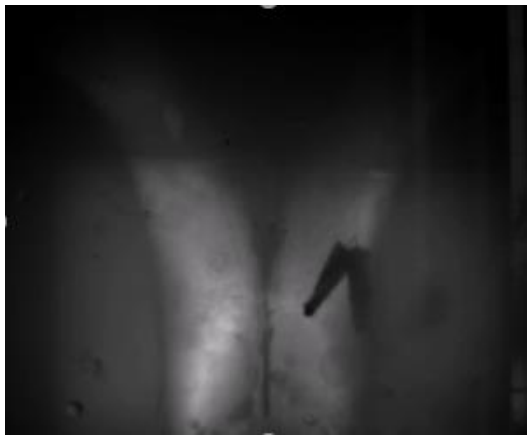

Figure 43: The scissors inside the lateral ventricles of the brain are moved using an external field applied via a 1-inch cube permanent magnet.

A pair of scissors is used to cut brain tissue obtained from a goat inside the agar mold of the brain ventricles. The brain tissue is clamped inside the mold which accomplishes two major goals: 1) it provide a piece of protruding tissue for the scissors to cut and 2) pulling on the tissue increases the tension on it and often when tissues are in tension, they require a smaller cutting force. This makes is easier to cut through the tissue. The scissors are navigated to the target site using a 1-inch cube magnet as shown in Figure 43 and the tissue cutting is shown in Figure 44 along with an endoscopic image inset.

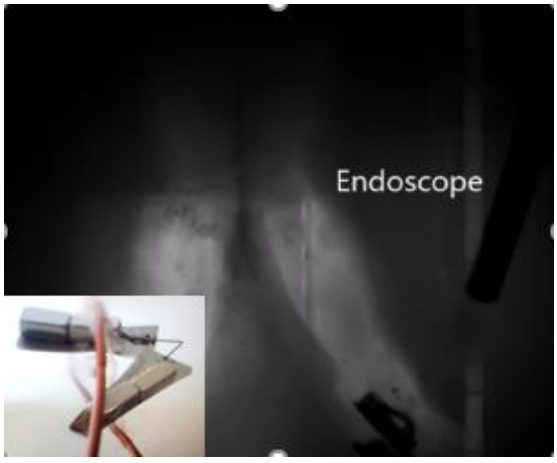

Figure 44: The brain tissue of a goat is clamped inside the agar mold while the pair of scissors is used to cut the protruding tissue. The inset shows the image taken from the endoscope.

After the desired surgical process has been completed, the scissors will need to be retrieved from the target location. The two main ways of achieving this are 1) putting a string on the scissors or 2) using magnetic fields to navigate it back to the entry site where the trocar is located. Putting a string on the pair of scissors is not the same as a tether even though it essentially means the scissors are attached to something. This is because a string is able to navigate around corners and follow the scissors on any desired trajectory unlike a traditional tether. For retrieval purposes, the string can be pulled back and the scissors will slowly retract to the trocar. The scissors can similarly be navigated back to the trocar using the same magnetic fields that were used to navigate them to the target location. The string, however, is considered to be more secure by surgeons as it can always be used to retract the scissors in the case of an emergency or the scissors getting stuck in any location. The string provides a level of comfort and security both to the surgeons and the patients.

4.6 Conclusions

The pair of scissors proposed in this study are 15 mm x 15 mm when fully open and 11 mm wide when fully closed. This is approximately two times the desired size for clinical use. Typically, neurosurgeons use small surgical corridors via burr holes through which instruments are fed through and the scissors would have to fit through this corridor. Therefore, for the next study, the scissors are scaled down to a width of 6 mm when closed and a row of permanent magnets is used to maintain the same magnetic volume. A larger external magnetic flux density can also be used to generate the same force output.

The rat liver required approximately 1.6 N to cut with a pair of scissors and sheep liver approximately 7.1 N [75]. The cutting force achieved here is between 16-35 mN. This force can be done by using larger external magnetic flux densities. Recent advances in clinical-scale coil systems have shown capabilities to produce fields up to 400 mT [13] which is 20 times larger than the maximum field strength used in this study. Using such a large field, the force output of the scissors would be increased to 1.5 N which is close to the value required for rat liver. In future work we will investigate cutting forces at higher field strength, which would also allow for further reduction of the size of the surgical scissors from what has been achieved. Further work is needed to achieve smooth cutting motion for dexterous procedures as friction effects are seen

here which cause the scissors to stick during the closing and can reduce the cutting force produced.

The scissors motion and cutting demonstration here was a relatively simple motion in a 2D plane for both cutting of agar and brain tissue. Future work will develop a robust 3D controller for accurate feedback-controlled positioning and cutting in arbitrary environments. Future studies will explore the cutting of different tissues, explore smaller scissors, control the 3D positioning and the use of medical imaging as real-time feedback to further prove the potential of using untethered surgical tools. The safety and usability of completely untethered tools is a potential concern depending on the application scenario. One way this concern could be addressed is by adding an extremely flexible cable such as a string to the scissors for scissor removal.

Chapter 5
Contributions and Future Research

This chapter summarizes the contributions of this thesis for on-chip and mobile devices. It also outlines how this thesis advances the field of small-scale robotics as well as pointing out future research directions.

5 Contributions and Future Research

5.1 Contributions

This thesis explores the role of two specific types of devices: 1) on-chip tools and 2) untethered mobile tools. Both sets of tools are actuated remotely using magnetic fields. The on-chip devices are proposed for use in cell manipulation while the untethered mobile tools are proposed for use in neurosurgery.

The on-chip tools are simple devices made up of a combination of magnetic material and polymer base. They are added onto a microfluidic platform with a complex infrastructure to fulfill desired tasks such as 1) cell sorting and 2) cell stimulation. While the magnetic valve and magnetic oscillating beam used in these two cases are independently similar; their addition to individualized platforms results in new capabilities.

For each case, a device was designed to take advantage of the magneto-elastic nature of the valve and beam. The devices were studied using physics-based models stemming from electricity and magnetism, elasticity and fluid mechanics. Both devices were also studied using 3D finite element numerical simulations performed in ANSYS using Workbench. Fluid-structure interaction simulations were used to study the vortices that were generated and how particle trajectories were affected in the case of cell sorting. These simulated results were then matched to experimental results. This allows a platform for exploring optimizations to device designs and how changes to different parameters (magnetic, elastic or fluid based) can alter the trajectory of the particles. Fluid-structure interaction simulations were also used to determine the shear stress generated on the cell surface for the purposes of cell stimulation. This was something that could not be done experimentally and thus simulations were essential to identifying parameters such as device deflection and gap height that would generate the desired shear stress and thus stimulate the cells.

A new magnetic actuation system was designed and built for each of these applications. The magnetic actuation systems consisted of two electromagnets that were placed in a 1D Helmholtz coil configuration. For the purposes of cell sorting, the coil system was necessary to achieve high speed cell sorting. This means that the designed coil system had low inductance so that a high frequency signal could be used for cell sorting. The coil system designed for this experiment

could be reliably operated up to a frequency of 1 kHz with negligible amplitude loss. The coil system also had to be able to generate a magnetic flux density of 10 mT to consistently actuate the valve and required a uniform magnetic field in a workspace large enough to fit a microfluidic chip. The magnetic actuation platform designed for the purposes of cell stimulation did not have any requirements for high frequency as it was actuated only at a frequency of 1 Hz. The main requirements for this platform were: 1) magnetic flux density of 10 mT to actuate the beam, 2) fit around a confocal microscope necessary for imaging and 3) reduced heat generation from the electromagnets for longer operation time (10 minutes). The heat generation was minimized by doubling the resistance of the wires typically used in the coils by double wrapping the wire. Each of these magnetic actuation platforms were used in conjunction with the on-chip devices to achieve the desired goals. Both on-chip devices were fully controlled using a global magnetic field.

The mobile untethered device was the first ever pair of small-scale surgical scissors designed that are fully controllable using global magnetic fields for removal of pineal tumours or cysts during neurosurgery. The scissors were completely manufactured in house using thin titanium sheets that were grinded to produce sharp edges. The scissors were then assembled with a super-elastic nitinol wire and magnets. The nitinol wire adds an elastic element to the device which allows the scissors to be opened and closed using one control input as they spring back to resting position when the magnetic field is removed. The magnets are arranged to provide a net magnetization direction to the device in order to orient and actuate it. The placement of the magnets was optimized using a physics-based model composed of dipole interaction forces and torques and elastic torque from the spring element. This model was also expanded to predict the tip-to-tip separation between the blades when an external magnetic field was applied. The scissors were also assembled using a unique sandwich design in order to maintain contact between the blades without a pin joint. This allows the blades to shear the tissue as seen with a typical pair of scissors. Experiments were then performed with the scissors to show cutting of agar and brain tissue. The blocking force of the scissors was also measured using a single axis force sensor.

The scissors were actuated using two different existing magnetic actuation platforms. The first was a 3D Helmholtz coil system in which the scissors were actuated on a 2D acrylic base in a fluid filled environment. This demonstration was completed using only magnetic torque where the scissors were first oriented in the direction of the external magnetic field and then actuated to

a target location using stick-slip motion where they were closed to cut agar. All of this was done open loop using a joystick with a top view and side view camera. The scissors were also actuated to cut brain tissue inside a magnetic actuation platform consisting of four permanent magnets. This actuation platform was used because it has a large workspace that allows a whole brain to be placed inside. However, gradient meant that this system was not sufficiently capable of controlling the scissors, so a 1-inch cube magnet was used instead. The brain tissue of a goat was clamped inside an agar mold of the brain ventricles and the scissors were then used to cut it. Again, magnetic torque was employed to cut the tissue but gradient pulling was used to move the scissors to the target location.

The major results of this thesis were all performed using different devices and different actuation platforms. Cell sorting was performed using a small 1D Helmholtz coil configuration with low inductance. Cell stimulation was performed using a large 1D Helmholtz coil configuration with a lower resistance. Cutting of agar was performed using a 3D Helmholtz coil configuration while cutting of brain tissue was performed using a permanent magnet. This shows the unique capabilities of the devices presented which can be controlled in various global magnetic fields as well as the ability to use different actuation setups to achieve the desired results.

5.2 Future Research Directions

Small-scale robotics is an exciting area of research with potential applications in many different fields. Several biomedical applications were explored in this thesis using various devices and platforms. Specific research directions for each of the projects are discussed below.

Microfluidic platforms have allowed for an expansion of research into disease by isolating cells or cell populations. This allows for a targeted study on cells and how different factors can affect their growth and the impacts on human health. For this reason, non-contact cell manipulation has been a growing field of research. In addition to the cell sorting and cell stimulation projects mentioned in this thesis, vibrating cells as a potential treatment for cancer is also being explored by using a magnetically vibrating platform. Specific future directions related to the cell sorting and cell stimulation projects are discussed below.

Cell sorting:

1. Parametric study using 3D finite element analysis for design optimization of the microfluidic device geometry which can also help to increase the speed and efficiency of sorting.

2. Using electronics that can be operated at higher frequencies to increase the speed of the valve. Currently, increases in frequency above 1 kHz result in a drastic amplitude reduction since the current setup behaves like a low pass filter. While the frequency can technically be increased to 3.3 kHz, the amplitude of the magnetic field is not sufficient to actuate the valve.

3. Parallel sorting of cells using multiple valves at once that can be independently actuated in a global magnetic field. Current research has only shown the ability to control two valves at once by magnetizing them perpendicular to each other in order to independently control them. However, for this device to be commercially feasible, multiple valves would need to be actuated both independently and simultaneously which has not yet been shown.

4. This project was a collaboration with Bio-Rad Laboratories, a life sciences company. They currently have a detection system for cells that can be added to our device in order to successfully sort cells. Current research has only shown successful sorting of microbeads.

Cell Stimulation:

1. Develop an experimental technique to measure the gap height on each device to make cell stimulation more reliable and reproducible and thus obtain a threshold value of the shear stress from numerical simulations by accurately matching them to the experimental cases.

2. Install the magnetically actuated oscillating beam inside a microfluidic device in order to study more specific cell characteristic and signalling pathways. This will allow the study to go beyond just calcium signalling.

Minimally invasive surgery is a rapidly growing research area because it has so many benefits from reducing trauma and recovery times as well as the associated medical costs. The development of the first completely untethered surgical scissors is a step forward, but many steps remain before these scissors can be utilized in surgical setting. Outlined below are some currently being pursued.

1. Scale down the scissors further to better fit inside small surgical corridors used for neurosurgery and make the scissors biocompatible for surgical operations (for example: by using gold coated magnets and biocompatible glue).

2. Explore design optimizations that will allow the scissors to have a larger output cutting force to cut various tissues and harder materials.

3. Force and contact sensors can be placed on the device in addition to visual feedback while navigating through the ventricles in order to have a more efficient path to a target site and avoid collisions or tissue damage. This will also allow for the development of autonomous controllers.

4. An untethered magnetically actuated pair of forceps can be developed to allow the whole surgery to be done wirelessly.

References

[1] E. Diller and M. Sitti, "Micro-Scale Mobile Robotics," *Foundations and Trends® in Robotics,* vol. 2, no. 3, pp. 143-259, 2013.

[2] T. Xu, J. Zhang, M. Salehizadeh, O. Onaizah, and E. Diller, "Millimeter-scale flexible robots with programmable three-dimensional magnetization and motions," *Science Robotics,* vol. 4, no. 29, p. eaav4494, 2019.

[3] O. Youssefi and E. Diller, "Contactless Robotic Micromanipulation in Air Using a Magneto-Acoustic System," *IEEE Robotics and Automation Letters,* vol. 4, no. 2, pp. 1580-1586, 2019.

[4] Z. Li and E. Diller, "Polymer filament–based in situ microrobot fabrication using magnetic guidance," *International Journal of Advanced Robotic Systems,* vol. 14, no. 1, p. 1729881416682707, 2016.

[5] E. Diller, J. Giltinan, and M. Sitti, "Independent control of multiple magnetic microrobots in three dimensions," *The International Journal of Robotics Research,* vol. 32, no. 5, pp. 614-631, 2013.

[6] M. P. Kummer, J. J. Abbott, B. E. Kratochvil, R. Borer, A. Sengul, and B. J. Nelson, "OctoMag: An Electromagnetic System for 5-DOF Wireless Micromanipulation," *IEEE Transactions on Robotics,* vol. 26, no. 6, pp. 1006-1017, 2010.

[7] J. J. Abbott, E. Diller, and A. J. Petruska, "Magnetic Methods in Robotics," *Annual Review of Control, Robotics, and Autonomous Systems,* 2019.

[8] D. W. McRobbie, "Occupational exposure in MRI," *Br J Radiol,* vol. 85, no. 1012, pp. 293-312, 2012.

[9] M. Salehizadeh and E. Diller, "Two-agent formation control of magnetic microrobots," in *2016 International Conference on Manipulation, Automation and Robotics at Small Scales (MARSS)*, 2016, pp. 1-6.

[10] E. Diller, S. Floyd, C. Pawashe, and M. Sitti, "Control of Multiple Heterogeneous Magnetic Microrobots in Two Dimensions on Nonspecialized Surfaces," *IEEE Transactions on Robotics,* vol. 28, no. 1, pp. 172-182, 2012.

[11] S. Martel and M. Mohammadi, "Using a swarm of self-propelled natural microrobots in the form of flagellated bacteria to perform complex micro-assembly tasks," in *2010 IEEE International Conference on Robotics and Automation*, 2010, pp. 500-505.

[12] S. Chowdhury, W. Jing, and D. J. Cappelleri, "Towards Independent Control of Multiple Magnetic Mobile Microrobots," *Micromachines (Basel),* vol. 7, no. 1, 2015.

[13] J. Rahmer, C. Stehning, and B. Gleich, "Remote magnetic actuation using a clinical scale system," *PLOS ONE,* vol. 13, no. 3, p. e0193546, 2018.

[14] P. Ryan and E. Diller, "Magnetic Actuation for Full Dexterity Microrobotic Control Using Rotating Permanent Magnets," *IEEE Transactions on Robotics,* vol. 33, no. 6, pp. 1398-1409, 2017.

[15] J. Zhang and E. Diller, "Millimeter-scale magnetic swimmers using elastomeric undulations," in *2015 IEEE/RSJ International Conference on Intelligent Robots and Systems (IROS)*, 2015, pp. 1706-1711.

[16] Z. Jiachen, O. Onaizah, K. Middleton, L. You, and E. Diller, "Reliable Grasping of Three-Dimensional Untethered Mobile Magnetic Microgripper for Autonomous Pick-and-Place," *IEEE Robotics and Automation Letters,* vol. 2, no. 2, pp. 835-840, 2017.

[17] J. Zhang, O. Onaizah, A. Sadri, and E. Diller, "A generic label-free microfluidic microobject sorter using a magnetic elastic diverter," *Biomedical Microdevices,* vol. 19, no. 2, p. 43, 2017.

[18] A. J. Armstrong, M. S. Marengo, S. Oltean, G. Kemeny, R. L. Bitting, J. D. Turnbull, *et al.*, "Circulating tumor cells from patients with advanced prostate and breast cancer display both epithelial and mesenchymal markers," *Mol Cancer Res,* vol. 9, no. 8, pp. 997-1007, 2011.

[19] F. Z. Bischoff, D. A. Marquez-Do, D. I. Martinez, D. Dang, C. Horne, D. Lewis, *et al.*, "Intact fetal cell isolation from maternal blood: improved isolation using a simple whole blood progenitor cell enrichment approach (RosetteSep)," *Clin Genet,* vol. 63, no. 6, pp. 483-9, 2003.

[20] M. J. Tomlinson, S. Tomlinson, X. B. Yang, and J. Kirkham, "Cell separation: Terminology and practical considerations," *J Tissue Eng,* vol. 4, p. 2041731412472690, 2013.

[21] A. W. Wognum, A. C. Eaves, and T. E. Thomas, "Identification and isolation of hematopoietic stem cells," *Arch Med Res,* vol. 34, no. 6, pp. 461-75, 2003.

[22] C. W. t. Shields, C. D. Reyes, and G. P. Lopez, "Microfluidic cell sorting: a review of the advances in the separation of cells from debulking to rare cell isolation," *Lab Chip,* vol. 15, no. 5, pp. 1230-49, 2015.

[23] J. Voldman, "Electrical forces for microscale cell manipulation," *Annu Rev Biomed Eng,* vol. 8, pp. 425-54, 2006.

[24] X. Wang, S. Chen, M. Kong, Z. Wang, K. D. Costa, R. A. Li, *et al.*, "Enhanced cell sorting and manipulation with combined optical tweezer and microfluidic chip technologies," *Lab Chip,* vol. 11, no. 21, pp. 3656-62, 2011.

[25] K. Hoshino, Y. Y. Huang, N. Lane, M. Huebschman, J. W. Uhr, E. P. Frenkel, *et al.*, "Microchip-based immunomagnetic detection of circulating tumor cells," *Lab Chip,* vol. 11, no. 20, pp. 3449-57, 2011.

[26] Y. Yamanishi, S. Sakuma, K. Onda, and F. Arai, "Powerful actuation of magnetized microtools by focused magnetic field for particle sorting in a chip," *Biomed Microdevices,* vol. 12, no. 4, pp. 745-52, 2010.

[27] M. Hagiwara, T. Kawahara, T. Iijima, and F. Arai, "High-Speed Magnetic Microrobot Actuation in a Microfluidic Chip by a Fine V-Groove Surface," *IEEE Transactions on Robotics,* vol. 29, no. 2, pp. 363-372, 2013.

[28] P. B. Howell Jr, J. P. Golden, L. R. Hilliard, J. S. Erickson, D. R. Mott, and F. S. Ligler, "Two simple and rugged designs for creating microfluidic sheath flow," *Lab on a Chip,* vol. 8, no. 7, pp. 1097-1103, 2008.

[29] T. Betancourt and L. Brannon-Peppas, "Micro- and nanofabrication methods in nanotechnological medical and pharmaceutical devices," *Int J Nanomedicine,* vol. 1, no. 4, pp. 483-95, 2006.

[30] C. Uhler and G. V. Shivashankar, "Regulation of genome organization and gene expression by nuclear mechanotransduction," *Nat Rev Mol Cell Biol,* vol. 18, no. 12, pp. 717-727, 2017.

[31] S. Dupont, L. Morsut, M. Aragona, E. Enzo, S. Giulitti, M. Cordenonsi, *et al.*, "Role of YAP/TAZ in mechanotransduction," *Nature,* vol. 474, no. 7350, pp. 179-83, 2011.

[32] H. Hemmatian, A. D. Bakker, J. Klein-Nulend, and G. H. van Lenthe, "Aging, Osteocytes, and Mechanotransduction," *Curr Osteoporos Rep,* vol. 15, no. 5, pp. 401-411, 2017.

[33] L. You, S. Temiyasathit, P. Lee, C. H. Kim, P. Tummala, W. Yao, *et al.*, "Osteocytes as mechanosensors in the inhibition of bone resorption due to mechanical loading," *Bone,* vol. 42, no. 1, pp. 172-9, 2008.

[34] J. C. Crockett, M. J. Rogers, F. P. Coxon, L. J. Hocking, and M. H. Helfrich, "Bone remodelling at a glance," *J Cell Sci,* vol. 124, no. Pt 7, pp. 991-8, 2011.

[35] J. Li, E. Rose, D. Frances, Y. Sun, and L. You, "Effect of oscillating fluid flow stimulation on osteocyte mRNA expression," *J Biomech,* vol. 45, no. 2, pp. 247-51, 2012.

[36] F. Meng, G. F. Murray, L. Kurgan, and H. J. Donahue, "Functional and structural characterization of osteocytic MLO-Y4 cell proteins encoded by genes differentially expressed in response to mechanical signals in vitro," *Sci Rep,* vol. 8, no. 1, p. 6716, 2018.

[37] C. Wittkowske, G. C. Reilly, D. Lacroix, and C. M. Perrault, "In Vitro Bone Cell Models: Impact of Fluid Shear Stress on Bone Formation," *Front Bioeng Biotechnol,* vol. 4, p. 87, 2016.

[38] S. Weinbaum, S. C. Cowin, and Y. Zeng, "A model for the excitation of osteocytes by mechanical loading-induced bone fluid shear stresses," *J Biomech,* vol. 27, no. 3, pp. 339-60, 1994.

[39] M. L. Knothe Tate, R. Steck, M. R. Forwood, and P. Niederer, "In vivo demonstration of load-induced fluid flow in the rat tibia and its potential implications for processes associated with functional adaptation," *J Exp Biol,* vol. 203, no. Pt 18, pp. 2737-45, 2000.

[40] X. L. Lu, B. Huo, M. Park, and X. E. Guo, "Calcium response in osteocytic networks under steady and oscillatory fluid flow," *Bone,* vol. 51, no. 3, pp. 466-73, 2012.

[41] M. J. Mc Garrigle, C. A. Mullen, M. G. Haugh, M. C. Voisin, and L. M. McNamara, "Osteocyte differentiation and the formation of an interconnected cellular network in vitro," *Eur Cell Mater,* vol. 31, pp. 323-40, 2016.

[42] H. C. Blair, Q. C. Larrouture, Y. Li, H. Lin, D. Beer-Stoltz, L. Liu, *et al.*, "Osteoblast Differentiation and Bone Matrix Formation In Vivo and In Vitro," *Tissue Eng Part B Rev,* vol. 23, no. 3, pp. 268-280, 2017.

[43] K. J. Lewis, D. Frikha-Benayed, J. Louie, S. Stephen, D. C. Spray, M. M. Thi, *et al.*, "Osteocyte calcium signals encode strain magnitude and loading frequency in vivo," *Proc Natl Acad Sci U S A,* vol. 114, no. 44, pp. 11775-11780, 2017.

[44] M. Hu, G. W. Tian, D. E. Gibbons, J. Jiao, and Y. X. Qin, "Dynamic fluid flow induced mechanobiological modulation of in situ osteocyte calcium oscillations," *Arch Biochem Biophys,* vol. 579, pp. 55-61, 2015.

[45] I. Kalajzic, B. G. Matthews, E. Torreggiani, M. A. Harris, P. Divieti Pajevic, and S. E. Harris, "In vitro and in vivo approaches to study osteocyte biology," *Bone,* vol. 54, no. 2, pp. 296-306, 2013.

[46] X. E. Guo, E. Takai, X. Jiang, Q. Xu, G. M. Whitesides, J. T. Yardley, *et al.*, "Intracellular calcium waves in bone cell networks under single cell nanoindentation," *Mol Cell Biomech,* vol. 3, no. 3, pp. 95-107, 2006.

[47] A. E. Morrell, G. N. Brown, S. T. Robinson, R. L. Sattler, A. D. Baik, G. Zhen, *et al.*, "Mechanically induced Ca(2+) oscillations in osteocytes release extracellular vesicles and enhance bone formation," *Bone Res,* vol. 6, p. 6, 2018.

[48] M. Hagiwara, T. Kawahara, and F. Arai, "Local streamline generation by mechanical oscillation in a microfluidic chip for noncontact cell manipulations," *Applied Physics Letters,* vol. 101, no. 7, p. 074102, 2012.

[49] B. Lautrup, *Physics of continuous matter : exotic and everyday phenomena in the macroscopic world*. Bristol ; Philadelphia: Institute of Physics, 2005.

[50] R. Nalim, K. Pekkan, H. B. Sun, and H. Yokota, "Oscillating Couette flow for in vitro cell loading," *Journal of Biomechanics,* vol. 37, no. 6, pp. 939-942, 2004.

[51] K. Middleton, A. Kondiboyina, M. Borrett, Y. Cui, X. Mei, and L. You, "Microfluidics approach to investigate the role of dynamic similitude in osteocyte mechanobiology," *Journal of Orthopaedic Research,* vol. 36, no. 2, pp. 663-671, 2018.

[52] O. Onaizah and E. Diller, "Tetherless Mobile Micro-Surgical Scissors Using Magnetic Actuation," in *2019 International Conference on Robotics and Automation (ICRA)*, 2019, pp. 894-899.

[53] M. Al-Hussaini, I. Sultan, N. Abuirmileh, I. Jaradat, and I. Qaddoumi, "Pineal gland tumors: experience from the SEER database," *J Neurooncol*, vol. 94, no. 3, pp. 351-8, 2009.

[54] N. Simaan, R. M. Yasin, and L. Wang, "Medical Technologies and Challenges of Robot-Assisted Minimally Invasive Intervention and Diagnostics," *Annual Review of Control, Robotics, and Autonomous Systems*, vol. 1, no. 1, pp. 465-490, 2018.

[55] I. A. M. J. Broeders and J. Ruurda, "Robotics revolutionizing surgery: the Intuitive Surgical “Da Vinci” system," *Industrial Robot: An International Journal*, vol. 28, no. 5, pp. 387-392, 2001.

[56] J. J. Doulgeris, S. A. Gonzalez-Blohm, A. K. Filis, T. M. Shea, K. Aghayev, and F. D. Vrionis, "Robotics in Neurosurgery: Evolution, Current Challenges, and Compromises," *Cancer Control*, vol. 22, no. 3, pp. 352-359, 2015.

[57] T. Ota, A. Degani, D. Schwartzman, B. Zubiate, J. McGarvey, H. Choset, *et al.*, "A Highly Articulated Robotic Surgical System for Minimally Invasive Surgery," *The Annals of thoracic surgery*, vol. 87, no. 4, pp. 1253-1256, 2009.

[58] J. Burgner-Kahrs, D. C. Rucker, and H. Choset, "Continuum Robots for Medical Applications: A Survey," *IEEE Transactions on Robotics*, vol. 31, no. 6, pp. 1261-1280, 2015.

[59] C. Bergeles, A. H. Gosline, N. V. Vasilyev, P. J. Codd, P. J. d. Nido, and P. E. Dupont, "Concentric Tube Robot Design and Optimization Based on Task and Anatomical Constraints," *IEEE Transactions on Robotics*, vol. 31, no. 1, pp. 67-84, 2015.

[60] V. Agrawal, W. J. Peine, B. Yao, and S. Choi, "Control of cable actuated devices using smooth backlash inverse," in *IEEE International Conference on Robotics and Automation*, 2010, pp. 1074-1079.

[61] N. Simaan, X. Kai, W. Wei, A. Kapoor, P. Kazanzides, R. Taylor, *et al.*, "Design and Integration of a Telerobotic System for Minimally Invasive Surgery of the Throat," *The International Journal of Robotics Research*, vol. 28, no. 9, pp. 1134-1153, 2009.

[62] L. G. Torres, C. Baykal, and R. Alterovitz, "Interactive-rate motion planning for concentric tube robots," in *2014 IEEE International Conference on Robotics and Automation (ICRA)*, 2014, pp. 1915-1921.

[63] M. Sitti, H. Ceylan, W. Hu, J. Giltinan, M. Turan, S. Yim, *et al.*, "Biomedical Applications of Untethered Mobile Milli/Microrobots," *Proceedings of the IEEE*, vol. 103, no. 2, pp. 205-224, 2015.

[64] E. Gultepe, J. S. Randhawa, S. Kadam, S. Yamanaka, F. M. Selaru, E. J. Shin, *et al.*, "Biopsy with Thermally-Responsive Untethered Microtools," *Advanced Materials,* vol. 25, no. 4, pp. 514-519, 2012.

[65] E. Diller and M. Sitti, "Three-Dimensional Programmable Assembly by Untethered Magnetic Robotic Micro-Grippers," *Advanced Functional Materials,* vol. 24, no. 28, pp. 4397-4404, 2014.

[66] J. Zhang, O. Onaizah, K. Middleton, L. You, and E. Diller, "Reliable Grasping of Three-Dimensional Untethered Mobile Magnetic Microgripper for Autonomous Pick-and-Place," *IEEE Robotics and Automation Letters,* vol. 2, no. 2, pp. 835-840, 2017.

[67] I. S. M. Khalil, D. Mahdy, A. E. Sharkawy, R. R. Moustafa, A. F. Tabak, M. E. Mitwally, *et al.*, "Mechanical Rubbing of Blood Clots Using Helical Robots Under Ultrasound Guidance," *IEEE Robotics and Automation Letters,* vol. 3, no. 2, pp. 1112-1119, 2018.

[68] A. C. Barnett, J. A. Jones, Y.-S. Lee, and J. Z. Moore, "Compliant Needle Vibration Cutting of Soft Tissue," *Journal of Manufacturing Science and Engineering,* vol. 138, no. 11, pp. 111011-111011-9, 2016.

[69] J. Leclerc, A. Ramakrishnan, N. V. Tsekos, and A. T. Becker, "Magnetic Hammer Actuation for Tissue Penetration Using a Millirobot," *IEEE Robotics and Automation Letters,* vol. 3, no. 1, pp. 403-410, 2018.

[70] B. J. Nelson, I. K. Kaliakatsos, and J. J. Abbott, "Microrobots for Minimally Invasive Medicine," *Annual Review of Biomedical Engineering,* vol. 12, no. 1, pp. 55-85, 2010.

[71] M. Simi, G. Gerboni, A. Menciassi, and P. Valdastri, "Magnetic Torsion Spring Mechanism for a Wireless Biopsy Capsule," *Journal of Medical Devices,* vol. 7, no. 4, p. 041009, 2013.

[72] M. Hagiwara, T. Kawahara, Y. Yamanishi, and F. Arai, "Precise Control of Magnetically Driven Microtools for Enucleation of Oocytes in a Microfluidic Chip," *Advanced Robotics,* vol. 25, no. 8, pp. 991-1005, 2011.

[73] A. A. Sharp, A. M. Ortega, D. Restrepo, D. Curran-Everett, and K. Gall, "In Vivo Penetration Mechanics and Mechanical Properties of Mouse Brain Tissue at Micrometer Scales," *IEEE transactions on bio-medical engineering,* vol. 56, no. 1, pp. 45-53, 2009.

[74] M. Khadem, C. Rossa, R. S. Sloboda, N. Usmani, and M. Tavakoli, "Mechanics of Tissue Cutting During Needle Insertion in Biological Tissue," *IEEE Robotics and Automation Letters,* vol. 1, no. 2, pp. 800-807, 2016.

[75] S. Greenish, V. Hayward, V. Chial, A. Okamura, and T. Steffen, "Measurement, Analysis, and Display of Haptic Signals During Surgical Cutting," *Presence: Teleoperators and Virtual Environments,* vol. 11, no. 6, pp. 626-651, 2002.

[76] B. Takabi and B. L. Tai, "A review of cutting mechanics and modeling techniques for biological materials," *Medical Engineering and Physics,* vol. 45, pp. 1-14, 2017.

[77] B. Takabi and B. L. Tai, "A review of cutting mechanics and modeling techniques for biological materials," *Medical Engineering and Physics,* vol. 45, pp. 1-14.

[78] E. Reyssat, T. Tallinen, M. Le Merrer, and L. Mahadevan, "Slicing Softly with Shear," *Physical Review Letters,* vol. 109, no. 24, p. 244301, 2012.

[79] T. Chanthasopeephan, J. P. Desai, and A. C. Lau, "Measuring forces in liver cutting: new equipment and experimental results," *Ann Biomed Eng,* vol. 31, no. 11, pp. 1372-82, 2003.

[80] T. Chanthasopeephan, J. P. Desai, and A. C. Lau, "Study of soft tissue cutting forces and cutting speeds," *Stud Health Technol Inform,* vol. 98, pp. 56-62, 2004.

[81] T. Chanthasopeephan, J. P. Desai, and A. C. Lau, "Determining deformation resistance in cutting soft tissue with nonuniform thickness," *Conf Proc IEEE Eng Med Biol Soc,* vol. 4, pp. 2754-7, 2004.

[82] T. Chanthasopeephan, J. P. Desai, and A. C. Lau, "Modeling soft-tissue deformation prior to cutting for surgical simulation: finite element analysis and study of cutting parameters," *IEEE Trans Biomed Eng,* vol. 54, no. 3, pp. 349-59, 2007.

[83] M. Giovannini and K. Ehmann, "Vibrational Cutting of Soft Tissue with Micro-serrated Surgical Scalpels," *Procedia CIRP,* vol. 45, no. Complete, pp. 199-202, 2016.

[84] T. Azar and V. Hayward, "Estimation of the Fracture Toughness of Soft Tissue from Needle Insertion," in *Biomedical Simulation*, 2008, pp. 166-175.

[85] S. Misra, K. B. Reed, B. W. Schafer, K. T. Ramesh, and A. M. Okamura, "Mechanics of Flexible Needles Robotically Steered through Soft Tissue," *Int J Rob Res,* vol. 29, no. 13, pp. 1640-1660, 2010.

[86] T. Yang, L. Xiong, J. Zhang, L. Yang, W. Huang, J. Zhou, *et al.*, "Modeling cutting force of laparoscopic scissors," in *2010 3rd International Conference on Biomedical Engineering and Informatics*, 2010, pp. 1764-1768.

[87] C. T. McCarthy, M. Hussey, and M. D. Gilchrist, "On the sharpness of straight edge blades in cutting soft solids: Part I – indentation experiments," *Engineering Fracture Mechanics,* vol. 74, no. 14, pp. 2205-2224, 2007.

[88] C. T. McCarthy, A. N. Annaidh, and M. D. Gilchrist, "On the sharpness of straight edge blades in cutting soft solids: Part II – Analysis of blade geometry," *Engineering Fracture Mechanics,* vol. 77, no. 3, pp. 437-451, 2010.

[89] D. Taylor, N. O'Mara, E. Ryan, M. Takaza, and C. Simms, "The fracture toughness of soft tissues," *Journal of the Mechanical Behavior of Biomedical Materials,* vol. 6, pp. 139-147, 2012.

[90] M. Mahvash, L. M. Voo, D. Kim, K. Jeung, J. Wainer, and A. M. Okamura, "Modeling the forces of cutting with scissors," *IEEE Trans Biomed Eng*, vol. 55, no. 3, pp. 848-56, 2008.

[91] B. P. Pereira, P. W. Lucas, and T. Swee-Hin, "Ranking the fracture toughness of thin mammalian soft tissues using the scissors cutting test," *J Biomech*, vol. 30, no. 1, pp. 91-4, 1997.

[92] W.-C. Yeh, P.-C. Li, Y.-M. Jeng, H.-C. Hsu, P.-L. Kuo, M.-L. Li, *et al.*, "Elastic modulus measurements of human liver and correlation with pathology," *Ultrasound in Medicine and Biology*, vol. 28, no. 4, pp. 467-474, 2002.

[93] H. J. Kwon, A. D. Rogalsky, and D.-W. Kim, "On the measurement of fracture toughness of soft biogel," *Polymer Engineering & Science*, vol. 51, no. 6, pp. 1078-1086, 2011.

[94] C. Gokgol, C. Basdogan, and D. Canadinc, "Estimation of fracture toughness of liver tissue: Experiments and validation," *Medical Engineering & Physics*, vol. 34, no. 7, pp. 882-891, 2012.

[95] Z. Hu, B. Zhang, and W. Sun, "Cutting characteristics of biological soft tissues," *CIRP Annals*, vol. 61, no. 1, pp. 135-138, 2012.

[96] B. Chu, E. Gaillard, R. Mongrain, S. Reiter, and J.-C. Tardif, "Characterization of fracture toughness exhaustion in pig aorta," *Journal of the Mechanical Behavior of Biomedical Materials*, vol. 17, pp. 126-136, 2013.

[97] K. Manickam, R. R. Machireddy, and S. Seshadri, "Characterization of biomechanical properties of agar based tissue mimicking phantoms for ultrasound stiffness imaging techniques," *Journal of the Mechanical Behavior of Biomedical Materials*, vol. 35, pp. 132-143, 2014.

[98] C. Pawashe, S. Floyd, and M. Sitti, "Dynamic Modeling of Stick Slip Motion in an Untethered Magnetic Micro-Robot," in *Robotics: Science and Systems*, 2008.

[99] F. Pervin and W. W. Chen, "Mechanically Similar Gel Simulants for Brain Tissues," in *Dynamic Behavior of Materials, Volume 1*, 2011, pp. 9-13.

Copyright Acknowledgement

SPRINGER NATURE

A generic label-free microfluidic microobject sorter using a magnetic elastic diverter

Author: Jiachen Zhang, Onaizah Onaizah, Amir Sadri et al
Publication: Biomedical Microdevices
Publisher: Springer Nature
Date: Jan 1, 2017

Order Completed

Thank you for your order.

This Agreement between Onaizah Onaizah ("You") and Springer Nature ("Springer Nature") consists of your order details and the terms and conditions provided by Springer Nature and Copyright Clearance Center.

License number	Reference confirmation email for license number
License date	Jan, 14 2020

Licensed Content

Licensed Content Publisher	Springer Nature
Licensed Content Publication	Biomedical Microdevices
Licensed Content Title	A generic label-free microfluidic microobject sorter using a magnetic elastic diverter
Licensed Content Author	Jiachen Zhang, Onaizah Onaizah, Amir Sadri et al
Licensed Content Date	Jan 1, 2017
Licensed Content Volume	19
Licensed Content Issue	2

Order Details

Type of Use	Thesis/Dissertation
Requestor type	academic/university or research institute
Format	electronic
Portion	full article/chapter
Will you be translating?	no
Circulation/distribution	2000 - 4999
Author of this Springer Nature content	yes

About Your Work

Title	Millimeter-Scale Magnetically Actuated Robotic Tools for Surgery and Cell Manipulation
Institution name	University of Toronto
Expected presentation date	Jan 2020

Additional Data

Requestor Location

Onaizah Onaizah
2422 Colonel William Pkwy

Requestor Location

Oakville, ON L6M0K1
Canada
Attn: English

Tax Details

Billing Information

Billing Type: Invoice
English
2422 Colonel William Pkwy

Billing address

Oakville, ON L6M0K1
Canada
Attn: English

Price

Total: 0.00 USD

Total: 0.00 USD

CLOSE WINDOW